UNIVERSIDADE FEDERAL DO RIO GRANDE DO SUL

CENTRO ESTADUAL DE PESQUISAS EM SENSORIAMENTO REMOTO E METEOROLOGIA

PROGRAMA DE PÓS-GRADUAÇÃO EM SENSORIAMENTO REMOTO

LUCAS RIBEIRO DIAZ

CORREÇÃO ATMOSFÉRICA DE IMAGENS TERMAIS UTILIZANDO PERFIS VERTICAIS DE ALTA RESOLUÇÃO SIMULADOS POR UM MODELO DE MESOESCALA

PORTO ALEGRE

2021

LUCAS RIBEIRO DIAZ

CORREÇÃO ATMOSFÉRICA DE IMAGENS TERMAIS UTILIZANDO PERFIS VERTICAIS DE ALTA RESOLUÇÃO SIMULADOS POR UM MODELO DE MESOESCALA

Dissertação de mestrado apresentada ao Programa de Pós-Graduação em Sensoriamento Remoto como requisito parcial para a obtenção do título de mestre em Sensoriamento Remoto e Geoprocessamento.

Orientadora: Profa. Dra. Silvia Beatriz Alves Rolim

PORTO ALEGRE

2021

CIP - Catalogação na Publicação

Diaz, Lucas Ribeiro
Correção atmosférica de imagens termais utilizando perfis verticais de alta resolução simulados por um modelo de mesoescala / Lucas Ribeiro Diaz. -- 2021.
115 f.
Orientadora: Silvia Beatriz Alves Rolim.

Dissertação (Mestrado) -- Universidade Federal do Rio Grande do Sul, Centro Estadual de Pesquisas em Sensoriamento Remoto e Meteorologia, Programa de Pós-Graduação em Sensoriamento Remoto, Porto Alegre, BR-RS, 2021.

1. Sensoriamento remoto. 2. Temperatura de superfície. 3. WRF. 4. Reanálise. 5. Infravermelho termal. I. Rolim, Silvia Beatriz Alves, orient. II. Título.

Elaborada pelo Sistema de Geração Automática de Ficha Catalográfica da UFRGS com os dados fornecidos pelo(a) autor(a).

CEPSRM
CENTRO ESTADUAL DE PESQUISAS EM SENSORIAMENTO REMOTO E METEOROLOGIA
UNIVERSIDADE FEDERAL DO RIO GRANDE DO SUL

UFRGS 8 vezes a melhor Federal do Brasil

PROGRAMA DE PÓS-GRADUAÇÃO EM SENSORIAMENTO REMOTO

DISSERTAÇÃO

Submetida como parte dos requisitos
para obtenção do Grau de

MESTRE EM SENSORIMENTO REMOTO E GEOPROCESSAMENTO

Programa de Pós-Graduação em Sensoriamento Remoto (PPGSR)
Centro Estadual de Pesquisas em Sensoriamento Remoto e Meteorologia (CEPRSM)
Universidade Federal do Rio Grande do Sul (UFRGS)
Porto Alegre, RS, Brasil.

Aprovada em: 09/09/2021.

Pela Banca Examinadora:

SRolim
Digitally signed by SRolim
DN: cn=SRolim, o=UFRGS, ou, email=silvia.rolim@ufrgs.br, c=BR
Date: 2021.09.12 17:58:06 -03'00'

Profa. Dra. Silvia Beatriz Alves Rolim
Orientadora

Homologada em: 09/09/2021.

Por:

Prof. Dr. Guilherme Garcia de Oliveira
Coordenador do Programa de Pós-Graduação em Sensoriamento Remoto

Prof. Dr. Anderson Luis Ruhoff
(IPH/UFRGS)

Dr. Dražen Skoković
(Universitat de València)

Profa. Drª. Rita de Cássia Marques Alves
(PPGSR/UFRGS)

Av. Bento Gonçalves, 9.500 - Campus do Vale
Bairro Agronomia - CEP 91501-970 - Porto Alegre -RS
Telefones: (51) 3308-6221 e (51) 3308-7479
http: //www.ppgsr.ufrgs.br
Endereço eletrônico: ppgsr@ufrgs.br

Dedico este trabalho aos meus pais Maria Clara e Eviltom.

AGRADECIMENTOS

À minha orientadora professora Silvia Rolim pelos ensinamentos recebidos e pelas contribuições na construção deste trabalho. Agradeço por ter concedido minha primeira oportunidade cientifica ainda na graduação. Lá se vão mais de 6 anos trabalhando juntos, obrigado por sempre acreditar em mim.

Aos meus pais, Maria Clara e Eviltom, por serem sempre os meus exemplos e meus maiores incentivadores.

À minha irmã Liz, por todo apoio e parceria.

À minha namorada Luiza, pelo carinho e companheirismo. Mesmo que muitas vezes distantes fisicamente, estivemos sempre juntos em busca dos nossos sonhos.

Ao Daniel Caetano, por me auxiliar no desenvolvimento da pesquisa e estar sempre disposto a responder as minhas questões.

Aos colegas e amigos do Laboratório de Sensoriamento Remoto Geológico (LabSRGeo), Eduardo, Luján, Nájila, Pâmela e Savannah pela excelente convivência e pelas inúmeras vezes que colaboraram no desenvolvimento deste trabalho.

À banca examinadora, pela disponibilidade e interesse em compartilhar seus conhecimentos e valiosas sugestões.

À Coordenação de Aperfeiçoamento de Pessoal de Nível Superior (CAPES) pela concessão da bolsa de pesquisa.

À Universidade Federal do Rio Grande do Sul (UFRGS) e ao Centro Estadual de Pesquisas em Sensoriamento Remoto e Meteorologia (CEPSRM), com seus professores e funcionários, que proporcionaram as condições para a realização do meu mestrado.

E a todos amigos, familiares e profissionais que não foram aqui citados, mas que, de alguma forma, contribuíram nessa jornada.

RESUMO

A estimativa da temperatura da superfície terrestre (LST) por sensoriamento remoto no infravermelho termal (TIR) é dependente da realização de uma correção atmosférica apropriada que, em geral, necessita de perfis atmosféricos como dados de entrada. Dados globais de reanálise são uma alternativa prática para a obtenção desses perfis, mas podem apresentar limitações. Nesse contexto, o presente estudo teve como objetivo analisar a utilização do modelo numérico *Weather Research and Forecasting* (WRF) para gerar perfis verticais de alta resolução, refinando dados de reanálise, visando a correção atmosférica no TIR para o cálculo de valores de LST. Para tal, foram realizadas simulações com o modelo WRF com dados de reanálise do NCEP *Climate Forecast System Version* 2 (CFSv2) como condições iniciais e utilizando duas grades aninhadas com resoluções horizontais de 12 km (G12) e 3 km (G03). Para estimar a LST, foram empregados: o método da inversão direta da Equação de Transferência Radiativa (RTE), o modelo MODTRAN e valores de radiância da banda 10 do Landsat 8 TIRS. A pesquisa avaliou o desempenho do modelo através dos perfis verticais, dos parâmetros atmosféricos de correção (transmitância atmosférica e radiâncias *upwelling* e *downwelling*) e dos valores de LST, utilizando como referência dados de radiossondagens *in situ*, no sul do Brasil. Adicionalmente, foi executada uma análise de sensibilidade a dois esquemas de parametrização de camada limite planetária. Os resultados indicam que o modelo WRF simula de maneira satisfatória os perfis atmosféricos que, por consequência, geram parâmetros de correção e LST com baixos erros. Contudo, não existe melhora significativa nas métricas estatísticas entre os perfis extraídos diretamente da reanálise CFSv2 e os simulados pelo WRF. Em alguns casos, a utilização de um perfil de grade mais refinada resultou, até mesmo, em maiores erros. Os valores gerais de RMSE para a LST foram: 0,55 K (CFSv2), 0,79 K (WRF G12) e 0,82 K (WRF G03). A escolha do esquema de camada limite mostrou-se caso-dependente. Conclui-se que não há necessidade especial de refinar a resolução dos perfis de reanálise visando estimativa de LST, por meio do método da RTE.

Palavras-chave: Sensoriamento remoto. Temperatura de superfície. WRF. Reanálise. Infravermelho termal.

ABSTRACT

The Land Surface Temperature (LST) retrieval from thermal infrared (TIR) remote sensing depends on performing an appropriate atmospheric correction. In general, this approach requires atmospheric profiles as input data. Global reanalysis data are a practical alternative to obtain these profiles, but they may have limitations. In this context, this study aimed to assess the use of the Weather Research and Forecasting (WRF) numerical model to generate high-resolution vertical profiles, downscaling reanalysis data, to be applied in TIR atmospheric correction for LST retrieval. WRF simulations were carried out using NCEP Climate Forecast System Version 2 (CFSv2) reanalysis as initial conditions and two nested grids with horizontal resolutions of 12 km (G12) and 3 km (G03). To retrieve the LST, we used: the Radiative Transfer Equation (RTE) based method, the MODTRAN model, and radiance values from Landsat 8 TIRS10 band. This research evaluated the model performance through vertical profiles, atmospheric correction parameters (atmospheric transmittance and upwelling and downwelling radiances), and LST values, using in situ radiosonde data (in Southern Brazil) as reference. Moreover, a sensitivity analysis to two planetary boundary layer parameterization schemes was performed. The results indicate that the WRF model satisfactorily simulates the atmospheric profiles that, consequently, generate correction parameters and LST with low errors. However, there is no significant improvement in statistical metrics between profiles extracted directly from the CFSv2 reanalysis and those simulated by WRF. In some cases, the use of a finer grid profile resulted even in larger errors. The LST overall RMSE values were: 0.55 K (CFSv2), 0.79 K (WRF G12), and 0.82 K (WRF G03). The boundary layer scheme choice proved to be case-dependent. We concluded that there is no special need to increase the resolution of reanalysis profiles in order to retrieve LST using the RTE-based method.

Keywords: Remote sensing. Surface temperature. WRF. Reanalysis. Thermal infrared

LISTA DE ABREVIATURAS E SIGLAS

ACPC	Calculadora de Parâmetros de Correção Atmosférica, do inglês *Atmospheric Correction Parameter Calculation*
AIRS	*Atmospheric Infrared Sounder*
ARW	*Advanced Research* WRF
BOA	Base da atmosfera, equivalente ao nível do solo, do inglês *Bottom Of the Atmosphere*
CFSR	*Climate Forecast System Reanalysis*
CFSv2	*Climate Forecast System Version* 2
DOE	*United States Department of Energy*
ECMWF	*European Centre for Medium-Range Weather Forecasts*
ERA5	Sistema de dados de reanálise do ECMWF
ERA-Interim	Sistema de dados de reanálise do ECMWF
GAPRI	*Global Atmospheric Profiles derived from Reanalysis Information*
GFS	*Global Forecast System*
IRS	*Infrared Scanner,* sensor a bordo do satélite HJ-1B
JRA	*Japanese Reanalysis*
KMA	*Korea Meteorological Administration*
LSE	Emissividade da superfície terrestre, do inglês *Land Surface Emissivity*
LST	Temperatura da superfície terrestre, do inglês *Land Surface Temperature*
MAE	Erro médio absoluto, do inglês *Mean Absolute Error*
MERRA	*Modern Era Retrospective-Analysis for Research and Applications*
MOD07	Produto de perfis atmosféricos do sensor MODIS
MODIS	*Moderate Resolution Radiometer*
MODTRAN	*MODerate resolution atmospheric TRANsmission*
MRF	*Medium-Range Forecast Model*, esquema de parametrização de camada limite
MYJ	*Mellor–Yamada–Janjic*, esquema de parametrização de camada limite
NCAR	*National Center for Atmospheric Research*
NCEP FNL	Sistema de dados de (re)análise do NCEP, FNL – *Final*
NCEP	*National Center for Environmental Prediction*

NDVI	Índice de Vegetação por Diferença Normalizada, do inglês *Normalized Difference Vegetation Index*
$NDVI^{THM}$	NDVI *THresholds Method*
NIR	Infravermelho próximo, do inglês *Near-InfraRed*
NMM	*Nonhydrostatic Mesoscale Model*
NWP	Previsão numérica do tempo, do inglês *Numerical Weather Prediction*
OLI	*Operational Land Imager*, sensor a bordo do satélite Landsat 8
PBL	Camada limite planetária, do inglês *Planetary Boundary Layer*
R1	*Reanalysis* 1, NCEP/NCAR
R2	*Reanalysis* 2, NCEP/DOE
REM	Radiação eletromagnética
RMSE	Raiz do erro quadrático médio, do inglês *Root Mean Square Error*
RTE	Equação de Transferência Radiativa, do inglês *Radiative Transfer Equation*
RTM	Modelo de transferência radiativa, do inglês *Radiative Transfer Model*
SBPA	Código referente ao Aeroporto Internacional de Porto Alegre, Brasil
SWIR	Infravermelho de ondas curtas, do inglês Short *Wavelength InfraRed*
TIR	Infravermelho Termal, do inglês *Thermal InfraRed*
TIRS	*Thermal InfraRed Sensor*, sensor a bordo do satélite Landsat 8
TOA	Topo da atmosfera, do inglês *Top Of the Atmosphere*
USGS	*United States Geological Survey*
VIIRS	*Visible Infrared Imaging Radiometer Suite*
VNIR	Regiões espectrais do visível + infravermelho próximo
WPS	*WRF Preprocessing System*
WRF	*Weather Research and Forecasting*
WRFDA	*WRF Data Assimilation System*
YSU	*Yonsei University*, esquema de parametrização de camada limite

LISTA DE SÍMBOLOS

B_λ	Radiância espectral de um corpo negro
T	Temperatura
λ	Comprimento de onda
$C_{1,2}$	Constantes físicas da radiação (Lei de Planck)
ε	Emissividade
λ_{max}	Comprimento de onda de máxima emissão
L_λ^{sen}	Radiância espectral para medida por um sensor no TOA
T_s	Temperatura da superfície (LST)
$L_\lambda^{\downarrow}$	Radiância atmosférica de trajetória descendente (*downwelling*)
$L_\lambda^{\uparrow}$	Radiância atmosférica de trajetória ascendente (*upwelling*)
τ	Transmitância atmosférica
R_s	Resposta espectral de um determinado sensor
var	Variável genérica utilizada para denotar um dos parâmetros atmosféricos (transmitância, *upwelling* ou *downwelling*)
ρ	Reflectância
P_V	Proporção de vegetação
$d\varepsilon_\lambda$	Termo que leva em consideração o “efeito de cavidade” da superfície, na estimativa da emissividade
F'	Fator geométrico na estimativa da emissividade

SUMÁRIO

1 INTRODUÇÃO

A temperatura da superfície terrestre (*Land Surface Temperature* – LST) é um parâmetro-chave utilizado em variados estudos biogeofísicos (CAO *et al.*, 2019; LI *et al.*, 2013c; SKOKOVIC; SOBRINO; JIMENEZ-MUNOZ, 2017; SOBRINO *et al.*, 2016; WENG, 2009) uma vez que está intimamente conectada com o balanço de energia na superfície da Terra (ANDERSON *et al.*, 2008; TARDY *et al.*, 2016; WU *et al.*, 2021).

O sensoriamento remoto nos comprimentos de onda do Infravermelho Termal (*Thermal InfraRed* – TIR) é um meio valioso de se obter informações de temperatura da superfície em escala regional e global de maneira operacional e economicamente viável (COLL *et al.*, 2012; LI *et al.*, 2013c; MENG; CHENG, 2018; ROSAS; HOUBORG; MCCABE, 2017). Contudo, os sensores TIR a bordo de satélites registram a radiância espectral no topo da atmosfera (*Top Of the Atmosphere* – TOA), que é influenciada, não somente pelos parâmetros da superfície (emissividade e temperatura), como também pela composição e pela estrutura da atmosfera (vapor de água, principalmente) ao longo do caminho entre a superfície e o sensor (JIMÉNEZ-MUÑOZ *et al.*, 2010; LI *et al.*, 2013c). Portanto, os efeitos atmosféricos devem ser removidos para a correta utilização dos dados termais de sensoriamento remoto nas mais variadas aplicações (GALVE *et al.*, 2018; TANG; LI, 2014). Em termos gerais, realiza-se uma conversão de dados do TOA para o nível do solo (*ground-level*; *Bottom Of the Atmosphere* – BOA). Esse processo é conhecido como correção atmosférica e, se negligenciado, pode resultar em erros sistemáticos na estimativa de valores de LST (BARSI *et al.*, 2005; JIMÉNEZ-MUÑOZ *et al.*, 2010; TARDY *et al.*, 2016).

Uma das maneiras mais consolidadas de se realizar a correção atmosférica é por meio da Equação de Transferência Radiativa (*Radiative Transfer Equation* – RTE) (PRICE, 1983). Essa abordagem envolve uma inversão direta da RTE para obtenção da LST em uma banda (comprimento de onda) específica, sendo, teoricamente, o método mais apropriado para recuperação da LST a partir da radiância de uma única banda TIR (JIMÉNEZ-MUÑOZ *et al.*, 2010; LI *et al.*, 2013c). O método da inversão da RTE necessita de perfis atmosféricos verticais (temperatura, umidade, pressão) como dados de entrada, os quais são inseridos em modelos de transferência radiativa (*Radiative Transfer Model* – RTM) para calcular

três parâmetros atmosféricos necessários para resolver a RTE: transmitância atmosférica e radiâncias atmosféricas de trajetória ascendente (*upwelling*) e descendente (*downwelling*) (BARSI; BARKER; SCHOTT, 2003; COLL *et al.*, 2012; JIMÉNEZ-MUÑOZ *et al.*, 2010; MENG; CHENG, 2018).

Radiossondagens locais sincronizadas com a passagem do satélite são consideradas como a situação ideal e a fonte mais fidedigna de perfis atmosféricos (MENG; CHENG, 2018; SEKERTEKIN, 2019; SOBRINO; JIMÉNEZ-MUÑOZ; PAOLINI, 2004). Entretanto, na grande maioria dos estudos reais, radiossondagens *in situ* não estão disponíveis (COLL *et al.*, 2012; LI *et al.*, 2013a; MENG; CHENG, 2018; PÉREZ-PLANELLS; GARCÍA-SANTOS; CASELLES, 2015), devido ao alto custo financeiro envolvido (JIMÉNEZ-MUÑOZ *et al.*, 2010; LI *et al.*, 2013c). Existem estações, com lançamentos diários de radiossondas, espalhadas ao redor do globo terrestre (em aeroportos, por exemplo). Todavia, o registro desses dados pode não ser sincronizado com o horário de passagem do satélite ou a estação pode estar demasiada distante da cena da área de estudo (MIRA *et al.*, 2014; TARDY *et al.*, 2016). Dessa forma, estudos com radiossondagens ficam restritos a trabalhos de validação realizados em locais específicos (COLL *et al.*, 2005; ROSAS; HOUBORG; MCCABE, 2017).

Portanto, produtos de perfis atmosféricos provindos de diferentes fontes vêm sendo utilizados como alternativa às radiossondagens na correção atmosférica de dados TIR, resultando em valores de LST com acurácias aceitáveis (BARSI *et al.*, 2005; DUAN *et al.*, 2018; GALVE *et al.*, 2018; MALAKAR *et al.*, 2018; MATTAR *et al.*, 2015; MENG; CHENG, 2018; SKOKOVIC; SOBRINO; JIMENEZ-MUNOZ, 2017; TARDY *et al.*, 2016; VANHELLEMONT, 2020a). Perfis derivados de dados de satélite (AUMANN *et al.*, 2003; BORBAS; MENZEL, 2017; DIAO *et al.*, 2013) superam as limitações espaciais das radiossondas locais, uma vez que estão disponíveis na escala do pixel do satélite em questão. Apesar de apresentarem uma alta resolução espacial, esses perfis podem ter seu uso comprometido pela baixa resolução temporal (apenas no horário de passagem do satélite) (ROSAS; HOUBORG; MCCABE, 2017; YANG *et al.*, 2020). Os resultados podem, por consequência, não ser satisfatórios quando o satélite do sensor TIR de interesse não é o mesmo, ou não é sincronizado com a passagem, daquele que os perfis são derivados (COLL *et al.*, 2012; GALVE *et al.*, 2018). Para sobrepujar essa limitação

temporal, perfis provindos de dados globais de reanálise (DEE *et al.*, 2011; HERSBACH *et al.*, 2020; KALNAY *et al.*, 1996; KANAMITSU *et al.*, 2002; KOBAYASHI *et al.*, 2015; NCEP *et al.*, 2000; RIENECKER *et al.*, 2011; SAHA *et al.*, 2010, 2014) proporcionam uma resolução temporal flexível (de 3 ou 6 horas, tipicamente) e consistem em uma alternativa pratica às restrições espaciais dos dados de radiossondas (ROSAS; HOUBORG; MCCABE, 2017). Dados de reanálise correspondem a séries temporais homogêneas distribuídas globalmente em pontos de grade, isto é, sem lacunas temporais ou espaciais (ALGHAMDI, 2020).

Barsi *et al.* (2005) e Barsi, Barker e Schott (2003) propuseram uma Calculadora de Parâmetros de Correção Atmosférica (*Atmospheric Correction Parameter Calculation* – ACPC), uma ferramenta online para as bandas termais dos Landsat 5, 7 e 8. A ACPC utiliza perfis de reanálise do *National Center for Environmental Prediction* (NCEP) e o código do modelo de transferência radiativa *MODerate resolution atmospheric TRANsmission* (MODTRAN) (BERK *et al.*, 2014) para fornecer aos usuários os três parâmetros atmosféricos necessários à correção. Outros autores avaliaram e compararam a eficiência de diferentes fontes de perfis atmosféricos (tanto de reanálise como derivados de satélite) para a correção atmosférica/recuperação de LST. Perfis provindos do NCEP (*Reanalysis* 1 (KALNAY *et al.*, 1996) e FNL (NCEP *et al.*, 2000)) e do produto MOD07 do sensor *Moderate Resolution Radiometer* (MODIS) (BORBAS; MENZEL, 2017) foram analisados em diferentes áreas na Espanha (JIMÉNEZ-MUÑOZ *et al.*, 2010; PÉREZ-PLANELLS; GARCÍA-SANTOS; CASELLES, 2015; SKOKOVIC; SOBRINO; JIMENEZ-MUNOZ, 2017) e na China (LI *et al.*, 2013a) para os sensores TIR Landsat, ASTER e HJ-1B IRS. Coll *et al.* (2012), também na Espanha, adicionaram na análise comparativa os perfis de sondagens por satélite do *Atmospheric Infrared Sounder* (AIRS) (AUMANN *et al.*, 2003). Rosas, Houborg e McCabe (2017), por sua vez, incluíram o produto de reanálise *European Centre for Medium-Range Weather Forecasts* (ECMWF) ERA-Interim (DEE *et al.*, 2011), juntamente com os perfis acima mencionados, para estimar a LST na Arábia Saudita.

Recentemente, estudos incluindo um maior número de fontes de perfis atmosféricos foram realizados. Meng e Cheng (2018) consideraram os perfis de reanálise: *Modern Era Retrospective-Analysis for Research and Applications* (MERRA) (RIENECKER *et al.*, 2011) 1 e 2, ERA-Interim, NCEP FNL e NCEP

Reanalysis 2 (R2) (KANAMITSU *et al.*, 2002) e *Japanese Reanalysis* (JRA)-55 (KOBAYASHI *et al.*, 2015). A validação incluiu perfis distribuídos ao redor do globo e 32 imagens Landsat 8 banda 10 sobre a China. Yang *et al.* (2020) avaliaram sete fontes de perfis atmosféricos (AIRS, MOD07, ERA-Interim, MERRA2 e NCEP FNL, R2, GFS) utilizando 17 estações de radiossondas na Europa e medidas *in situ* de LST na China. Em geral, as acurácias na estimativa dos parâmetros atmosféricos e da LST são menores quando são utilizados perfis derivados de dados de satélite do que quando são aplicados aqueles provindos de reanálises (COLL *et al.*, 2012; LI *et al.*, 2013a; PÉREZ-PLANELLS; GARCÍA-SANTOS; CASELLES, 2015; SKOKOVIC; SOBRINO; JIMENEZ-MUNOZ, 2017; YANG *et al.*, 2020).

Entretanto, perfis de reanálise também possuem limitações. Sua resolução espacial de alguns graus (variando de acordo com o produto) pode ser considerada baixa. A acurácia é, via de regra, inferior para regiões com menor cobertura de observatórios permanentes, como é o caso dos oceanos e de muitas zonas no Hemisfério Sul (ALGHAMDI, 2020; CHEN; LIU, 2016; CHEN *et al.*, 2014). A descrição de fenômenos meteorológicos em escalas de tempo variável e subgrade pode ser afetada, devido aos dados serem espaçados em pontos de grade com intervalos de tempo de comumente 6 horas (TONOOKA, 2001). Por outro lado, modernos modelos numéricos de previsão do tempo e pesquisa atmosférica proporcionam desempenho computacional e parametrizações de processos físicos para refinar dados de reanálise (EVANS; EKSTRÖM; JI, 2012; ONWUKWE; JACKSON, 2020; PRASAD; SHERWOOD; BROGNIEZ, 2020). Modelos atmosféricos de mesoescala utilizam modelos globais de (re)análise como condições iniciais e de contorno para usos locais (HASSANLI; RAHIMZADEGAN, 2019; WEE *et al.*, 2012). Lee *et al.* (2020) aplicaram modelos de previsão numérica do tempo (*Numerical Weather Prediction* – NWP) de alta resolução (1,5 e 12 km), distribuídos pela *Korea Meteorological Administration* (KMA), como dados atmosféricos de entrada para a correção atmosférica e estimativa de temperatura da superfície do mar utilizando bandas do *Visible Infrared Imaging Radiometer Suite* (VIIRS). Esses dados KMA de NWP são restritos a Ásia Oriental, mas a abordagem adotada pelos autores de utilizar modelos de NWP de alta resolução combinados com RTM consiste em um *background* interessante para estudos relacionados com a correção atmosférica de dados de sensoriamento remoto no TIR.

O modelo *Weather Research and Forecasting* (WRF) (SKAMAROCK *et al.*, 2019) é um sistema de modelagem atmosférica desenvolvido tanto para pesquisa como para NWP. Atualmente, é o modelo de mesoescala mais utilizado no mundo (POWERS *et al.*, 2017). Não-hidrostático, gratuito, comunitário, de código aberto e com um amplo leque de opções de parametrizações, o modelo WRF proporciona recursos para uma variedade de aplicações em ciências atmosféricas (POWERS *et al.*, 2017; SKAMAROCK *et al.*, 2019; WANG *et al.*, 2019). Diante disso, o WRF tem sido amplamente empregado para estimar dados meteorológicos de alta resolução (EVANS; EKSTRÖM; JI, 2012; FEKIH; MOHAMED, 2019; GONZÁLEZ-ALONSO DE LINAJE; MATTAR; BORVARÁN, 2019; KIOUTSIOUKIS *et al.*, 2016; MOYA-ÁLVAREZ *et al.*, 2020; MYLONAS *et al.*, 2019; ONWUKWE; JACKSON, 2020; PRASAD; SHERWOOD; BROGNIEZ, 2020).

Sendo assim, é de grande importância analisar o potencial de utilização do modelo WRF em gerar perfis atmosféricos de alta resolução para, em conjunto com um RTM, permitir a realização de correções atmosféricas e de estimativas de LST mais precisas. Além disso, a maioria dos estudos que avaliam diferentes fontes de perfis atmosféricos para recuperação de LST foi realizada em áreas na Ásia e na Europa. Não se tem o conhecimento de trabalhos com esse objetivo na América do Sul. Existe também uma carência de estudos que utilizem sistemas de reanálise mais atuais e precisos, como o ERA5 (HERSBACH *et al.*, 2020) e o NCEP *Climate Forecast System Version* 2 (CFSv2) (SAHA *et al.*, 2014), para a correção atmosférica/estimativa de LST (VANHELLEMONT, 2020a, 2020b).

Nesse contexto, o presente estudo tem como objetivo avaliar o desempenho do modelo numérico WRF para simular perfis atmosféricos de alta resolução, melhorando a resolução espacial, vertical e temporal de reanálises globais, em especial do NCEP CFSv2. Assim, visa avaliar a aplicabilidade desses perfis na correção atmosférica de imagens termais e na recuperação da LST como uma alternativa mais precisa a necessidade de uma radiossondagem. Espera-se que a utilização do modelo WRF para refinar os dados de reanálise resulte em perfis atmosféricos mais próximos de uma radiossondagem local. Dessa forma, esse estudo buscará analisar se esse refinamento implicará em menores erros na correção atmosférica e em estimativas de LST mais acuradas, em comparação com a utilização de perfis diretamente extraídos dos dados de reanálise.

1.1 Objetivo geral

Este estudo tem como objetivo geral avaliar o desempenho do modelo numérico atmosférico WRF (*Weather Research and Forecasting*) na geração de perfis atmosféricos verticais para sua posterior aplicação em modelos de transferência radiativa, em substituição a dados de radiossondagens, visando à correção atmosférica de dados de sensoriamento remoto no infravermelho termal.

1.2 Objetivos específicos

- Realizar simulações numéricas de perfis atmosféricos com o modelo WRF no seu modo *Advanced Research WRF* (ARW) utilizando, como condições iniciais e de contorno, dados de reanálise NCEP CFSv2. Testando dois conjuntos de esquemas de parametrizações físicas, contendo as duas parametrizações de camada limite planetária mais utilizadas na literatura: *Yonsei University* e *Mellor–Yamada–Janjic*.
- Avaliar o desempenho do modelo WRF em descrever a distribuição vertical de algumas variáveis meteorológicas, por meio da comparação de perfis simulados com dados de campo provenientes do lançamento de radiossondas na área de estudo.
- Analisar a aplicação dos perfis simulados pelo WRF na estimativa dos parâmetros de correção atmosférica (por meio de um RTM) e de valores de LST (resolvendo a RTE, em conjunto com dados de radiância do Landsat 8 TIRS). Utilizando como referência os valores calculados a partir de radiossondagens *in situ*.
- Examinar o efeito do refinamento da resolução horizontal dos perfis verticais na correção atmosférica e recuperação de LST. Comparando os resultados dos perfis WRF com os da utilização de perfis diretamente extraídos de dados de reanálise NCEP CFSv2 e da Calculadora de Parâmetros de Correção Atmosférica (ACPC).

2 REFERENCIAL TEÓRICO

2.1 Sensoriamento Remoto no Infravermelho Termal

Todos os objetos com temperatura superior ao zero absoluto (0 K; -273,15 °C) emitem radiação eletromagnética (REM) (KUENZER *et al.*, 2013; LI *et al.*, 2013c). Portanto, todas as feições encontradas cotidianamente na paisagem terrestre, como vegetação, solo, rocha, água e os seres vivos, emitem REM infravermelha termal na porção correspondente do espectro (JENSEN, 2009). O infravermelho termal estende-se de comprimentos de onda próximos a 3 μm até cerca de 14 μm. Nessa faixa espectral, o mapeamento da superfície terrestre é possível devido às janelas atmosféricas existentes nas faixas de 3 a 5 μm e de 8 a 14 μm (LILLESAND; KIEFER; CHIPMAN, 2015; SABINS, 1986). Nessas janelas, a atmosfera permite que uma porção da energia infravermelha seja transmitida do terreno para os detectores remotos. Os instrumentos de sensoriamento remoto podem ser projetados para serem sensíveis apenas à energia infravermelha presente nas janelas atmosféricas. No caso do TIR, os detectores eletrônicos podem ser sensíveis a fótons de energia radiante infravermelha termal nas duas janelas mencionadas: 3 – 5 μm e 8 – 14 μm (JENSEN, 2009; KUENZER *et al.*, 2013; SCHMUGGE *et al.*, 2002).

Um conceito fundamental no sensoriamento remoto no TIR é o do corpo negro – uma entidade teórica hipotética que absorve e reemite toda a radiação incidente sobre ele (TANG; LI, 2014). A radiação emitida por um corpo negro é descrita pela Lei de Planck (Equação 1), a um determinado comprimento de onda, em função da temperatura absoluta do mesmo (PLANCK, 1901).

$$B_{\lambda}(T) = \frac{C_1}{\lambda^5 (e^{C_2/\lambda T} - 1)} \quad (1)$$

onde $B_{\lambda}(T)$ é a radiância espectral (W m^{-2} μm^{-1} sr^{-1}) de um corpo negro na temperatura T (em Kelvin) e no comprimento de onda λ (μm); C_1 (1,19104 x 10^8 W $\mu m^4\, m^{-2}\, sr^{-1}$) e C_2 (14387,7 μm K) são constantes físicas da radiação.

Todavia, como a maioria dos objetos naturais não são corpos negros ideais, a emissividade (ε) deve ser levada em consideração. Essa é definida como a razão entre a radiância de um objeto e a de um corpo negro à uma mesma temperatura. A

radiância desse objeto é, portanto, dada pela multiplicação de sua emissividade espectral pela Lei de Planck (LI *et al.*, 2013b, 2013c). O comprimento de onda do pico de radiação monocromática (comprimento de onda de máxima emissão, λ_{max}) a uma determinada temperatura (T) é dado pela Lei do Deslocamento de Wien (TANG; LI, 2014):

$$\lambda_{max} = \frac{2897{,}9\ [\mathrm{K\ \mu m}]}{T} \tag{2}$$

De acordo com a Equação 2, para temperaturas entre 250 e 330 K (a superfície terrestre apresenta uma temperatura média de 288 K, aproximadamente) o comprimento de onda de máxima emissão varia de 11,6 a 8,8 μm. A faixa espectral de 8 – 14 μm coincide justamente com a janela atmosférica mencionada anteriormente. Portanto, essa região do espectro aplica-se ao monitoramento termal de alvos como vegetação, solos, água e rochas, que apresentam temperaturas nessa faixa (LI *et al.*, 2013c). Contudo, o ozônio presente na atmosfera terrestre caracteriza-se como uma banda de absorção na região de 9,2 – 10,2 μm, absorvendo grande parte da energia termal emitida da superfície terrestre nessa faixa. Sendo assim, os sensores orbitais no infravermelho termal buscam evitar esta banda de absorção e, na prática, acabam por registrar dados na região de 10,5 – 12,5 μm (KUENZER *et al.*, 2013). O sensor Landsat 8 TIRS (*Thermal InfraRed Sensor*), por exemplo, possui bandas termais nas faixas de 10,60 – 11,19 μm e 11,50 – 12,51 μm (IHLEN; ZANTER, 2019; REUTER *et al.*, 2015). Já para temperaturas mais elevadas, o pico de emissão desloca-se para comprimentos de onda menores. A região de 3 – 5 μm é especialmente útil para o monitoramento de alvos de elevada temperatura, próximas a 800 K, como incêndios florestais e atividades geotermais (LI *et al.*, 2013c). Faz-se importante destacar que, no caso das janelas atmosféricas na faixa de 3 – 5 μm, tem-se o empecilho de que a radiação solar refletida ainda pode contaminar o sinal emitido (TIR) (KUENZER *et al.*, 2013).

Um sensor TIR a bordo de um satélite imageando a superfície terrestre registra a radiação da Terra e de sua atmosfera ao longo de uma linha de visada (LI *et al.*, 2013c). A partir dessa radiação mensurada, é possível derivar valores de

temperatura da superfície (LST). No sensoriamento remoto orbital, a LST pode ser definida como a temperatura radiométrica da superfície correspondente ao campo de visão instantâneo do sensor (DASH *et al.*, 2002; PRATA *et al.*, 1995). A LST representa o efeito integrado de um "conjunto" (*ensemble*) de objetos dentro de um pixel, portanto também está relacionada ao dispositivo de aquisição e sua resolução (BECKER; LI, 1995). Desse modo, faz-se importante diferenciar a LST de outras definições de temperatura, como termodinâmica ou cinética. Discussões a respeito de conceitos físicos e nomenclaturas de temperatura podem ser encontradas em Becker e Li (1995), Cao *et al.* (2019), Dash *et al*. (2002) e Norman e Becker (1995).

A radiância registrada por sensores orbitais TIR é resultante não somente dos parâmetros da superfície, mas também dos efeitos atmosféricos (LI *et al.*, 2013c; OTTLÉ; STOLL, 1993; PRATA *et al.*, 1995). Sendo assim, a estimativa de LST a partir de dados de sensoriamento remoto requer levar em consideração e compensar efeitos atmosféricos, angulares e de emissividade (DASH *et al.*, 2002). O presente estudo tem foco na correção atmosférica. Mais informações sobre efeitos direcionais e calibração radiométrica podem ser encontradas em Cao *et al.* (2019) e Tang e Li (2014), respectivamente, e de emissividade em Dash *et al.* (2002), Li *et al.* (2013b, 2013c) e Sekertekin e Bonafoni (2020a).

2.2 Correção atmosférica no TIR

Corrigir os efeitos da atmosfera no TIR, como já mencionado, é um passo essencial para a correta utilização dos dados termais, uma vez que o sinal que deixa um alvo na superfície é tanto atenuado como realçado pela atmosfera (BARSI *et al.*, 2005). Na região espectral de 8 – 14 μm, o vapor de água é o principal responsável pelos efeitos atmosféricos, ainda que haja uma banda de absorção de ozônio próxima a 9,5 μm (DASH *et al.*, 2002; JIMÉNEZ-MUÑOZ *et al.*, 2010; SOBRINO; COLL; CASELLES, 1991). A absorção e o espalhamento por aerossóis são insignificantes e, em geral, desprezados (JIMÉNEZ-MUÑOZ *et al.*, 2010; PRATA *et al.*, 1995). A correção atmosférica no TIR não é simples de ser implementada, uma vez que, usualmente, requer o conhecimento da distribuição do vapor de água e da temperatura na atmosfera, e ambos apresentam ampla variabilidade espaço temporal (DASH *et al.*, 2002; LI *et al.*, 2013c; PERRY; MORAN, 1994; SOBRINO; COLL; CASELLES, 1991).

Na grande maioria dos estudos, a correção atmosférica no termal ocorre com a recuperação de valores de LST da radiância no TOA, acoplada com a compensação dos efeitos da emissividade (JIMÉNEZ-MUÑOZ *et al.*, 2010). Nos últimos anos, muitos autores propuseram algoritmos para recuperar a LST com essa abordagem (BECKER; LI, 1990; CRISTÓBAL *et al.*, 2018; DU *et al.*, 2015; GILLESPIE *et al.*, 1998; JIMÉNEZ-MUÑOZ *et al.*, 2003; JIMÉNEZ-MUÑOZ *et al.*, 2009; MAO *et al.*, 2005; MENG *et al.*, 2019; PRICE, 1983; QIN; KARNIELI; BERLINER, 2001; YU; GUO; WU, 2014). Essas metodologias consideram as especificidades de vários sensores a bordo de diferentes satélites e se utilizam de variadas aproximações para a equação de transferência radiativa e para estimar a emissividade (LI *et al.*, 2013c).

De acordo com Sekertekin e Bonafoni (2020a), os algoritmos de recuperação de LST podem ser, simplificadamente, classificados de acordo com o número de bandas TIR que utilizam. Os algoritmos de canal único (*single-channel* ou *mono-window*) utilizam apenas uma banda TIR, enquanto os multicanais (*multi-channel*), em que estão incluídos os métodos *split-window*, utilizam mais de uma banda TIR. Li *et al.* (2013c) apresentam uma importante revisão dos métodos de recuperação de LST, enquanto outros autores compararam muitos desses algoritmos em diferentes regiões e condições atmosféricas e com diferentes resultados (ARABI ALIABAD; ZARE; GHAFARIAN MALAMIRI, 2021; GARCÍA-SANTOS *et al.*, 2018; HIDALGO GARCÍA; ARCO DÍAZ, 2021; JIMÉNEZ-MUÑOZ *et al.*, 2010; KÄFER *et al.*, 2020a, 2020b; SAJIB; WANG, 2020; SEKERTEKIN; BONAFONI, 2020a, 2020b; WANG; LU; YAO, 2019; WINDAHL; BEURS, 2016; YU; GUO; WU, 2014). De maneira geral, os algoritmos *split-window* são bastante populares devido ao seu bom equilíbrio entre simplicidade e desempenho – não necessitam de uma alta precisão nos dados atmosféricos de entrada (ARABI ALIABAD; ZARE; GHAFARIAN MALAMIRI, 2021; CHEN *et al.*, 2017; KÄFER *et al.*, 2020b). Essas técnicas utilizam duas bandas TIR (comumente entre 10 e 12 μm) e partem da premissa de que a atenuação da radiância pela absorção atmosférica é proporcional à diferença entre as medições simultâneas de radiância nos dois comprimentos de onda, sendo cada uma sujeita a diferentes quantidades de absorção atmosférica (JIMÉNEZ-MUÑOZ *et al.*, 2014; MCMILLIN, 1975). Por outro lado, os métodos *single-channel* possuem metodologias e teorias, baseadas na física, mais robustas, podendo apresentar performance

superior quando se dispõe de dados precisos do estado da atmosfera (DASH *et al.*, 2002; JIMÉNEZ-MUÑOZ *et al.*, 2009; KÄFER *et al.*, 2020b; YU; GUO; WU, 2014). A inversão direta da equação de transferência radiativa, que também pode ser considerada um método *single-channel*, é inclusive constantemente aplicada como referência em comparações e validações (JIMÉNEZ-MUÑOZ *et al.*, 2009, 2014; SOBRINO; JIMÉNEZ-MUÑOZ; PAOLINI, 2004).

2.2.1 Recuperação de LST baseada na RTE

A solução inversa da Equação de Transferência Radiativa (RTE) (PRICE, 1983) é um meio direto e, *a priori*, o procedimento mais adequado para recuperação da LST utilizando uma única banda termal (JIMÉNEZ-MUÑOZ *et al.*, 2009). Assumindo uma atmosfera sob condições de céu claro e em equilíbrio termodinâmico local e a superfície terrestre como um refletor Lambertiano (DASH *et al.*, 2002; SUSSKIND; ROSENFIELD; REUTER, 1983), a RTE, aplicada a uma banda/comprimento de onda (λ) em particular, pode ser simplificada conforme a Equação 3:

$$L_{\lambda}^{sen} = \left[\varepsilon_{\lambda} B_{\lambda}(T_s) + (1-\varepsilon_{\lambda}) L_{\lambda}^{\downarrow}\right]\tau_{\lambda} + L_{\lambda}^{\uparrow} \tag{3}$$

onde L_{λ}^{sen} (W·m^{-2}·sr^{-1}·μm^{-1}) é a radiância espectral para a banda TIR correspondente medida pelo sensor no TOA, ε_{λ} se refere a emissividade da superfície (adimensional), B_{λ} (W·m^{-2}·sr^{-1}·μm^{-1}) é a radiância do corpo negro, T_s (Kelvin) representa a LST, $L_{\lambda}^{\downarrow}$ e $L_{\lambda}^{\uparrow}$ (W·m^{-2}·sr^{-1}·μm^{-1}) são referentes as radiâncias atmosféricas de trajetória descendente (*downwelling*) e ascendente (*upwelling*), respectivamente, e τ_{λ} é a transmitância atmosférica (adimensional). Assim, a radiância emitida por um corpo negro à temperatura T_s é dada pela inversão da Equação 3:

$$B_{\lambda}(T_s) = \frac{L_{\lambda}^{sen} - L_{\lambda}^{\uparrow} - \tau_{\lambda}(1-\varepsilon_{\lambda}) L_{\lambda}^{\downarrow}}{\tau_{\lambda}\varepsilon_{\lambda}} \tag{4}$$

A temperatura da superfície pode ser então obtida substituindo e invertendo a Lei de Planck (Equação 1) na Equação 4:

$$T_s = \frac{C_2}{\lambda}\left[\ln\left(\frac{C_1}{\lambda^5\left[\frac{L_\lambda^{sen} - L_\lambda^{\uparrow}}{\varepsilon_\lambda \tau_\lambda} - \left(\frac{1-\varepsilon_\lambda}{\varepsilon_\lambda}\right) L_\lambda^{\downarrow}\right]} + 1\right)\right]^{-1} \quad (5)$$

Quando a RTE é aplicada a uma banda de um sensor específico, as magnitudes espectrais são calculadas de acordo com a função espectral de resposta dessa banda (JIMÉNEZ-MUÑOZ *et al.*, 2010). Daqui em diante, a notação do comprimento de onda/banda (λ) nesses termos espectrais pode ser suprimida por conveniência, uma vez que está se trabalhando com uma única banda. Nota-se que a Equação 5 inclui tanto a correção dos efeitos atmosféricos (τ, $L^{\uparrow}$ e $L^{\downarrow}$) como de emissividade da superfície (ε). A estimativa da LST com base na inversão da RTE requer conhecimento prévio dos parâmetros atmosféricos e da emissividade, como abordado nas seções a seguir.

2.2.2 Estimativa de parâmetros atmosféricos com um RTM

Os parâmetros atmosféricos (τ, $L^{\uparrow}$ e $L^{\downarrow}$) podem ser calculados por meio de um modelo de transferência radiativa (RTM) como os das séries MODTRAN (BERK *et al.*, 2014), 4A/OP (CHAUMAT *et al.*, 2012), 6S (KOTCHENOVA *et al.*, 2006; KOTCHENOVA; VERMOTE, 2007), libRadtran (EMDE *et al.*, 2016). Dentre esses, o modelo MODTRAN é amplamente aplicado para a correção atmosférica no TIR. (LI *et al.*, 2013c; MALAKAR *et al.*, 2018).

O MODTRAN é um modelo comercial desenvolvido pela Força Aérea dos Estados Unidos e pela empresa *Spectral Sciences Incorporated*. Esse RTM requer como *inputs* perfis atmosféricos de temperatura do ar, umidade relativa e pressão (Seção 2.2.3). As saídas do MODTRAN são fornecidas na resolução espectral do modelo. Portanto, uma integração precisa ser realizada entre os limites definidos

pela curva de resposta espectral da banda do sensor de interesse (TARDY *et al.*, 2016), como mostra a Equação 6:

$$var\ (\lambda_i)\ =\ \frac{\int_{\lambda_{i,min}}^{\lambda_{i,max}} var\ (\lambda) R_s(\lambda) d\lambda}{\int_{\lambda_{i,min}}^{\lambda_{i,max}} R_s(\lambda) d\lambda} \quad (6)$$

onde R_s é a resposta espectral do sensor no comprimento de onda central λ_i de uma banda com uma janela espectral de $\lambda_{i,min} - \lambda_{i,max}$. Por sua vez, var refere-se ao valor do parâmetro atmosférico (transmitância, *upwelling* ou *downwelling*).

2.2.3 Alternativas de perfis atmosféricos

Perfis verticais atmosféricos são essenciais como dados de entrada em RTMs para a correção atmosférica de dados TIR. Como mencionado anteriormente, esses dados são, em geral, derivados de medições com radiossondas, sondagens por satélite, ou ainda dados globais assimilados em um modelo numérico – reanálises (DUAN *et al.*, 2018; TONOOKA, 2001; YANG *et al.*, 2020). Perfis de radiossondagens podem ser considerados a situação ideal, uma vez que caracterizam o estado da atmosfera, em coordenadas específicas, com elevada precisão. Contudo, esses perfis estão disponíveis em locais e horários limitados (DE ROSA; DI GIROLAMO; SUMMA, 2020; FILIOGLOU *et al.*, 2017; RAJA *et al.*, 2008). Sendo assim, alternativas acabam por ser frequentemente utilizadas (MENG; CHENG, 2018; ROSAS; HOUBORG; MCCABE, 2017).

Dentre as fontes de perfis atmosféricos derivados de dados de satélites, destacam-se o *Atmospheric Infrared Sounder* (AIRS) (AUMANN *et al.*, 2003; DIAO *et al.*, 2013) e os produtos MOD07 (*MODIS atmospheric profiles product*) (BORBAS; MENZEL, 2017). Já no que se refere aos dados de reanálise de sistemas globais de previsão, são alternativas frequentes à substituição de dados de radiossondagem: NCEP/NCAR (*National Center for Atmospheric Research's) Reanalysis* 1 (R1) (KALNAY *et al.*, 1996) e NCEP/DOE (*United States Department of Energy*) *Reanalysis* 2 (R2) (KANAMITSU *et al.*, 2002), NCEP *Final Operational Model Global Tropospheric* Analyses (NCEP FNL) (NCEP *et al.*, 2000), NCEP *Global Forecast*

System (GFS) (NCEP *et al.*, 2007), NCEP *Climate Forecast System Reanalysis* (CFSR) (SAHA *et al.*, 2010) e *Climate Forecast System Version* 2 (CFSv2) (SAHA *et al.*, 2014), *European Centre for Medium-Range Weather Forecasts* (ECMWF) *Re-Analysis* (ERA-Interim) (DEE *et al.*, 2011) e ERA5 (HERSBACH *et al.*, 2020), *Modern Era Retrospective-Analysis for Research and Applications* (MERRA) (RIENECKER *et al.*, 2011), e *Japanese Reanalysis* (JRA) (KOBAYASHI *et al.*, 2015). A Tabela 1 apresenta as principais características desses produtos de perfis atmosféricos.

Tabela 1 – Resumo das características de diferentes fontes de perfis atmosféricos aplicados na correção atmosférica de dados TIR.

Tipo de dado	Fonte do dado	Disponibilidade dos dados	Resolução temporal	Resolução espacial	Resolução vertical
Perfis derivados de dados de satélite	AIRS	2002 – presente	2 vezes dia	1,0º x 1,0º	24 níveis
	MOD07	2000 – presente	2 vezes dia	5 km x 5 km	20 níveis
Perfis derivados de reanálise	NCEP/NCAR R1	1948 – presente	6 horas	2,5º x 2,5º	28 níveis
	NCEP/DOE R2	1979 – presente	6 horas	2,5º x 2,5º	28 níveis
	NCEP FNL	1999 – presente	6 horas	1,0º x 1,0º	26 níveis
	NCEP GFS	2007 – presente	6 horas	0,5º x 0,5º	31 níveis
	NCEP CFSR	1979 – 2011	6 horas	0,5º x 0,5º	37 níveis
	NCEP CFSv2	2011 – presente	6 horas	0,5º x 0,5º	37 níveis
	ERA-Interim	1979 – 2019	6 horas	0,7º x 0,7º	37 níveis
	ERA5	1950 – presente	1 hora	0,25º x 0,25º	37 níveis
	MERRA	1979 – 2016	3 e 6 horas	0,5º x 0,5º	42 níveis
	MERRA2	1980 – presente	3 e 6 horas	0,5º x 0,66º	42 níveis
	JRA-55	1958 – presente	6 horas	1,25º x 1,25º	27 níveis

Fonte: Elaboração própria.

Barsi; Barker e Schott (2003) propuseram a Calculadora de Parâmetros de Correção Atmosférica (*Atmospheric Correction Parameter Calculation* – ACPC), uma ferramenta de acesso público na web que fornece os três parâmetros atmosféricos

necessários para a correção das bandas termais dos sensores Landsat 5 TM, Landsat 7 ETM+ e Landsat 8 TIRS (banda 10). A ACPC utiliza perfis globais atmosféricos interpolados do NCEP FNL para data, hora e local específicos, fornecidos pelo usuário, como entrada para o código do MODTRAN. Espera-se que a ACPC possibilite a recuperação de valores de LST, globalmente, com viés de ±2K, onde a atmosfera é relativamente clara (BARSI *et al.*, 2005). Adicionalmente, a Calculadora também disponibiliza os perfis verticais interpolados.

Mattar *et al.* (2015) apresentaram uma base de dados, denominada *Global Atmospheric Profiles derived from Reanalysis Information* (GAPRI), que compila perfis verticais derivados de reanálises com o objetivo específico de atender à necessidade desses na estimativa de LST. A base de dados GAPRI inclui 8324 perfis atmosféricos derivados do ERA-Interim, extraídos no ano de 2011, em condições de céu claro e distribuídos ao redor do globo. Os perfis são disponibilizados no formato apropriado para serem inseridos no MODTRAN. Já Tardy *et al.* (2016) desenvolveram uma ferramenta em linguagem Python para estimar LST a partir de imagens termais Landsat, utilizando perfis atmosféricos do ERA-Interim e o código do MOTRAN. A validação feita pelos autores indicou valores de raiz do erro quadrático médio (*Root Mean Square Error* – RMSE) de 2,55 K e 1,84 K para áreas na França e na Tunísia, respectivamente.

Adicionalmente, estudos vêm sendo apresentados comparando o desempenho de diferentes fontes de perfis verticais na correção atmosférica de dados de sensoriamento remoto no TIR. Jiménez-Muñoz *et al.* (2010) compararam três diferentes fontes de perfis atmosféricos com radiossondagens locais (lançadas próximas à passagem do sensor): MOD07, NCEP FNL (gerados pela ACPC) e NCEP/NCAR R1 (modificado). Em termos de valores recuperados de LST, todos os produtos de perfis apresentaram resultados satisfatórios em comparação aos obtidos a partir de radiossondagens locais. Os maiores erros foram de 2 K com os perfis da ACPC para dados do Landsat 5 em uma área agrícola na Espanha.

Coll *et al.* (2012) analisaram a eficiência dos perfis de reanálise NCEP FNL/ACPC e dos provindos de sondagens por satélite AIRS e MOD07, em comparação com radiossondagens, para recuperação de valores de LST em uma área na Espanha e com dados dos sensores Landsat 7 ETM+, ASTER, MODIS e AATSR. Os resultados mostraram valores de RMSE de aproximadamente 1 K

quando utilizados os perfis NCEP FNL/ACPC e MOD07 e entre -1 K e -2 K para os perfis AIRS. Já Li *et al.* (2013a) avaliaram os produtos de perfis verticais NCEP FNL e MOD07 na recuperação de LST, através de medidas de campo na China e com dados do sensor HJ-1B *Infrared Scanner* (IRS). Ambos os produtos de perfis resultaram em valores de LST em concordância com as medidas de campo, com RMSE de 1,16 K e 1,21 K ao utilizar NCEP FNL e MOD07, respectivamente.

Pérez-Planells; García-Santos e Caselles (2015), por sua vez, buscaram comparar os perfis NCEP FNL (obtidos com a ACPC) e MOD07 com radiossondagens locais. Neste caso, a análise deu-se por meio da comparação dos parâmetros atmosféricos necessários para a correção: *upwelling*, *downwelling* e transmitância. O estudo foi realizado em três estações meteorológicas na Espanha e para as bandas 29, 31 e 32 do sensor MODIS. Os resultados da comparação das três fontes de perfis atmosféricos mostraram que os perfis NCEP FNL/ACPC caracterizaram a atmosfera de maneira mais eficiente do que os perfis MOD07. Os valores médios dos RMSEs resultantes foram: ±0,2 $W \cdot m^{-2}$ μm^{-1} sr^{-1} para a radiância *upwelling*; ±0,3 $W \cdot m^{-2}$ μm^{-1} sr^{-1} para a radiância *downwelling*; e ±0,03 para a transmitância atmosférica. Em termos de valores simulados de LST, os erros produziram um desvio de ±0,9 K.

Rosas, Houborg e Mccabe (2017) também avaliaram o impacto de diferentes perfis verticais na correção atmosférica e na estimativa da LST. Para tal, utilizaram perfis derivados de um banco de dados de radiossondagens, de produtos globais de reanálises (NCEP/NCAR R1 e ERA-Interim) e de sondagens por satélite (AIRS e MOD07). Sobre uma área agrícola em uma zona árida na Arábia Saudita, os resultados apresentaram um *range* absoluto médio entre 1,2 K e 1,8 K para solo exposto e entre 3,3 K e 3,8 K para áreas de cultivo de alfafa – com os perfis AIRS proporcionando as melhores estimativas para a região estudada. Meng e Cheng (2018) compararam oito produtos globais de reanálise (NCEP FNL; NCEP/DOE R2; MERRA-3h; MERRA-6h; MERRA2-3h; MERRA2-6h; JRA-55; e ERA-Interim) quando aplicados na correção atmosférica de dados da banda 10 do Landsat 8 TIRS. Para validação, foram utilizadas observações globais de radiossondagens de 163 estações e 32 imagens Landsat 8 TIRS10 sobre a China. Os resultados gerados com os produtos ERA-Interim e MERRA-6h foram os mais acurados em diferentes níveis de conteúdo de vapor de água na atmosfera e elevações da superfície. Os

valores globais de viés e RMSE, para LST, foram inferiores a 0,2 K e 1,09 K, respectivamente.

Recentemente, Yang *et al.* (2020) analisaram sete fontes de perfis verticais, contendo tanto dados de reanálise (ERA-Interim, MERRA2, NCEP FNL, NCEP/DOE R2 e NCEP GFS) como dados derivados de satélites (AIRS e MOD07). O estudo levou em consideração 17 estações de radiossondas na Europa, imagens Landsat 8 TIRS e medidas *in situ* de LST na China. Os resultados dos autores indicaram melhores desempenhos, na recuperação da LST, quando foram utilizados os perfis ECMWF, MERRA2, NCEP GFS e NCEP FNL – com valores de RMSE próximos a 1 K para LST, quando comparada com medidas de campo. De maneira geral, os estudos comparativos mostram um desempenho superior dos perfis de reanálise quando comparados àqueles provindos de dados de satélites, tanto na estimativa dos três parâmetros atmosféricos como na da LST. A exceção fica no artigo de Rosas, Houborg e Mccabe (2017). Esses resultados são explicados devido à dificuldade de se sincronizar os dados AIRS e MOD07 com as observações globais de radiossondas e com a passagem de muitos sensores TIR (COLL *et al.*, 2012; GALVE *et al.*, 2018; MENG; CHENG, 2018).

Ademais, Vanhellemont (2020a, 2020b) utilizou sistemas de reanálise mais modernos e refinados – CFSv2 e ERA5 – para a correção atmosférica e estimativa de LST. Lee *et al.* (2020), por sua vez, propuseram uma abordagem utilizando modelos de NWP de alta resolução para extrair os dados atmosféricos a serem aplicados no MODTRAN, com resultados competitivos. Apesar de os autores utilizarem modelos e dados de NWP disponíveis apenas para a Ásia Oriental, esse recente estudo constitui um passo interessante no que diz respeito à geração de perfis atmosféricos de alta resolução, utilizando modelos numéricos, visando o cálculo da LST por sensoriamento remoto.

2.3 Estimativa da Emissividade da Superfície Terrestre a partir do NDVI

A Emissividade da Superfície Terrestre (*Land Surface Emissivity* – LSE) é um dos parâmetros essenciais para calcular a LST a partir de dados de sensoriamento remoto. Essa é, por definição, uma medida da capacidade intrínseca da superfície de converter a energia térmica em energia radiante. A LSE é uma função da

composição, rugosidade e umidade da superfície e também das condições de observação da mesma (LI *et al.*, 2013b; SEKERTEKIN; BONAFONI, 2020a; SOBRINO; RAISSOUNI; LI, 2001). Li *et al.* (2013b) apresentam uma revisão e uma discussão detalhada dos métodos de estimativa de LSE a partir de dados de satélite. Já Sekertekin e Bonafoni (2020a) trazem uma tabela contendo uma atualização da revisão do trabalho anterior, mostrando o estado da arte dos métodos de cálculo da LSE, suas categorias e os sensores para os quais são aplicados.

Dentre esses métodos, os baseados no Índice de Vegetação por Diferença Normalizada (*Normalized Difference Vegetation Index* – NDVI) destacam-se por serem operacionais e apresentarem resultados satisfatórios (KÄFER *et al.*, 2019; LI; JIANG, 2018; SOBRINO *et al.*, 2008; SOBRINO; RAISSOUNI; LI, 2001; VALOR; CASELLES, 1996; VAN DE GRIEND; OWE, 1993; YU; GUO; WU, 2014). Essas metodologias são baseadas na alta correlação, relatada por Van de Griend e Owe (1993), entre a LSE e o logaritmo natural do NDVI para uma banda na faixa de 8 – 14 μm:

$$\varepsilon = a + b\ln(\mathrm{NDVI}) \tag{7}$$

sendo,

$$\mathrm{NDVI} = \frac{\rho_{NIR} - \rho_R}{\rho_{NIR} + \rho_R} \tag{8}$$

onde a e b são constantes derivadas por análise de regressão para uma área de estudo (LI *et al.*, 2013b). Já ρ_{NIR} e ρ_R são as reflectâncias das bandas do infravermelho próximo (*Near-InfraRed* – NIR) e do vermelho, respectivamente.

Inspirados nos trabalhos de Van de Griend e Owe (1993) e Valor e Caselles (1996), Sobrino e Raissouni (2000) e Sobrino *et al.* (2008) propuseram o NDVI *THresholds Method* ($\mathrm{NDVI}^{\mathrm{THM}}$). Essa metodologia utiliza certos valores de NDVI (*thresholds* = limiares) para distinguir pixels entre: solo exposto ($\mathrm{NDVI} < \mathrm{NDVI}_s$), vegetados ($\mathrm{NDVI} > \mathrm{NDVI}_v$) e pixels compostos tanto por solo como por vegetação ($\mathrm{NDVI}_s \leq \mathrm{NDVI} \leq \mathrm{NDVI}_v$). Sendo assim, a LSE dos pixels de uma imagem, de uma determinada banda (λ), é estimada de acordo com os seguintes critérios:

$$\varepsilon_\lambda = \begin{cases} a_\lambda + b_\lambda \rho_R & \text{NDVI} < \text{NDVI}_\text{s} \\ \varepsilon_{\text{v}\lambda} P_\text{V} + \varepsilon_{\text{s}\lambda}(1 - P_\text{V}) + d\varepsilon_\lambda & \text{NDVI}_\text{s} \leq NDVI \leq \text{NDVI}_\text{v} \\ \varepsilon_{\text{v}\lambda} + d\varepsilon_\lambda & NDVI > \text{NDVI}_\text{v} \end{cases} \quad (9)$$

onde a_λ e b_λ são coeficientes obtidos por regressão e dependentes da banda utilizada, NDVI_s e NDVI_v são os valores de NDVI limiares adotados para pixels de solo exposto e completamente vegetados, respectivamente. Esses limiares podem ser estimados através do histograma de toda cena ou adotados valores globais de referência (em geral, NDVI_s = 0,2 e NDVI_v = 0,5) (DASH *et al.*, 2005; LI *et al.*, 2013b; SEKERTEKIN; BONAFONI, 2020a; SOBRINO *et al.*, 2008; SOBRINO; JIMÉNEZ-MUÑOZ; PAOLINI, 2004; SOBRINO; RAISSOUNI, 2000). $\varepsilon_{\text{v}\lambda}$ e $\varepsilon_{\text{s}\lambda}$ são as emissividades, em um comprimento de onda específico, atribuidas à vegetação e ao solo, respectivamente, e ambas podem ser obtidas de medidas de campo ou de bibliotecas espectrais (LI *et al.*, 2013b). P_V é a proporção de vegetação (ou fração de cobertura) e pode ser obtido a partir do NDVI (CARLSON; RIPLEY, 1997):

$$P_V = \left[\frac{\text{NDVI} - \text{NDVI}_\text{s}}{\text{NDVI}_\text{v} - \text{NDVI}_\text{s}}\right]^2 \quad (10)$$

$d\varepsilon_\lambda$ é um termo que leva em consideração o “efeito de cavidade” (SOBRINO; CASELLES; BECKER, 1990; VALOR; CASELLES, 1996) devido à rugosidade da superfície ($d\varepsilon_\lambda$ = 0, para uma superfície plana). Pode ser calculado baseado na geometria da superfície, utilizando o modelo proposto por Sobrino; Caselles e Becker (1990):

$$d\varepsilon_\lambda = \varepsilon_{\text{s}\lambda}(1 - \varepsilon_{\text{s}\lambda})\varepsilon_{\text{v}\lambda} F'(1 - P_\text{V}) \quad (11)$$

onde F' é um fator geométrico que varia de 0 a 1, dependendo da distribuição da geometria da superfície. Por não poder ser estimado por sensoriamento remoto (visível, NIR e TIR), frequentemente o valor médio de 0,55 é adotado (SOBRINO *et al.*, 2008; SOBRINO; JIMÉNEZ-MUÑOZ; PAOLINI, 2004; SOBRINO; RAISSOUNI, 2000).

Devido a sua simplicidade e operacionalidade, o $NDVI^{THM}$ vem sendo amplamente aplicado com variados sensores orbitais. Sobrino *et al.* (2008) destacam que o método, por trabalhar apenas com bandas do visível e do NIR (VNIR), possibilita: sua aplicação, na recuperação de LST, em sensores com apenas uma banda na região do TIR e, também, o mapeamento da emissividade com uma resolução refinada, uma vez que as bandas no VNIR apresentam, em geral, maior resolução espacial que as do TIR. E ainda não é necessária uma correção atmosférica acurada das bandas VNIR para estimar os valores de P_V. Jiménez-Muñoz *et al.* (2009) testaram essa sensibilidade à correção atmosférica no cálculo da P_V e concluíram não haver grandes necessidades de realizar correções atmosféricas e radiométricas para a estimativa da P_V a partir de valores de NDVI escalonados (Equação 10) – no que se refere à recuperação de LST como objetivo.

Os fatores limitantes do $NDVI^{THM}$ residem, principalmente, no conhecimento da emissividade dos solos, que em alguns casos pode se fazer necessária, e na impossibilidade de sua aplicação em algumas superfícies como água, neve, gelo e rochas (SOBRINO *et al.*, 2008). Ademais, a estimativa de LSE por satélite sobre áreas urbanas ainda é um desafio e, portanto, invariavelmente, os diversos métodos existentes, incluindo aqueles baseados no NDVI, irão apresentar erros nesses ambientes (OLTRA-CARRIÓ *et al.*, 2012). Por outro lado, estudos recentes constataram que estimativas mais precisas de LSE não resultam em um aumento na acurácia da LST recuperada (NEINAVAZ; SKIDMORE; DARVISHZADEH, 2020) e que bons resultados no cálculo da LST podem ser obtidos até mesmo fixando a emissividade como 1 (VANHELLEMONT, 2020b). Por fim, é interessante destacar a análise comparativa realizada por Sekertekin e Bonafoni (2020a, 2020b), na qual os autores estudam seis métodos de estimativa de LSE baseados no NDVI para bandas termais Landsat.

2.4 Dados de satélite: Landsat 8

2.4.1 Visão geral

A missão Landsat vem proporcionando dados de observação da superfície terrestre, em resolução espacial moderada, por quase 50 anos. O Landsat 8,

lançado em fevereiro de 2013, é o mais recente satélite operacional da série. Esse possui dois sensores: o *Operational Land Imager* (OLI), que coleta dados em oito bandas no espectro refletido (VNIR e infravermelho de ondas curtas (*Short Wavelength InfraRed* – SWIR)) com resolução especial de 30 m, além de uma banda pancromática com resolução de 15 m; e o *Thermal InfraRed Sensor* (TIRS), com duas bandas nos comprimentos de onda do termal com resolução espacial de 100 m, reamostradas e disponibilizadas em 30 m para serem consistentes com as bandas OLI (IHLEN; ZANTER, 2019; ROY *et al.*, 2014). O período de revisita do Landsat 8 é de aproximadamente 16 dias. A Tabela 2 traz um resumo das características das bandas do Landsat 8.

Tabela 2 – Principais características das bandas do satélite Landsat 8.

Sensor	Número da banda	"Nome" da banda	Comprimento de onda (µm)	Resolução espacial (m)
OLI	1	Costa/aerossol	0,43 – 0,45	30
	2	Azul	0,45 – 0,51	30
	3	Verde	0,53 – 0,59	30
	4	Vermelho	0,64 – 0,67	30
	5	NIR	0,85 – 0,88	30
	6	SWIR 1	1,57 – 1,65	30
	7	SWIR 2	2,11 – 2,29	30
	8	Pancromática	0,50 – 0,68	15
	9	Cirrus	1,36 – 1,38	30
TIRS	10	TIRS 1	10,60 – 11,19	100
	11	TIRS 2	11,50 – 12,51	100

Fonte: Elaboração própria. Adaptado de Ihlen e Zanter (2019).

2.4.2 O sensor TIRS

Em termos de dados termais, a série Landsat oferece uma oportunidade interessante para recuperação de LST devido a sua disponibilidade de dados (de 1984, com o Landsat 4, até o presente) e resolução (YU; GUO; WU, 2014). Assim, as imagens TIR da missão vêm sendo amplamente aplicadas em estudos de

balanço de energia, ilhas de calor, agricultura, desastres naturais, atividades geotermais e gestão de recursos hídricos (ANDERSON *et al.*, 2012; GEMITZI; DALAMPAKIS; FALALAKIS, 2021; KHANAL; FULTON; SHEARER, 2017; LEMUS-CANOVAS *et al.*, 2020; ROCHA *et al.*, 2020; SOBRINO *et al.*, 2016; TAVARES *et al.*, 2020; WANG *et al.*, 2015).

Como mencionado anteriormente, o sensor TIRS do Landsat 8 conta com duas bandas termais (10 e 11, Figura 1). Todavia, em novembro de 2013, a equipe de calibração do Landsat alertou sobre o problema de *Stray Light* no sensor, que resultava em um erro considerável de calibração radiométrica absoluta para as imagens TIRS (BARSI *et al.*, 2014; MONTANARO *et al.*, 2014a, 2014b; REUTER *et al.*, 2015). Essa imprecisão na calibração afetava em especial a banda 11, dificultando a aplicação de métodos *split-window*. Portanto, o *United States Geological Survey* (USGS) passou a recomendar o uso de algoritmos *single-channel*, utilizando a banda 10, para recuperar LST (CRISTÓBAL *et al.*, 2018; GUO *et al.*, 2020; SEKERTEKIN; BONAFONI, 2020b). Além disso, a banda 10 está localizada em uma região de menor absorção atmosférica (altos valores de transmitância), o que torna o seu uso preferível para os métodos de canal único (JIMÉNEZ-MUÑOZ *et al.*, 2014).

Figura 1 – Função resposta espectral das bandas do sensor TIRS do Landsat 8.

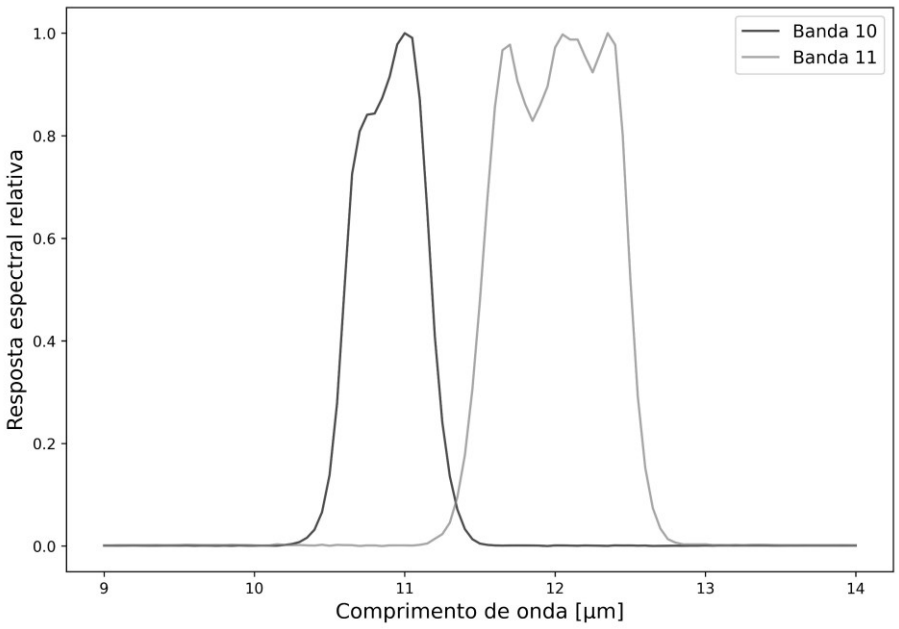

Fonte: Elaboração própria.

Cabe destacar que estudos visando calibração e correção dos erros devido ao *Stray Light* continuaram em progresso, com algoritmos sendo propostos (GERACE; MONTANARO, 2017; MONTANARO; GERACE; ROHRBACH, 2015), e a última atualização do USGS nesse sentido é de dezembro de 2019 (usgs.gov/core-science-systems/nli/landsat/landsat-8-oli-and-tirs-calibration-notices). Análises recentes dessa recalibração das bandas do sensor TIRS e da correção do efeito *Stray Light* podem ser encontradas em Guo *et al*. (2020) e Niclòs *et al*. (2021).

2.5 O Modelo WRF

Como o próprio nome indica, o WRF é um sistema de simulação atmosférica desenvolvido tanto para aplicações operacionais (NWP) como para pesquisa. Disponibilizado para o público em 2000, o WRF é um modelo de mesoescala de última geração, sendo, atualmente, o modelo atmosférico mais utilizado no mundo. Ainda que oficialmente seja mantido pelo NCAR, o WRF recebe contribuições de uma base mundial de usuários, o que o torna um legítimo modelo comunitário. Dessa forma, está em constate aperfeiçoamento e oferece uma variedade de recursos para uma ampla gama de aplicações na previsão/simulação de sistemas terrestres como hidrologia, poluição atmosférica, furacões, energia solar e eólica, incêndios florestais, simulações climáticas e meteorologia urbana (POWERS *et al.*, 2017; SKAMAROCK *et al.*, 2019).

O processo de realização das simulações atmosféricas no WRF se divide, basicamente, em três etapas: a primeira, destina-se a configurar os domínios do modelo, isto é, inserir os dados de entrada e preparar as condições iniciais e de contorno; já a segunda consiste na execução do modelo numérico propriamente dito; e a terceira etapa é a de pós-processamento e visualização dos dados. As simulações iniciam com o sistema de pré-processamento do WRF – o *WRF Preprocessing System* (WPS). Primeiramente, o WPS extrai informações geográficas (como topografia e uso do solo) para os domínios configurados pelo usuário. Em seguida, incorpora, reformata e interpola os dados atmosféricos necessários para serem utilizados como condições iniciais no modelo (por exemplo, os dados de (re)análise de um modelo global), também de acordo com os domínios configurados para a simulação (POWERS *et al.*, 2017; SKAMAROCK *et al.*, 2019).

Esses *inputs* são distribuídos nos níveis verticais do modelo e as condições de contorno laterais são geradas. O modelo WRF está então pronto para ser executado. Isso é feito pelo componente de previsão que contém o núcleo solucionador dinâmico e os pacotes de parametrizações físicas para processos atmosféricos que não podem ser representados explicitamente pelo modelo numérico (ver Seção 2.5.1). Existem dois núcleos dinâmicos na estrutura de software do WRF: o núcleo de Pesquisas Avançadas (*Advanced Research WRF* – ARW), desenvolvido primeiramente no NCAR, e o *Nonhydrostatic Mesoscale Model* (NMM), desenvolvido pelo NCEP. Por fim, após serem realizadas as simulações numéricas, ocorre o pós-processamento das informações, isto é, a extração dos dados de interesse, sua leitura, verificação e disponibilização para uma ferramenta gráfica de visualização, para que, então, sejam realizadas a geração e a análise de resultados (POWERS *et al.*, 2017; SKAMAROCK *et al.*, 2019; WANG *et al.*, 2019).

A Figura 2 apresenta um fluxograma do sistema de modelagem do WRF-ARW, onde as etapas utilizadas no presente estudo estão destacadas pelas células coloridas em tons de verde. Cabe salientar que o WRF apresenta também: a possibilidade de ser configurado para simulações idealizadas; um sistema de assimilação de dados – o *WRF Data Assimilation System* (WRFDA); e modelos acoplados especializados, como o WRF-Chem (química atmosférica), o WRF-Hydro (modelagem hidrológica) e o WRF-Fire (modelagem de incêndios florestais). Mais detalhes a respeito dos componentes e operação do WRF, além das equações governantes do modelo, podem ser encontrados em Skamarock *et al.* (2019) e Wang *et al.* (2019).

Figura 2 – Fluxograma do sistema de modelagem do WRF-ARW. As etapas que foram utilizadas neste projeto estão destacas nas células coloridas do fluxograma.

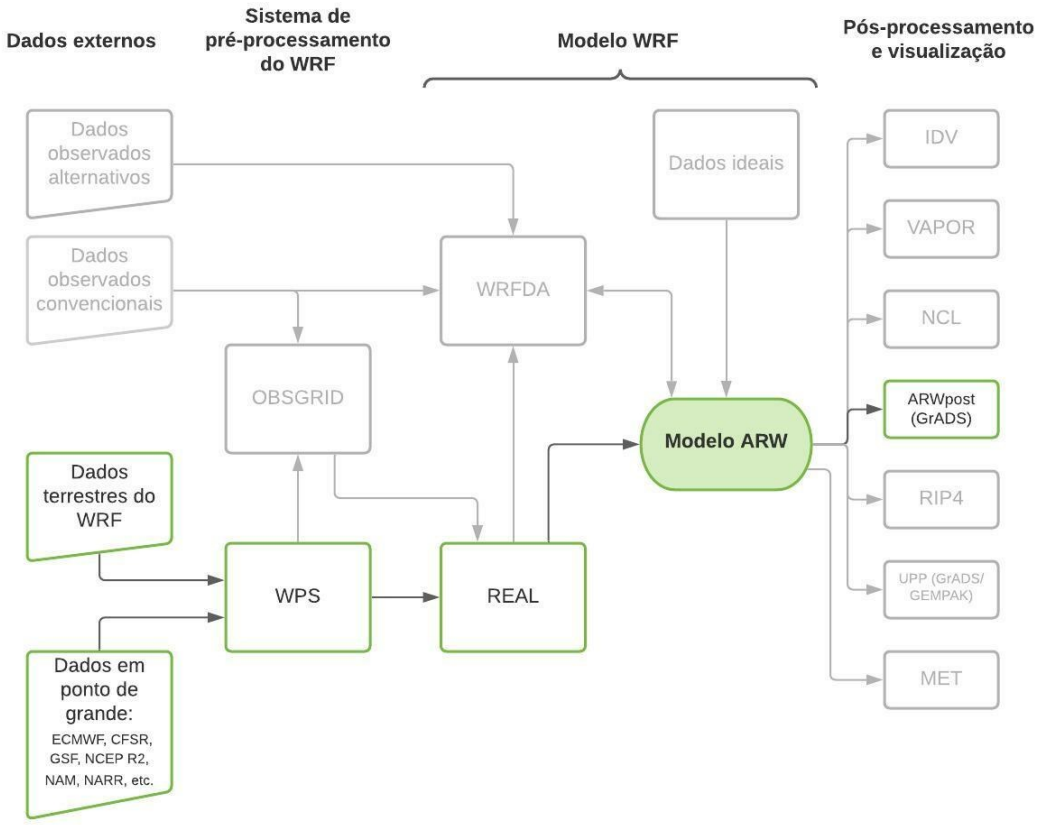

Fonte: Elaboração própria. Adaptado de Wang *et al*. (2019).

2.5.1 Parametrização de camada limite atmosférica no WRF

Muitos processos físicos importantes da atmosfera não podem ser resolvidos completamente por um modelo numérico e, por tanto, precisam ser parametrizados. Os esquemas de parametrização descrevem a contribuição desses fenômenos "não resolvidos" em termos de variáveis resolvidas na grade discreta do modelo (GARCÍA-DÍEZ *et al.*, 2013; STENSRUD, 2007; XIE *et al.*, 2012). Dentre esses processos, a parametrização de camada limite planetária (*Planetary Boundary Layer* – PBL) é crucial para a simulação de variáveis meteorológicas (HU; NIELSEN-GAMMON; ZHANG, 2010; JIA; ZHANG, 2020). A PBL é a porção da troposfera mais próxima da superfície, sendo caracterizada pelo atrito e mistura turbulenta (STULL, 2017). Essa camada desempenha um importante papel no transporte de energia para os níveis superiores da atmosfera e atua como um mecanismo de *feedback* na circulação atmosférica.

Os esquemas de parametrização de PBL são responsáveis pela representação da transferência de calor, umidade e momento entre a superfície e a atmosfera, pelo mecanismo dominante – fluxos turbulentos, que não é resolvido explicitamente pelos modelos numéricos (HOLT; RAMAN, 1988; STENSRUD, 2007; STULL, 2017). A espessura e a estrutura da camada limite são determinadas pelas propriedades físicas e térmicas da superfície subjacente, juntamente com a dinâmica e a termodinâmica da baixa atmosfera (BOADH *et al.*, 2016; GARRATT, 1994; MADALA; SATYANARAYANA; RAO, 2014).

Uma simulação acurada da estrutura da PBL é fundamental para pesquisas atmosféricas, NWP e estudos ambientais. Perfis verticais de temperatura e vapor de água, por exemplo, podem apresentar variações entre os esquemas de PBL dentro da mesma e, em consequência, ao longo de toda coluna atmosférica e todo domínio do modelo (CHAOUCH *et al.*, 2017; CUCHIARA *et al.*, 2014; HARIPRASAD *et al.*, 2014; HU; NIELSEN-GAMMON; ZHANG, 2010; XIE *et al.*, 2012). Além disso, é na camada limite que estão localizadas as maiores concentrações de vapor de água da atmosfera, o que reforça a importância dessa camada para a correção atmosférica de imagens TIR (JIMÉNEZ-MUÑOZ et al., 2010; SOBRINO; COLL; CASELLES, 1991).

O Modelo WRF apresenta uma variedade de opções de esquemas de parametrizações físicas, e não é diferente para os esquemas de PBL. Esses podem ser classificados em dois grupos principais: esquemas de fechamento local e não-local. Nos esquemas de fechamento local, apenas os níveis verticais imediatamente adjacentes a um dado ponto influenciam diretamente a estimativa das variáveis nesse ponto. Já os esquemas de fechamento não-local, podem utilizar múltiplos níveis verticais para estimar variáveis em um dado ponto (COHEN *et al.*, 2015; ONWUKWE; JACKSON, 2020). Estudos analisando a sensibilidade do WRF a diferentes esquemas de parametrização de PBL vêm sendo realizados ao longo dos anos (BANKS *et al.*, 2016; CONIGLIO *et al.*, 2013; CUCHIARA *et al.*, 2014; FEKIH; MOHAMED, 2019; HARIPRASAD *et al.*, 2014; HU; NIELSEN-GAMMON; ZHANG, 2010; MADALA; SATYANARAYANA; RAO, 2014; ONWUKWE; JACKSON, 2020; SHIN; HONG, 2011; TYAGI *et al.*, 2018; XIE *et al.*, 2012, 2013). De maneira geral, diferentes resultados foram reportados e as conclusões têm dependência local, sazonal, temporal e da variável analisada (DE LANGE *et al.*, 2021; GARCÍA-DÍEZ *et*

al., 2013). Portanto, a realização de estudos locais é de suma importância (CHAOUCH *et al.*, 2017).

Nesse trabalho, foram avaliados os dois esquemas de parametrização de PBL mais utilizados pela comunidade científica – um de fechamento local e outro de fechamento não-local. Nas seções a seguir, é apresentada uma breve descrição desses esquemas. Cohen *et al.* (2015) e Jia e Zhang (2020) proporcionam revisões sobre os esquemas de camada limite disponíveis no modelo WRF. Mais informações sobre as opções de parametrizações de PBL no WRF podem ser encontradas nesses estudos, bem como nos manuais do modelo (SKAMAROCK *et al.*, 2019; WANG *et al.*, 2019).

2.5.2 Os esquemas de PBL Yonsei University e Mellor–Yamada–Janjic

O esquema *Yonsei University* (YSU) (HONG; NOH; DUDHIA, 2006) é um esquema de primeira-ordem, de fechamento não-local, com um tratamento explícito do topo da camada limite (SIUTA; WEST; STULL, 2017). Esse esquema veio como uma evolução do esquema *Medium-Range Forecast Model* (MRF) (HONG; PAN, 1996). O esquema YSU geralmente trabalha melhor sob condições atmosféricas instáveis/convectivas. O oposto ocorre para condições estáveis, uma vez que essa configuração tende a subestimar a razão de mistura do vapor de água devido a grande quantidade de mistura vertical provinda dos grandes turbilhões (CHAOUCH *et al.*, 2017; SHIN; HONG, 2011). Em camadas limites convectivas diurnas, pode vir a produzir condições muito quentes e secas na PBL, resultantes do *overmixing* (CONIGLIO *et al.*, 2013). O esquema YSU é considerado o esquema de parametrização de PBL mais utilizado na literatura (JIA; ZHANG, 2020).

Por sua vez, o esquema *Mellor–Yamada–Janjic* (MYJ) (JANJIĆ, 1994) é de fechamento local e de “uma ordem e meia” (“*1.5-order*”). O fechamento local implica que apenas pequenas contribuições sejam consideradas para a distribuição da energia cinética turbulenta (equação prognóstica), uma vez que esse não considera os impactos dos efeitos não-locais (JIA; ZHANG, 2020; SIUTA; WEST; STULL, 2017). Tradicionalmente, a utilização do esquema MYJ gera bons resultados em atmosferas estáveis, mas, por outro lado, tende a gerar condições muito frias e úmidas próximas a superfície para camadas limites convectivas diurnas – resultado da pouca mistura na camada (CONIGLIO *et al.*, 2013). Devido ao seu baixo custo

computacional em relação a outros esquemas de PBL, o MYJ é amplamente aplicado. Pode ser considerado o mais popular entre os esquemas locais, ficando atrás apenas do YSU, quando considerados todos os tipos de fechamentos (JIA; ZHANG, 2020). As equações envolvidas nos dois esquemas de PBL aqui apresentados podem ser encontradas nos artigos de referência dos mesmos (HONG; NOH; DUDHIA, 2006; JANJIĆ, 1994).

3 RESULTADOS E DISCUSSÕES

3.1 Artigo 1: Reanalysis profile downscaling with WRF model and sensitivity to PBL parameterization schemes over a subtropical station

Artigo publicado no periódico "*Journal of Atmospheric and Solar-Terrestrial Physics*" e que visa atender os dois primeiros objetivos específicos da presente dissertação.

DIAZ, L. R. *et al.* Reanalysis profile downscaling with WRF model and sensitivity to PBL parameterization schemes over a subtropical station. **Journal of Atmospheric and Solar-Terrestrial Physics**, v. 222, p. 105724, 2021. Disponível em: https://linkinghub.elsevier.com/retrieve/pii/S1364682621001784.

Journal of Atmospheric and Solar–Terrestrial Physics 222 (2021) 105724

Contents lists available at ScienceDirect

Journal of Atmospheric and Solar-Terrestrial Physics

journal homepage: www.elsevier.com/locate/jastp

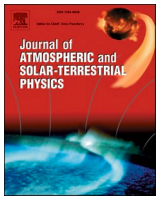

Reanalysis profile downscaling with WRF model and sensitivity to PBL parameterization schemes over a subtropical station

Lucas Ribeiro Diaz [a,*], Daniel Caetano Santos [b], Pâmela Suélen Käfer [a], María Luján Iglesias [a], Nájila Souza da Rocha [a], Savannah Tâmara Lemos da Costa [a], Eduardo Andre Kaiser [a], Silvia Beatriz Alves Rolim [a]

[a] Universidade Federal do Rio Grande do Sul (UFRGS), State Research Center for Remote Sensing and Meteorology (CEPSRM), Av. Bento Gonçalves, 9500, Campus do Vale, Porto Alegre, RS, Brazil

[b] Universidade Federal de Santa Maria (UFSM), Center for Natural and Exact Sciences, Department of Physics, Av. Roraima, Santa Maria, RS, Brazil

ARTICLE INFO

Keywords:
NCEP CFSv2
Atmospheric correction
Yonsei University (YSU)
Mellor–Yamada–Janjic (MYJ)

ABSTRACT

Atmospheric profiles are essential in weather prediction, atmospheric research, and satellite data calibration. In this study, we assess the use of the Weather Research and Forecasting (WRF) model to downscaling NCEP Climate Forecast System Version 2 (CFSv2) reanalysis atmospheric profiles. Moreover, a sensitivity analysis was conducted to Yonsei University (YSU) and Mellor–Yamada–Janjic (MYJ) Planetary Boundary Layer (PBL) parameterization schemes. WRF simulations were carried out using two nested grids with horizontal resolutions of 12 and 3 km. Simulated profiles were evaluated against radiosonde observations in Southern Brazil. Results indicate that WRF can skillfully simulate vertical profiles of water vapor mixing ratio (q) and potential temperature (θ). The entire profile comparison yielded high correlation coefficients (mostly higher than 0.9), low moist and cold average biases, and overall RMSE (MAE) of 0.84 (0.44) g/Kg and 2.30 (1.61) K for q and θ, respectively. In the lower troposphere (0–3 km), errors are larger for q and lower for θ. Statistically, there is no significant difference in the retrieved profiles on increasing the horizontal resolution. The setting choice is a compromise between spatial detail needs and computational cost. Furthermore, the overall results did not indicate any particular PBL scheme that stands out in all case days. The performance depends on the meteorological conditions that prevail in the different cases. The WRF model and even data directly from NCEP CFSv2 reanalysis are useful to represent the vertical structure of the atmosphere when local radiosondes are not available.

1. Introduction

The vertical distribution of atmospheric parameters is crucial to understand global atmospheric circulation, hydrologic cycle, and local dynamic processes (Chang et al., 2020; Hassanli and Rahimzadegan, 2019; Sobrino et al., 2015). Accurate monitoring on global and regional scales of temperature and water vapor is essential for assessing climate changes (Chang et al., 2020; Hersbach et al., 2020; Rao et al., 2020; Sobrino et al., 2015) These parameters play a key role in Earth's energy balance and thermodynamic state of the atmosphere (De Rosa et al., 2020; Held and Soden, 2000; Jiang et al., 2019; Sherwood et al., 2010; Thorne et al., 2005). Moreover, temperature and water vapor vertical profiles are required for Numerical Weather Prediction (NWP) (Naakka et al., 2019; Turner et al., 2000; Zhao et al., 2020) and in the atmospheric correction of optical satellite imagery (Jiménez-Muñoz et al., 2010).

Radiosonde profiles characterize the atmospheric conditions at a specific location with high accuracy. Nevertheless, they are available only in limited sites (mostly in or near urban settlements) and times (typically 00:00 and 12:00 UTC) (De Rosa et al., 2020; Filioglou et al., 2017; Raja et al., 2008). Radiosondes are also high in cost and their observational networks are geographically sparse in South America (Chang et al., 2020; Diaz et al., 2020; Li et al., 2003; Xu et al., 2015). Thus, radiosonde-recorded data are particularly regarded as the truth

* Corresponding author.
E-mail addresses: lucas.diaz@ufrgs.br (L.R. Diaz), danielcae@gmail.com (D.C. Santos), pamelaskafer@gmail.com (P.S. Käfer), lujaniglesias@gmail.com (M.L. Iglesias), najila.rocha@ufrgs.br (N.S. da Rocha), savannah.lemos@ufrgs.br (S.T.L. da Costa), kaiser-eduardo@hotmail.com (E.A. Kaiser), silvia.rolim@ufrgs.br (S.B.A. Rolim).

https://doi.org/10.1016/j.jastp.2021.105724
Received 18 May 2021; Received in revised form 22 July 2021; Accepted 27 July 2021
Available online 30 July 2021
1364-6826/

value in atmospheric research and for calibration and validation of satellite data (Divakarla et al., 2006; Meng and Cheng, 2018; Rao et al., 2020; Zhao et al., 2020). Reanalysis profiles from global NWP models supply a practical alternative to the radiosondes spatial constraint and provide a flexible temporal resolution that can match the applications demands (Rosas et al., 2017). These datasets are global gridded with an extended homogeneous time series, i.e., no spatial and temporal gaps (Alghamdi, 2020; Chen and Liu, 2016; Dee et al., 2011). They are delivered at low spatial resolution (several degrees) each 1, 3, or 6 h, varying for each product (Wang and Zeng, 2012; Yang et al., 2020). To this end, NWP outputs, data assimilation techniques, and observations from several variables and sources are integrated (Alghamdi, 2020; Mooney et al., 2011).

A remarkable application of reanalysis profiles is in the atmospheric correction of remote sensing data (from visible to thermal infrared spectral regions) to retrieve accurate bio-geophysical parameters from the Earth surface. Regarding the TIR range, the water vapor is the main constituent involved in the signal atmospheric perturbation (Jiménez-Muñoz et al., 2010; Li et al., 2013). Thermal infrared (TIR) remote sensing is a singular way of estimating the land surface temperature (LST) from different scales (Meng and Cheng, 2018; Rosas et al., 2017) and this variable is a key element connected to the surface energy exchange (Tardy et al., 2016). Consequently, LST is a powerful tool in studies of evapotranspiration (Rocha et al., 2020), geothermal activity (Chan et al., 2018), forest fire detection (Maffei et al., 2018), drought monitoring (Khanal et al., 2017), urban heat islands (Lemus--Canovas et al., 2020), and natural disasters (Sekertekin et al., 2020).

Even though global reanalysis data are largely applied in scientific research, their precision is usually lower for regions with poor permanent observatories coverage, such as the oceans and many Southern Hemisphere countries (Alghamdi, 2020; Chen and Liu, 2016; Chen et al., 2014; Tonooka, 2001). Their accuracy of meteorological phenomena on a sub-grid or variable time scale can be affected since they are spaced at grid points with time intervals of typically 6 h (Tonooka, 2001). Additionally, due to differences mainly in local atmospheric processes and topography, reanalysis data efficiency is local, time, and weather dependent (Alghamdi, 2020; Mooney et al., 2011; Schafer et al., 2003). Thus, most studies assessing reanalysis sources performance have not demonstrated broad conclusions due to varied regional climatic conditions (Alghamdi, 2020; Bao and Zhang, 2013, 2019). Chen et al. (2014) pointed out that reanalysis datasets may have uncertainties at a regional scale and care should be taken when using these data for specific sites. Therefore, coarse global reanalysis may not be appropriate for local studies (Hassanli and Rahimzadegan, 2019).

Contemporary numerical weather models own greater computer capabilities and physical processes parameterizations to refine the resolution of reanalysis data. Using global models outputs as initial and boundary conditions, mesoscale atmospheric models are applied for local research and forecast purposes (Hassanli and Rahimzadegan, 2019; Wee et al., 2012). The Weather Research and Forecasting (WRF) model (Skamarock et al., 2019) is a next-generation atmospheric modeling system designed for both NWP and meteorological research. Non-hydrostatic, open-source, free, and community-based, the WRF model supply specialized assets for a diversity of applications in Earth systems (Powers et al., 2017).

The WRF is among the most employed mesoscale models for simulating high-resolution meteorological data (Fekih and Mohamed, 2019; Hassanli and Rahimzadegan, 2019; Knievel et al., 2007; Powers et al., 2017). However, many atmospheric phenomena cannot be completely resolved by the numerical model and need to be parameterized. Parameterization schemes represent the contribution of these unresolved physical processes in terms of variables resolved at the model discrete grid (García-Díez et al., 2013; Stensrud, 2007; Xie et al., 2012). Among them, the Planetary Boundary Layer (PBL) parameterization is crucial to the simulation of meteorological properties (Hu et al., 2010; Jia and Zhang, 2020; Xie et al., 2012). PBL is the portion of the troposphere closest to the ground level, characterized by friction and turbulent mixing (Stull, 2017). It plays a key role in the transportation of energy (momentum, heat, moisture) into the upper layers of the atmosphere and acts as a feedback mechanism in atmospheric circulation (Boadh et al., 2016; Garratt, 1994; Madala et al., 2014; Stull, 2017). Vertical profiles of water vapor and temperature may display variations among the PBL schemes across the boundary layer depth and subsequently the entire atmospheric column and the whole model domain (Chaouch et al., 2017; Cuchiara et al., 2014; Hariprasad et al., 2014; Hu et al., 2010; Xie et al., 2012). Furthermore, the largest concentrations of atmospheric water vapor are in the PBL, which reinforces its importance for TIR satellite imagery atmospheric correction (Jiménez-Muñoz et al., 2010; Sobrino et al., 1991).

The WRF model has a wide range of physical parameterization options, including the boundary layer ones. A number of sensitivity studies to PBL schemes have been carried out with WRF (Banks et al., 2016; Coniglio et al., 2013; Cuchiara et al., 2014; de Lange et al., 2021; Fekih and Mohamed, 2019; Hariprasad et al., 2014; Hu et al., 2010; Madala et al., 2014; Onwukwe and Jackson, 2020; Shin and Hong, 2011; Tyagi et al., 2018; Xie et al, 2012, 2013). In general, different results were reported and conclusions are site-specific. Thus, local studies should be performed for a precise evaluation (Chaouch et al., 2017). Additionally, García-Díez et al. (2013) demonstrated that the WRF performance using different PBL parameterizations is influenced by the distinct atmospheric conditions at different times of day and seasons of the year.

Most of these studies evaluating PBL schemes (as well as for the other physical parameterizations) are basically distributed in North America, Europe, and Asia (Jia and Zhang, 2020). There is a general lack of sensitivity studies on the effect of different PBL parameterization schemes over South America (González-Alonso de Linaje et al., 2019; Moya-Álvarez et al., 2020; Ruiz et al., 2010; Santos and Nascimento, 2016). Besides, the majority of these works analyze surface parameters (e.g., temperature, relative humidity, and wind speed/direction), PBL height, turbulent diffusion coefficients, and vertical profiles of potential temperature, water vapor mixing ratio, and wind speed within PBL depth. Few papers look over the influence of PBL schemes in the entire atmospheric profile (Chaouch et al., 2017; Prasad et al., 2020).

This work aims to evaluate the potential of the WRF as a tool to downscaling reanalysis atmospheric profiles to their use in future assessments for atmospheric correction of TIR remote sensing images. We expect to generate high-resolution vertical profiles as an alternative to the need for a radiosonde. This study conducts WRF simulations using as initial and boundary conditions the National Centers for Environmental Prediction (NCEP) Climate Forecast System Version 2 (CFSv2) (Saha et al., 2014) reanalysis data. In addition, a sensitivity analysis was carried out with the two widely used PBL schemes: the nonlocal Yonsei University (YSU) (Hong et al., 2006) and the local Mellor–Yamada–Janjic (MYJ) (Janjić, 1994). Since each PBL scheme is tied to a particular surface-layer scheme, Revised MM5 (Jiménez et al., 2012) and Eta Similarity (Janjić, 1994, 1996, 2002; Monin and Obukhov, 1954) schemes were used, respectively. The model simulations were evaluated with available radiosonde observations at a station in Southern Brazil. We analyzed water vapor and temperature profiles in the lower troposphere and throughout the entire model atmospheric column.

2. Study area and case days

In this study, the radiosonde station of the Porto Alegre International Airport, Rio Grande do Sul State, Brazil was selected as the study area. The station is located at 30.00° S and 51.18° W, with a 3.0 m elevation above mean sea level. The station's global identifier name is SBPA and its number is 83971. The local climate is subtropical humid with hot summers (Cfa), in Köppen's climate classification (Alvares et al., 2013), with a mean annual air temperature of 19.6 °C, annual precipitation around 1397 mm, and mean annual relative humidity of 76.1%

(Matzenauer et al., 2011). Fig. 1 shows the location of the SBPA station. In this station, radiosondes are launched twice a day, at 00:00 and 12:00 UTC.

As we are particularly interested in the performance of high-resolution vertical profiles for atmospheric correction of TIR remote sensing data purposes, the study is developed only for dates coinciding with the Landsat 8 overpass and under clear-sky conditions. Table 1 shows the dates used in this paper, i.e., the 27 days when clear-sky Landsat 8 images were available from 2013 to 2019.

Table 1
Dates used to perform the study.

Year	Day and Month (Case Day)					
2013	18 Nov (1)	04 Dec (2)				
2014	06 Feb (3)	20 Oct (4)	07 Dec (5)			
2015	24 Jan (6)	25 Feb (7)	08 Nov (8)			
2016	15 Mar (9)	22 Aug (10)	12 Dec (11)			
2017	03 Apr (12)	22 Jun (13)	24 Jul (14)	25 Aug (15)	13 Nov (16)	15 Dec (17)
2018	17 Feb (18)	22 Apr (19)	09 Jun (20)	28 Aug (21)	29 Sep (22)	16 Nov (23)
2019	24 Mar (24)	09 Apr (25)	15 Aug (26)	19 Nov (27)		

3. Data and methods

3.1. In situ radiosonde observations

Radiosonde consists of sensors (temperature, pressure, and humidity) integrated into a light structure, which is released into the atmosphere by a meteorological helium balloon. The meteorological variables are measured and transmitted to the surface by radio signals with the aid of a ground station. The radiosonde launch allows characterizing the vertical structure of the atmosphere with profiles of air temperature, pressure, humidity. Here, radiosonde data of SBPA were obtained from the University of Wyoming website (http://weather.uwyo.edu/upperair/sounding.html) for the 27 days presented in Table 1. This dataset features profiles with up to 99 vertical levels. We used the 12:00 UTC radiosonde profiles, once it is the closest time to the Landsat 8 crossing time over the study area (~13 UTC). The radiosonde observations were used as the ground truth for evaluating the simulations.

3.2. Reanalysis data

Reanalysis data from the NCEP Climate Forecast System Version 2 (CFSv2) (Saha et al., 2014) 6-hourly product were used as initial and boundary conditions for the simulations. CFSv2 is produced using the NCEP Global Forecasting System (GFS) atmospheric model and the Grid point Statistical Interpolation (GSI) analysis system with three-dimensional variational data assimilation (3D-Var). These data are arranged in grids with a horizontal resolution of 0.5° × 0.5° and in 37 vertical (pressure) levels (1000–1 mbar), 0.205° for surface parameters. The CFSv2 has also been included in the profiles intercomparison, to assess the WRF downscaling performance. The NCEP CFSv2 reanalysis is suitable, providing all variables needed to drive WRF, and frequently employed for WRF simulations (de Lange et al., 2021; Li et al., 2017; Ma et al., 2020; Siegmund et al., 2015). However, it is still underexplored for remote sensing atmospheric correction (Vanhellemont, 2020).

3.3. WRF model configuration and PBL schemes

The numerical simulations were performed using the WRF Model version 4.1.2 with the Advanced Research WRF (ARW) dynamical solver (Skamarock et al., 2019; Wang et al., 2019). The model domains were

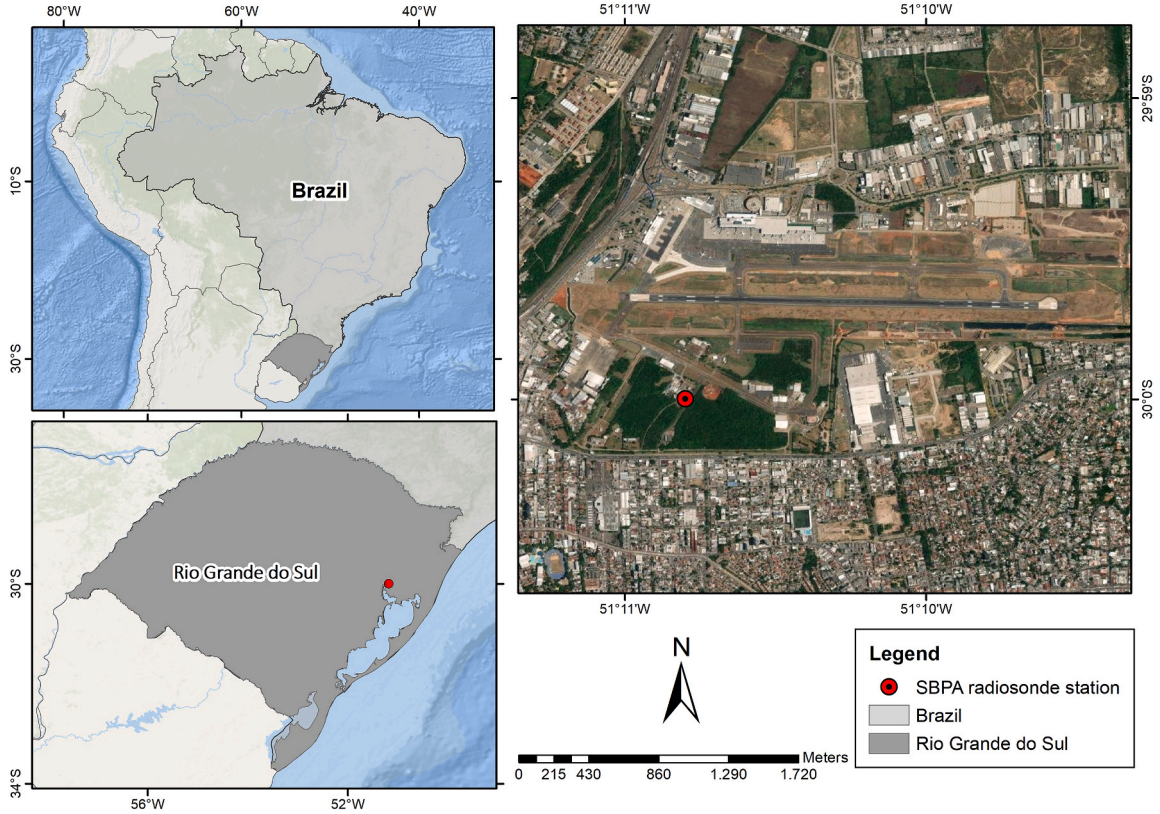

Fig. 1. Location of the study area: Porto Alegre Airport (SBPA) radiosonde station, Southern Brazil.

configured with two nested grids centered at SBPA station, with horizontal resolutions of 12 km (G12) and 3 km (G03) (4:1 parent grid ratio), in one-way mode, and 33 sigma vertical levels with 50 hPa top pressure value. Fig. 2 shows these grids and also an asterisk that indicates where the simulation results were extracted, it refers to the grid point closest to the SBPA station.

The geographical static data such as land use, albedo, reflectance, and topography are introduced to the modeling using the land use categories of the United States Geological Survey (USGS). The time step used for the outermost domain was 72s with a 4:1 parent ratio. The common physics options chosen included: Purdue Lin microphysics parameterization (Chen and Sun, 2002); Betts–Miller–Janjic (BMJ) cumulus scheme (Janjić, 1994); Dudhia shortwave radiation (Dudhia, 1989); Rapid Radiative Transfer Model (RRTM) longwave radiation option (Mlawer et al., 1997); and Unified NOAH Land-Surface Model (LSM) scheme (Tewari et al., 2004). This set of schemes was used while a sensitivity experiment was conducted by changing the PBL and the surface-layer schemes. The Yonsei University (YSU) PBL scheme (Hong et al., 2006) was used tied to the Revised MM5 surface-layer scheme (Jiménez et al., 2012), and Mellor–Yamada–Janjic (MYJ) (Janjić, 1994) combined with Eta Similarity (Janjić, 1994, 1996, 2002; Monin and Obukhov, 1954). Similar choices of parameterization schemes were used in Santos and Nascimento (2016). The WRF model set ups are resumed in Table 2.

The study consisted of 54 runs of 24-h duration for the 27 selected dates in Table 1: a simulation with YSU and another with MJY PBL option for each of the days. Mohan and Sati (2016) reported that smaller time split simulations show significant improvement in the performance. The resulting profiles were extracted at 12:00 UTC, to match with the in situ radiosonde observations. Thus, the first 12 h of the simulation were considered for spin up time. The model output for each grid was stored every half hour.

PBL schemes work to represent unresolved turbulent vertical fluxes' contribution in the boundary layer and through all over the atmospheric column. A closure scheme is required to connect turbulent fluxes of heat, momentum, and moisture with mean quantities (Holt and Raman, 1988; Hu et al., 2010). PBL parameterization can be mainly grouped in local closure or nonlocal closure schemes. In local closure schemes, only the immediately adjacent vertical levels to a given point directly influence variables at that point. Differently, nonlocal closure schemes can use multiple vertical levels to estimate variables at a given point (Cohen et al., 2015; Onwukwe and Jackson, 2020). Cohen et al. (2015) and Jia and Zhang (2020) provide reviews and explanations about the PBL parameterization schemes available for the WRF model. In this work, we tested the most used PBL parameterization scheme of each closure group. Below we present a brief description of the PBL schemes used in the present study.

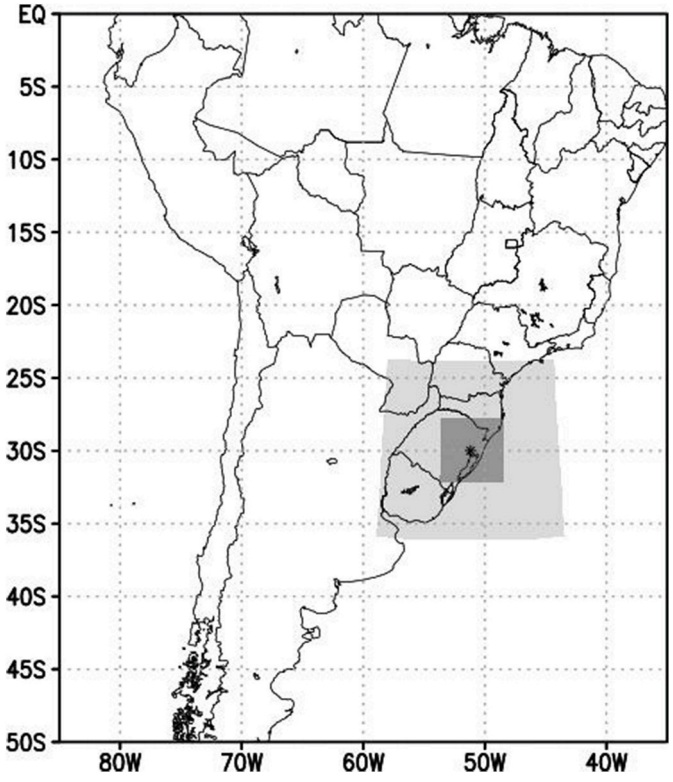

Fig. 2. WRF nested grids used in the study, with horizontal resolutions of 12 km (light gray) and 3 km (dark gray). The asterisk indicates the point where the results were extracted.

Table 2
Overview of WRF model configuration.

WRF Model Configuration	
Version	4.1.2
Dynamical solver	ARW
Initial and boundary conditions	NCEP CFSv2
Map projection	Lambert
Grid size	Domain 1: (119 × 116) x 33
	Domain 2: (169 × 165) x 33
Horizontal resolution	Domain 1: 12 km
	Domain 2: 3 km
Nesting	One-way
Time step	72s
Static geographical data	USGS
Cloud Microphysics	Purdue Lin
PBL	1) YSU
	2) MYJ
Cumulus	BMJ (Domain 1 only)
Shortwave Radiation	Dudhia
Longwave Radiation	RRTM
LSM	Unified NOAH
Surface-layer	1) Revised MM5
	2) Eta Similarity

3.3.1. *Yonsei University (YSU) PBL scheme*

The Yonsei University scheme (Hong et al., 2006) is a first-order, nonlocal eddy-diffusivity (K theory) approach with an explicit treatment of the boundary layer top (Siuta et al., 2017). It comes after modifications from the Medium-Range Forecast Model (MRF) scheme (Hong and Pan, 1996). A parabolic K-profile in an unstable mixed layer with the addition of an explicit term is used to treat the entrainment layer at the PBL top (Banks et al., 2016; Tyagi et al., 2018). It is controlled by the level at that minimum turbulent flux exists (momentum, heat, moisture) (Siuta et al., 2017). The YSU scheme usually works better under unstable/convective conditions and does not perform well in stable conditions, because it underpredicts the vapor mixing ratio due to the high amount of vertical mixing from the large eddies (Chaouch et al., 2017; Shin and Hong, 2011). In day-time convective boundary layers, it can produce conditions that are too warm and dry in the PBL resulting from overmixing (Coniglio et al., 2013). The YSU can be considered the most commonly used PBL scheme (Jia and Zhang, 2020).

3.3.2. *Mellor–Yamada–Janjic (MYJ) PBL scheme*

The Mellor–Yamada–Janjic scheme (Janjić, 1994) is a local mixing one-and-a-half order ("1.5-order") closure scheme, with a prognostic equation for Turbulent Kinetic Energy (TKE). The TKE vertical distribution is regulated by a master mixing length, used in the TKE budget equation. The local closure implies that only small turbulent eddy contributions are considered to the TKE distribution. It does not consider the impact of the nonlocal effects (Jia and Zhang, 2020; Siuta et al., 2017). Traditionally, this scheme produces conditions that are too cool and moist near the ground in day-time convective boundary layers, resulting

from too little mixing (Coniglio et al., 2013), while prevails during stable and very stable conditions. Many researchers choose to utilize this scheme, as it does not have particularly large computational expenses. Thus, MYJ is the most widely used among local schemes (Jia and Zhang, 2020).

3.4. Model evaluation, sensitivity analysis, and statistics

To evaluate the accuracy of the model simulations and the impact of the PBL schemes, we considered vertical profiles of water vapor mixing ratio (q) and potential temperature (θ). A point validation technique was used (Onwukwe and Jackson, 2020). Atmospheric profiles for model grid point corresponding to the ground location of the SBPA station (Fig. 2) were retrieved, at 12 UTC. Namely, the WRF resulting profiles of q and θ for G12 and G03, and with both YSU and MYJ schemes were intercompared against SBPA observational profiles. In addition, profiles retrieved directly from the CFSv2 product were included in the comparative analysis to assess the performance of the WRF in downscaling reanalysis profiles. To analyze the atmospheric stability and the PBL height are beyond the scope of this paper.

Vertical interpolation for a comparison of model output to observations is imperative since the height and pressure of model (sigma) levels can vary both spatially and temporally in the model domain (Cogan, 2017). Therefore, the WRF output data were interpolated from the model to the radiosondes vertical levels. The interpolation was carried out through a weighted linear one (Santos and Nascimento, 2016), Equation (1):

$$D(h) = \left\{ d[h_1] \times \left[1 - \frac{(h - h_1)}{(h_2 - h_1)} \right] \right\} + \left\{ d[h_2] \times \left[1 - \frac{(h_2 - h)}{(h_2 - h_1)} \right] \right\} \quad (1)$$

where $D(h)$ is the interpolated value at the observed level h, and $[h]$ is the simulated value at the two neighboring model levels h_1 and h_2 (Santos and Nascimento, 2016).

The statistical criteria used in this paper are Pearson's correlation coefficient (R), bias (mean error), Mean Absolute Error (MAE), and Root Mean Square Error (RMSE). These statistical metrics are widely used for evaluating the efficiency of models and were selected to reflect a mix of accuracy measurements (Chai and Draxler, 2014; Onwukwe and Jackson, 2020; Sekertekin, 2019; Wilks, 2006; Willmott and Matsuura, 2005). The metrics were computed according to:

$$\mathrm{R} = \frac{\sum_{i=0}^{n}(p_i - \overline{p})(o_i - \overline{o})}{\sqrt{\sum_{i=0}^{n}(p_i - \overline{p})^2}\sqrt{\sum_{i=0}^{n}(o_i - \overline{o})^2}} \quad (2)$$

$$\mathrm{bias} = \frac{1}{n}\sum_{i=1}^{n} p_i - o_i \quad (3)$$

$$\mathrm{MAE} = \frac{1}{n}\sum_{i=1}^{n} |p_i - o_i| \quad (4)$$

$$\mathrm{RMSE} = \sqrt{\frac{1}{n}\sum_{i=1}^{n}(p_i - o_i)^2} \quad (5)$$

where p_i and o_i are pairs of modeled and observed values, respectively, n is the number of pairs, and overbars represent the mean values of the respective terms.

Bias, MAE, and RMSE are in the parameter of interest units and are negatively oriented indices, i.e., values closer to zero are better. Bias is useful in determining if the model is underestimating (bias < 0) or overestimating (bias > 0) the observed variables. MAE is the average of the absolute difference between the simulations and the observations, regardless of model overestimation or underestimation. RMSE represents the deviation between modeled and observed values and is more sensitive to outliers once the errors are squared before summing. While R, the scores range from -1 to 1, and values approaching 1 indicate a strong correlation.

The assessment of the WRF performance and the identification of the most suitable parameterization scheme set are checked per statistical measurements in the lowest 3 km of the atmosphere, to target the PBL depth, and also for the entire model atmospheric profile. The lowest 3 km averaged 17 of the 33 WRF model levels.

4. Results and discussion

4.1. Overall comparison results of the entire model profile

Fig. 3 shows an example of the vertical distribution of q and θ for the case day 9. The performance of the different atmospheric profiles was analyzed by extracting the profiles from the grid point closest to the SBPA station at 12 UTC. The general agreement of q and θ profiles with the model and radiosonde is clearly good. It indicates a consistency of obtained profiles for both CFSv2 reanalysis and all WRF settings (see the supplementary material to check each profile).

Figs. 4 and 5 illustrate the statistical comparison of the studied profiles throughout each case day for q and θ, respectively. Table 3 presents the average metrics of profiles comparison for all evaluated days. The CFSv2 and all WRF profiles showed high correlation coefficient values for the vertical distribution of both q (0.96) and θ (0.99). In general terms, the q profiles showed a mean tendency to overestimate the observations, with CFSv2 showing the highest bias (0.10 g/kg). The q bias of G12 grids (0.04 g/kg) was slightly higher than the G03 ones (0.03 g/kg). In contrast, the WRF configurations tend to underestimate the θ vertical distribution, while CFSv2 reanalysis tends to overestimate it (Fig. 5a). The CFSv2 θ bias was the largest (0.50 K). There was no significant difference between the overall biases of WRF YSU and MYJ. The WRF MYJ had the highest MAE for q (0.44 g/kg), with a small variation in comparison to WRF YSU and CFSv2 (0.43 g/kg). The θ MAE of the WRF profiles was faintly larger (1.60 K against 1.57 K of the CFSv2). Concerning the RMSEs, all the WRF configurations presented the same value, which was slightly worse than the CFSv2 (see Table 3).

Despite RMSE and MAE overall values of the WRF simulations being a bit higher in comparison to NCEP CFSv2, when taking into account each individual case day, the WRF model overcomes the CFSv2 reanalysis in more days than vice versa for water vapor mixing ratio profiles. We have found WRF settings with the best RMSE in 14 of the 27 case days and with the best MAE in 19. Among the WRF configurations, WRF YSU G03 and WRF MYJ G03 showed superior q RMSE and MAE, respectively, in more days (6). On the other hand, the WRF settings overcome the CFSv2 in 13 of the 27 case days, for potential temperature. The WRF YSU G12 setting slightly stands out at this point, with the best θ MAE in 5 case days. In particular, case day 10 was found as the one with the largest discrepancy with observations regarding the vertical evolution of θ: RMSEs around 4.6 K. While in case day 17, e.g., the WRF model notably improved the high θ errors from the NCEP CFSv2 reanalysis.

Statistically, no significant differences are shown between the WRF grids G12 and G03, for both parameterization schemes sets. In some cases, a finer grid even increases errors. This kind of remark has already been mentioned in other studies (Diaz et al., 2020; Hassanli and Rahimzadegan, 2019; Lin et al., 2018; Mohan and Sati, 2016; Pérez-Jordán et al., 2015). It suggests that computation costs can be saved by using a coarse horizontal resolution grid, mean-while efficiently simulate the vertical profile. Lin et al. (2018) simulated water vapor transport with horizontal resolutions of 30, 10, and 2 km. They inferred that a significant difference was found when the model resolution is changed from 30 to 10 km so that a resolution around 10 km represented a good compromise between a spatially detailed simulation and computational time in their study. In this research, in at least 12 of the 27 case days, we have found an improvement in statistical metrics when the model went from 12 km to 3 km horizontal resolution. Pérez-Jordán et al. (2015) improved the resolution from a coarse to 3 km

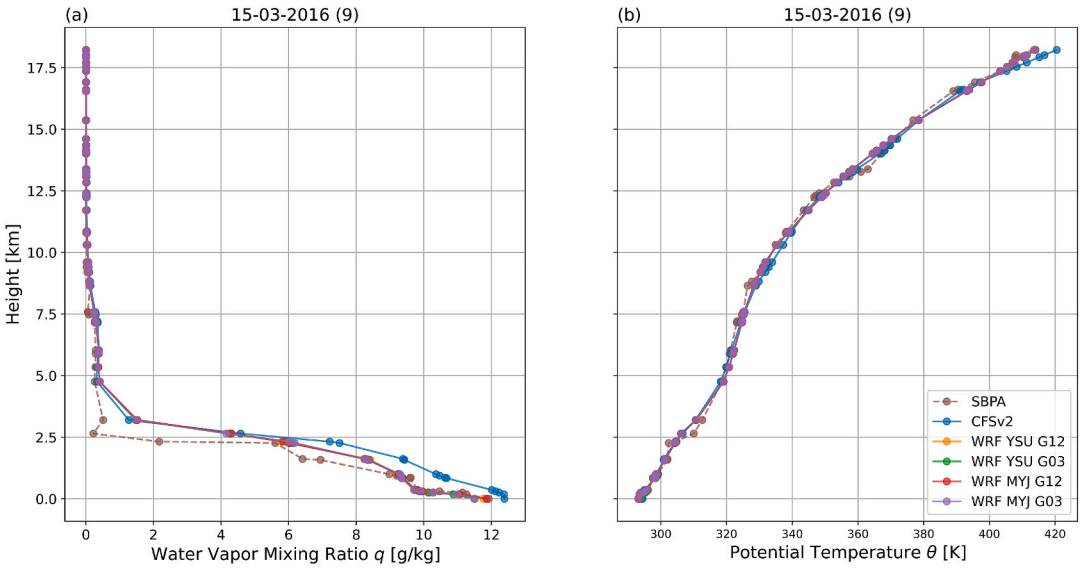

Fig. 3. Vertical profiles of (a) water vapor mixing ratio and (b) potential temperature for the case 9 (15-03-2016).

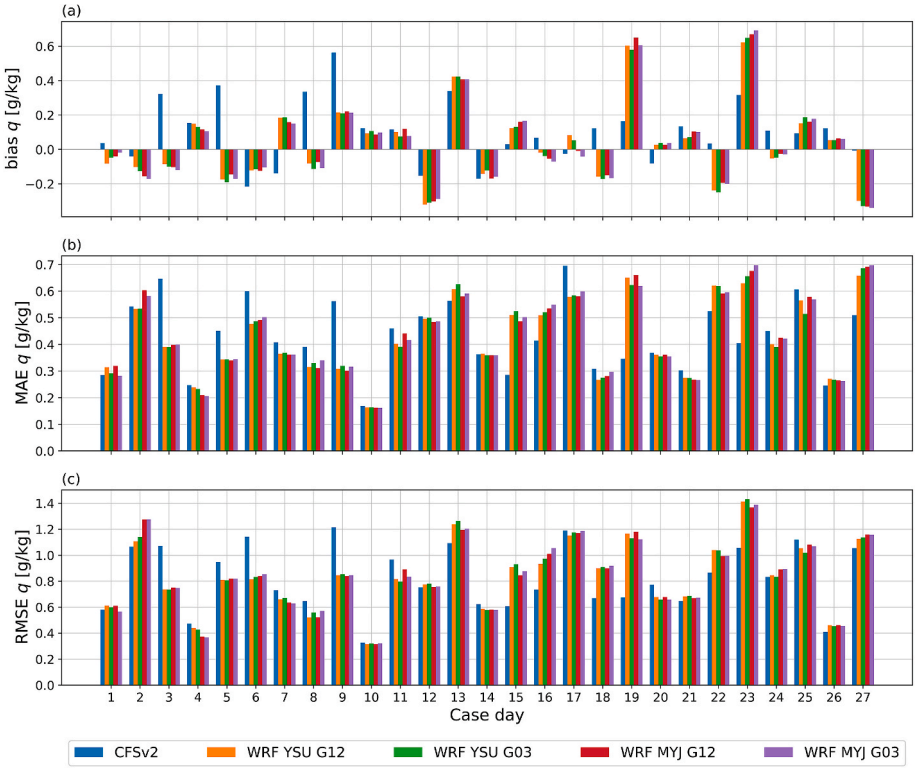

Fig. 4. Statistical metrics: (a) bias, (b) MAE, and (c) RMSE; over the case days for q.

and achieved better results in 8 of 23 water vapor profiles. Thereby, the authors recommended the use of this fine grid spacing for high-resolution operational needs.

The above-mentioned results indicate that no same particular PBL parameterization outperformed the other in all cases analyzed. The best set varied over the case days. We did not observe large differences between the schemes in the vertical distribution of the meteorological variables analyzed. Results in which no single best PBL configuration is identified are common (de Lange et al., 2021). Researchers have already reported this for studies in the United Arab Emirates, the United States, India, Peru, South Africa, and some countries in Europe (Chaouch et al., 2017; Cuchiara et al., 2014; de Lange et al., 2021; Hariprasad et al., 2014; Kioutsioukis et al., 2016; Moya-Álvarez et al., 2020; Tyagi et al., 2018). These findings are in line and corroborate with the conclusions of García-Díez et al. (2013). The authors outlined that the performance of WRF model different settings frequently depends on the seasonal and daily cycles, and therefore on the different atmospheric conditions that prevail on the different seasons and times of the day. de Lange et al. (2021) showed that it is also variable-specific. The next sections assess the dependence of the WRF model and PBL schemes performance on meteorological conditions.

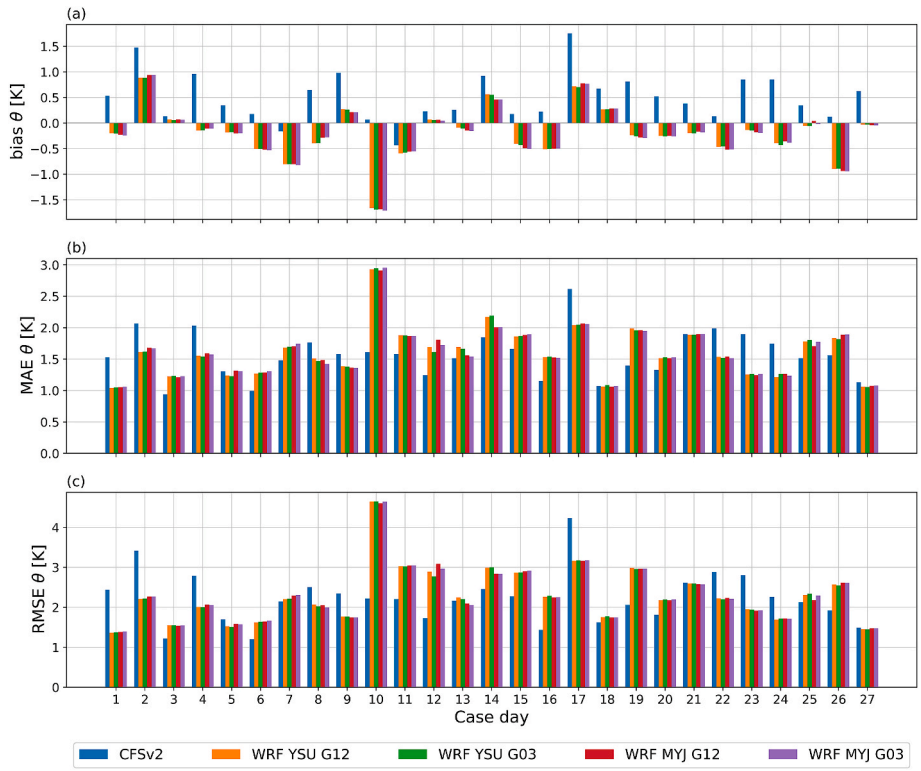

Fig. 5. Statistical metrics: (a) bias, (b) MAE, and (c) RMSE; over the case days for θ.

Table 3
Statistical comparison of all q and θ model profiles against SBPA radiosonde observations.

	CFSv2	WRF YSU G12	WRF YSU G03	WRF MYJ G12	WRF MYJ G03
R q	0.96	0.96	0.96	0.96	0.96
bias q [g/kg]	0.10	0.04	0.03	0.04	0.03
MAE q [g/kg]	0.43	0.43	0.43	0.44	0.44
RMSE q [g/kg]	0.82	0.84	0.84	0.84	0.84
R θ	0.99	0.99	0.99	0.99	0.99
bias θ [K]	0.50	−0.20	−0.20	−0.20	−0.21
MAE θ [K]	1.57	1.61	1.61	1.61	1.61
RMSE θ [K]	2.22	2.30	2.30	2.30	2.30

4.2. Seasonal and meteorological conditions dependence

RMSEs were computed for the profiles evaluated in seasons and specific meteorological conditions. The meteorological conditions of each case day can be found in the supplementary material. Fig. 6 shows the RMSEs of q and θ profiles by the warm (spring and summer) and cold (winter and autumn) seasons, Precipitable Water Vapor (PWV) for the entire observed radiosonde column, and observed wind speed at the SBPA station level.

For both q and θ, the WRF model generates overall better profiles during the warm seasons. Unlike, in cold ones, the model shows larger RMSEs than the profiles retrieved directly from reanalysis. In warm seasons the YSU scheme performed slightly greater, and MYJ showed smaller errors in cold seasons. Regarding the observed water vapor content in the atmosphere, WRF simulated q profiles in better accordance with the radiosondes in PWV below 10 mm and between 20 and 30 mm. In the 20–30 mm range, the YSU scheme showed a bit low RMSE. For θ, the WRF forecasted results were superior in intermediate ranges, while for NCEP CFSv2 were in low and high water vapor content situations. Except for the high PWV range, we found slightly lower θ RMSE values for the MYJ scheme in other PWV contents. In case days when the wind speed was low (at 12 UTC), the WRF was not well at downscaling the reanalysis q profile. Its capability was superior at wind speeds higher than 6 m/s. The WRF generated θ profiles finer than the reanalysis in the 6–12 m/s range. Theoretically, the YSU PBL scheme works better under unstable/convective conditions, while the MYJ PBL scheme prevails under stable atmospheric conditions (Chaouch et al., 2017; Hariprasad et al., 2014; Jia and Zhang, 2020; Kioutsioukis et al., 2016; Shin and Hong, 2011). Our results show that YSU clearly stood out when the wind speeds are higher (Fig. 6c), whereas MYJ overcame a little when it is below 6 m/s. It may suggest an alignment with these previous evaluation studies. A deeper stability analysis exceeds the scope of this paper.

4.3. Vertical distribution of errors

In this section, we assess the vertical distribution of errors in q and θ profiles. For this, we calculate the average RMSE at every 3 m of altitude. Fig. 7 shows q and θ heatmaps with this RMSE vertical distribution. The biggest q errors are located in the first 3 km of the atmosphere. This is clearly related to the water vapor concentration in the atmosphere. Where the amount of water vapor (q) is close to zero, so are the errors in its estimate. This fact contributes to reducing overall errors throughout the entire profile. The NCEP CFSv2 q profiles are in better agreement with the SBPA radiosondes in the first 3 km of the atmosphere, while the WRF ones show better RMSE values in the other layers. Concerning θ profiles, the overall RMSEs are larger in elevated heights (15–18.5 km). In this layer, the WRF errors are lower compared to CFSv2. In the other heights analyzed, the CFSv2 presented better results.

4.4. Lowest 3 km (PBL) comparison results

Due to the PBL importance in our study and the fact that the biggest

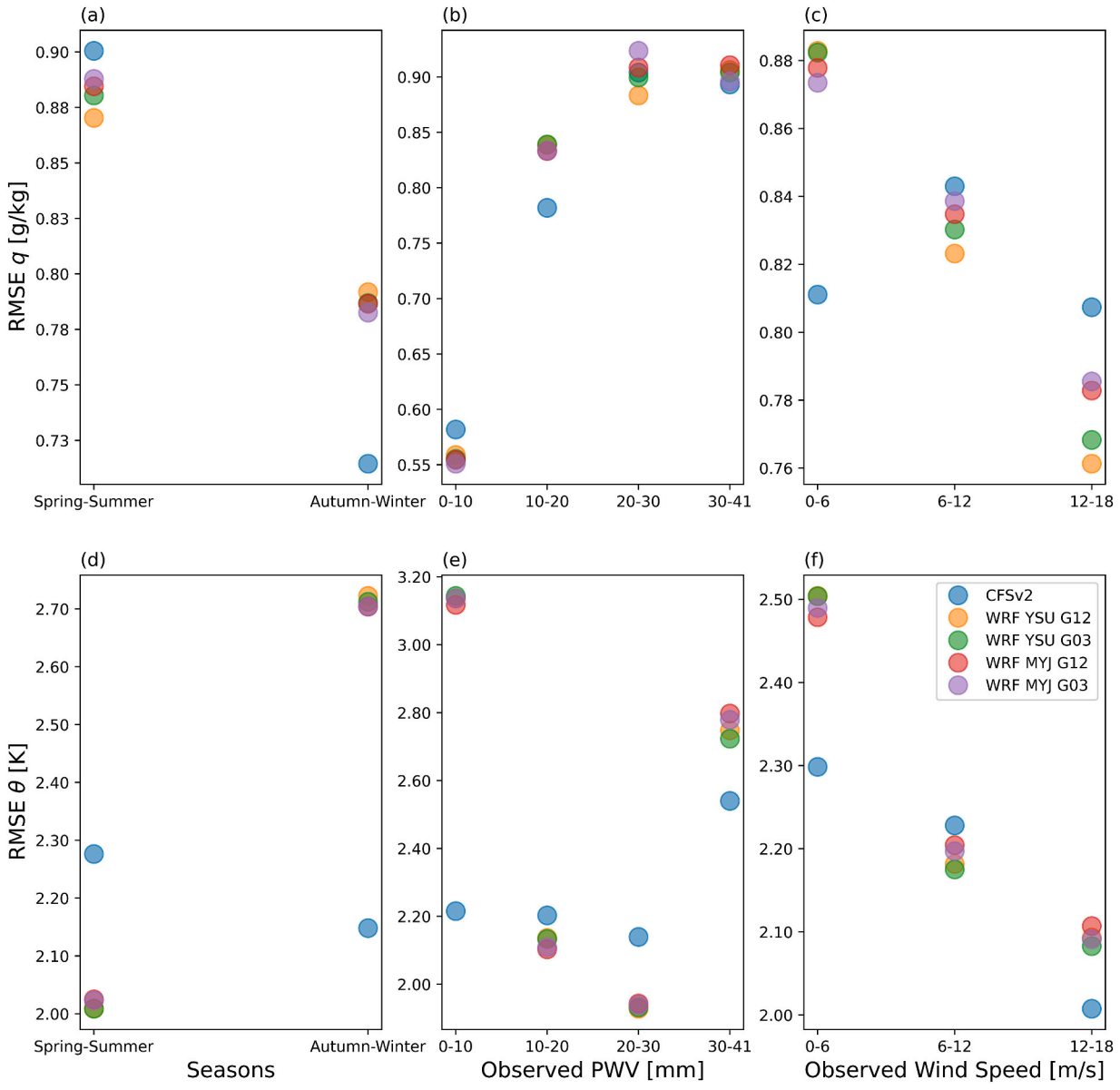

Fig. 6. RMSE of q (a–c) and θ (d–f) profiles by seasons, PWV, and wind speed.

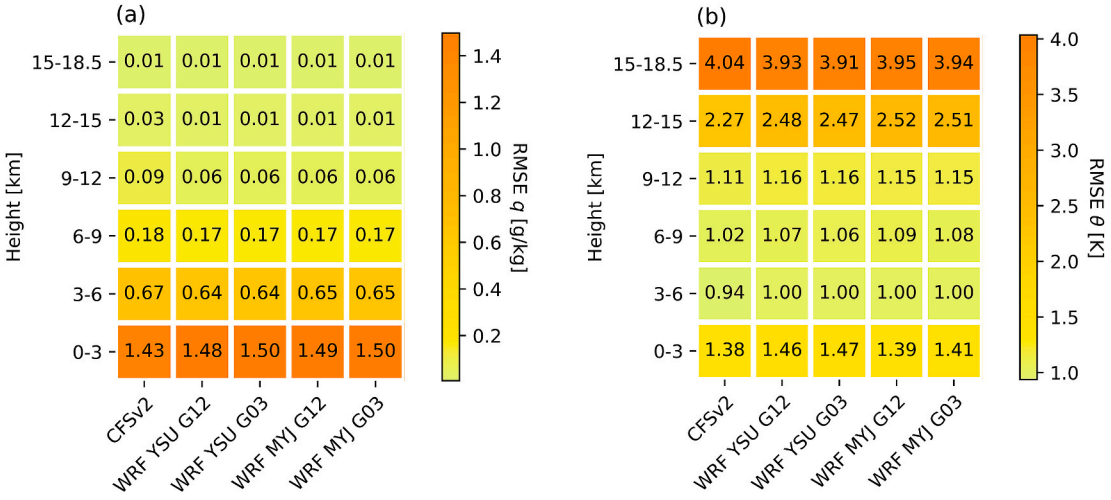

Fig. 7. RMSE vertical distribution by height: (a) q and (b) θ profiles.

errors in the q estimate are in the first kilometers of the atmosphere (as can be seen in the previous section), is essential to pay special attention to the evaluation of the WRF model in this layer. We performed a statistical analysis similar to section 4.1 but considering exclusively the lowest 3 km of the troposphere, aiming to englobe and target the PBL depth. In Fig. 8, examples of 0–3 km vertical profiles are shown (all PBL limited profiles plots are in the supplementary material). Mainly for water vapor mixing ratio, the greater discrepancy of the simulated profiles in the first levels of the atmosphere is visually evident. Table 4 shows the overall metrics and Figs. 9 and 10 the distribution of the statistical metrics along the case days.

The R values are lower than when considering the entire column atmosphere, mainly for q. However, these R values still indicate a strong correlation. The q profiles retrieved from the CFSv2 reanalysis tend to overestimate the reference, while the WRF simulated profiles tend to underestimate it. Li et al. (2019) also recorded that WRF simulations using YSU and MYJ PBL schemes underpredict q near the surface, over the Baltimore-Washington region in the United States. For θ, the tendency is to underestimate the observations for NCEP CFSv2 and WRF settings. Hu et al. (2010) reported that WRF simulations including local and nonlocal PBL schemes under predict temperature profiles near the surface, with the use of the local MYJ producing the largest bias. Santos and Nascimento (2016) related the most negative bias in the lower-tropospheric θ profiles using MYJ, this over the SBPA station. Our results are in agreement with this cold bias in the WRF simulation of the lower 3 km θ profile and with MYJ producing the largest bias. The MYJ scheme is expected to represent a cooler and moister PBL than the YSU scheme, as the turbulent mixing of the first is smaller and it does not consider the impact of nonlocal effects (Jia and Zhang, 2020). Fig. 10a evidence that most case day biases are negative and most of these biases already come from the CFSv2 initial conditions. Prasad et al. (2020) mentioned that the biases of their WRF simulations derive mainly from the biases of the driving reanalysis.

The reanalysis average MAE values are better than the WRF simulated ones. Moreover, G03 domains bring slightly larger MAEs comparing to G12. YSU performs a bit better for q and MYJ for θ. However, in 15 of the 27 case days, one of the WRF simulated profiles overcomes the CFSv2 reanalysis in terms of MAE q, and 16 in terms of MAE θ. The overall MAEs for q are larger than those computed for the entire atmospheric column. And for θ, the overall MAEs are lower than for the entire column. As mentioned above, errors in the estimation of q are higher in the first kilometers of atmosphere, and in the highest model levels for θ.

Table 4
Statistical comparison of all q and θ model profiles against SBPA radiosonde observations in the lowest 3 km of the atmosphere.

	CFSv2	WRF YSU G12	WRF YSU G03	WRF MYJ G12	WRF MYJ G03
R q	0.89	0.87	0.87	0.88	0.88
bias q [g/kg]	0.17	−0.08	−0.09	−0.07	−0.10
MAE q [g/kg]	1.13	1.17	1.18	1.18	1.19
RMSE q [g/kg]	1.43	1.48	1.50	1.49	1.50
R θ	0.97	0.98	0.98	0.98	0.98
bias θ [K]	−0.43	−0.50	−0.53	−0.51	−0.55
MAE θ [K]	1.10	1.19	1.20	1.15	1.17
RMSE θ [K]	1.38	1.46	1.47	1.39	1.41

Regarding the found RMSE values, in 13 (and 16) of the 27 case days, one of the WRF settings overcomes in the simulation of the lowest 3 km profile, for q (for θ). Highlighting that for θ the MJY had better average RMSE results. In contrast, Santos and Nascimento (2016) noticed that the YSU scheme displayed slightly better results in the representation of the potential temperature profile (lowest 3 km) over the same radiosonde station used here. It is important to mention that the authors were studying a specific situation of Low-Level Jet Stream (LLJS) with strong synoptic forcing.

Fig. 11 shows RMSEs of q and θ 0–3 km profiles distributed by seasons, observed PWV, and observed wind speed. For this atmosphere layer, errors are lower in the Autumn-Winter and Spring-Summer seasons, for q and θ respectively. Profiles from NCEP CFSv2 produced average lower q RMSE values in both seasons. Among the WRF configurations, YSU G12 showed slightly better RMSE in warm seasons and MYJ G12 in cold ones. Regarding θ, WRF simulated profiles are in better agreement with observations than CFSv2 in warm seasons, mainly the MYJ PBL scheme. This scheme also has lower RMSEs than the YSU in cold seasons. Though evaluating surface temperature and humidity, de Lange et al. (2021) highlighted that local PBL schemes are preferred during winter periods for a Southern Africa region, which is situated in the subtropic as well. Other authors (García-Díez et al., 2013; Hu et al., 2010) also pointed out that the YSU scheme seems to be an advantageous option for research focused on summer periods, while the MYJ model would be more appropriate for winter periods. The behavior of q

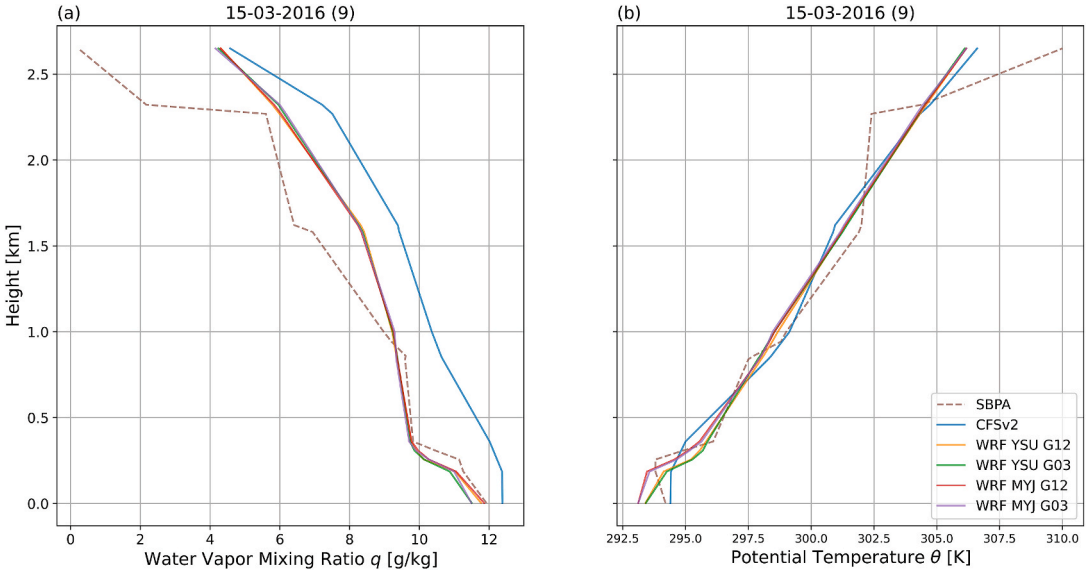

Fig. 8. Lowest 3 km vertical profiles of (a) water vapor mixing ratio and (b) potential temperature for the case 9 (15-03-2016).

Fig. 9. Statistical metrics: (a) bias, (b) MAE, and (c) RMSE; over the case days for q in the lowest 3 km of the atmosphere.

Fig. 10. Statistical metrics: (a) bias, (b) MAE, and (c) RMSE; over the case days for θ in the lowest 3 km of the atmosphere.

in different PWV conditions is quite similar to when the entire column is considered, but with higher RMSE values. In terms of θ, the errors are overall small in moist conditions, with WRF MYJ overcoming when the PWV is higher than 30 mm. YSU performs better at wind speeds greater than 6 m/s and MYJ stood out at speeds below that. As in section 4.2, this may be an indicator of the relationship between the PBL scheme results and the turbulence. Differently, in the lower troposphere, the smallest average RMSEs are produced by CFSv2. WRF has an average

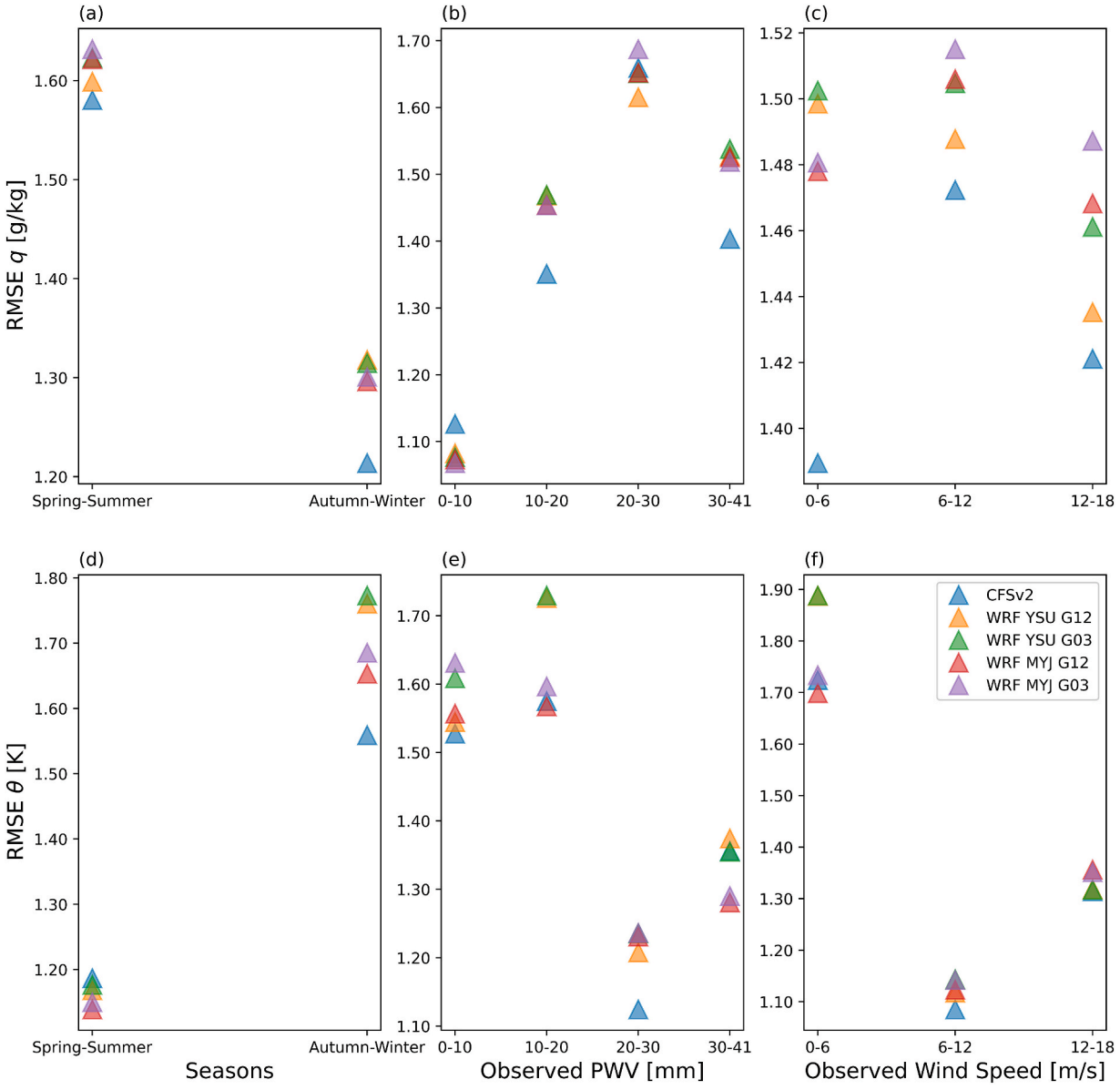

Fig. 11. Lowest 3 km profile RMSE of q (a–c) and θ (d–f) profiles by seasons, PWV, and wind speed.

best RMSE just for θ profiles at the lowest wind speed range with MYJ G12.

5. Conclusions

Assessing downscaled meteorological data is of great importance to diagnose model errors that can propagate to the end application, including the atmospheric correction of optical satellite data. In this paper, the WRF model simulated well the vertical profiles of water vapor mixing ratio and potential temperature. Its resulting profiles yielded high correlation coefficients, very small biases, and relatively low values of RMSE and MAE. However, there is no significant difference in statistical overall results of profiles from WRF varying the horizontal grid resolution from 12 to 3 km, and also with those retrieved directly from NCEP CFSv2 reanalysis. In some cases, increasing the settings resolution even resulted in greater differences compared to the observed profiles. These results indicate that increasing the horizontal resolution did not improve significantly the quality of the simulated atmospheric profile. Therefore, our findings suggest that there is no special need to increase the spatial resolution for applications related to average site atmosphere characterization. Particularly because it adds computational cost without expressive improvement of the simulated profiles. We recommend the use of grid spacing finer than 3 km for specific high-resolution local usages. With the lower impact of the horizontal resolution in mind, we encourage a focus on increasing the vertical resolution in the profile simulations.

The sensitivity analysis of the vertical profile simulation to YSU and MYJ PBL parameterization revealed that no particular scheme stands out in both meteorological variables evaluated for all the case days. These results emphasized that the optimal parameterization scheme set varies with meteorological conditions, season, and variable. Moreover, the overall entire model profile statistical metrics are quite comparable. Thus, choosing one of these PBL schemes over the other may not be pivotal to the depiction of general atmospheric profiles.

The present study advocates that the WRF model is a useful tool in the simulation of water vapor and temperature atmospheric profiles. The application of both WRF and also NCEP CFSv2 profiles in the atmospheric correction of remote sensing images is promising and additional research is currently ongoing with this aim. An assessment using different reanalysis products will also be addressed in a future study.

Finally, note that the presented results are related to a specific site under clear-sky conditions. Supplemental analyses are required to expand and corroborate the conclusions over other environments.

Declaration of competing interest

The authors declare that they have no known competing financial interests or personal relationships that could have appeared to influence the work reported in this paper.

Acknowledgments

The CFSv2 reanalysis data are courtesy of the National Centers for Environmental Prediction (NCEP), available at the Research Data Archive (RDA) – National Center for Atmospheric Research (NCAR). The radiosonde observations were obtained from the University of Wyoming website. This study was financed in part by the Coordenação de Aperfeiçoamento de Pessoal de Nível Superior – Brazil (CAPES), finance code 001, grant number 88882.438973/2019-01. We are also grateful to the anonymous reviewers for their valuable contributions.

Appendix A. Supplementary data

Supplementary data to this article can be found online at https://doi.org/10.1016/j.jastp.2021.105724.

References

Alghamdi, A.S., 2020. Evaluation of four reanalysis datasets against radiosonde over Southwest Asia. Atmosphere 11. https://doi.org/10.3390/ATMOS11040402.

Alvares, C.A., Stape, J.L., Sentelhas, P.C., De Moraes Gonçalves, J.L., Sparovek, G., 2013. Köppen's climate classification map for Brazil. Meteorol. Z. 22, 711–728. https://doi.org/10.1127/0941-2948/2013/0507.

Banks, R.F., Tiana-Alsina, J., Baldasano, J.M., Rocadenbosch, F., Papayannis, A., Solomos, S., Tzanis, C.G., 2016. Sensitivity of boundary-layer variables to PBL schemes in the WRF model based on surface meteorological observations, lidar, and radiosondes during the HygrA-CD campaign. Atmos. Res. 176–177, 185–201. https://doi.org/10.1016/j.atmosres.2016.02.024.

Bao, X., Zhang, F., 2019. How accurate are modern atmospheric reanalyses for the data-sparse Tibetan plateau region? J. Clim. 32, 7153–7172. https://doi.org/10.1175/JCLI-D-18-0705.1.

Bao, X., Zhang, F., 2013. Evaluation of NCEP-CFSR, NCEP-NCAR, ERA-Interim, and ERA-40 reanalysis datasets against independent sounding observations over the Tibetan Plateau. J. Clim. 26, 206–214. https://doi.org/10.1175/JCLI-D-12-00056.1.

Boadh, R., Satyanarayana, A.N.V., Rama Krishna, T.V.B.P.S., Madala, S., 2016. Sensitivity of PBL schemes of the WRF-ARW model in simulating the boundary layer flow parameters for their application to air pollution dispersion modeling over a tropical station. Atmósfera 29, 61–81. https://doi.org/10.20937/ATM.2016.29.01.05.

Chai, T., Draxler, R.R., 2014. Root mean square error (RMSE) or mean absolute error (MAE)? – arguments against avoiding RMSE in the literature. Geosci. Model Dev. (GMD) 7, 1247–1250. https://doi.org/10.5194/gmd-7-1247-2014.

Chan, H.P., Chang, C.P., Dao, P.D., 2018. Geothermal anomaly mapping using Landsat ETM+ data in ilan plain, Northeastern Taiwan. Pure Appl. Geophys. 175, 303–323. https://doi.org/10.1007/s00024-017-1690-z.

Chang, L., Li, Yanxing, Han, Z., Feng, G., Li, Yangdong, Zhang, Y., 2020. Improvement of precipitable water vapour and water vapour mixing ratio profile in atmospheric infrared sounder retrievals: differential linear adjustment model. Int. J. Rem. Sens. 41, 6858–6875. https://doi.org/10.1080/01431161.2020.1750736.

Chaouch, N., Temimi, M., Weston, M., Ghedira, H., 2017. Sensitivity of the meteorological model WRF-ARW to planetary boundary layer schemes during fog conditions in a coastal arid region. Atmos. Res. 187, 106–127. https://doi.org/10.1016/j.atmosres.2016.12.009.

Chen, B., Liu, Z., 2016. Global water vapor variability and trend from the latest 36 year (1979 to 2014) data of ECMWF and NCEP reanalyses, radiosonde, GPS, and microwave satellite. J. Geophys. Res.: Atmospheres 121, 11,442–11,462. https://doi.org/10.1002/2016JD024917.

Chen, G., Iwasaki, T., Qin, H., Sha, W., 2014. Evaluation of the warm-season diurnal variability over East Asia in recent reanalyses JRA-55, ERA-Interim, NCEP CFSR, and NASA MERRA. J. Clim. 27, 5517–5537. https://doi.org/10.1175/JCLI-D-14-00005.1.

Chen, S.-H., Sun, W.-Y., 2002. A one-dimensional time dependent cloud model. Journal of the meteorological society of Japan. Ser. II 80, 99–118. https://doi.org/10.2151/jmsj.80.99.

Cogan, J., 2017. Evaluation of model-generated vertical profiles of meteorological variables: method and initial results. Meteorol. Appl. 24, 219–229. https://doi.org/10.1002/met.1620.

Cohen, A.E., Cavallo, S.M., Coniglio, M.C., Brooks, H.E., 2015. A review of planetary boundary layer parameterization schemes and their sensitivity in simulating southeastern U.S. cold season severe weather environments. Weather Forecast. 30, 591–612. https://doi.org/10.1175/WAF-D-14-00105.1.

Coniglio, M.C., Correia, J., Marsh, P.T., Kong, F., 2013. Verification of convection-allowing WRF model forecasts of the planetary boundary layer using sounding observations. Weather Forecast. 28, 842–862. https://doi.org/10.1175/WAF-D-12-00103.1.

Cuchiara, G.C., Li, X., Carvalho, J., Rappenglück, B., 2014. Intercomparison of planetary boundary layer parameterization and its impacts on surface ozone concentration in the WRF/Chem model for a case study in houston/Texas. Atmos. Environ. 96, 175–185. https://doi.org/10.1016/j.atmosenv.2014.07.013.

de Lange, A., Naidoo, M., Garland, R.M., Dyson, L.L., 2021. Sensitivity of meteorological variables on planetary boundary layer parameterization schemes in the WRF-ARW model. Atmos. Res. 247 https://doi.org/10.1016/j.atmosres.2020.105214.

De Rosa, B., Di Girolamo, P., Summa, D., 2020. Temperature and water vapour measurements in the framework of the network for the detection of atmospheric composition change (NDACC). Atmos. Meas. Techn. 13, 405–427. https://doi.org/10.5194/amt-13-405-2020.

Dee, D.P., Uppala, S.M., Simmons, A.J., Berrisford, P., Poli, P., Kobayashi, S., Andrae, U., Balmaseda, M.A., Balsamo, G., Bauer, P., Bechtold, P., Beljaars, A.C.M.M., van de Berg, L., Bidlot, J., Bormann, N., Delsol, C., Dragani, R., Fuentes, M., Geer, A.J., Haimberger, L., Healy, S.B., Hersbach, H., Hólm, E., v Isaksen, L., Kållberg, P., Köhler, M., Matricardi, M., McNally, A.P., Monge-Sanz, B.M., Morcrette, J.-J., Park, B.-K., Peubey, C., de Rosnay, P., Tavolato, C., Thépaut, J.-N., Vitart, F., 2011. The ERA-Interim reanalysis: configuration and performance of the data assimilation system. Q. J. R. Meteorol. Soc. 137, 553–597. https://doi.org/10.1002/qj.828.

Diaz, L.R., Rolim, S.B.A., Santos, D.C., Käfer, P.S., Rocha, N.S., Alves, R.C.M., 2020. Using the WRF model to refine NCEP CFSv2 reanalysis atmospheric profile: a southern Brazil test case. Braz. J. Geophys. 38 (2), 1–22. https://doi.org/10.22564/rbgf.v38i2.2043.

Divakarla, M.G., Barnet, C.D., Goldberg, M.D., McMillin, L.M., Maddy, E., Wolf, W., Zhou, L., Liu, X., 2006. Validation of Atmospheric Infrared Sounder temperature and water vapor retrievals with matched radiosonde measurements and forecasts. J. Geophys. Res. Atmos. 111, 1–20. https://doi.org/10.1029/2005JD006116.

Dudhia, J., 1989. Numerical study of convection observed during the winter monsoon experiment using a mesoscale two-dimensional model. J. Atmos. Sci. 46, 3077–3107. https://doi.org/10.1175/1520-0469(1989)046<3077:NSOCOD>2.0.CO;2.

Fekih, A., Mohamed, A., 2019. Evaluation of the WRF model on simulating the vertical structure and diurnal cycle of the atmospheric boundary layer over Bordj Badji Mokhtar (southwestern Algeria). J. King Saud Univ. Sci. 31, 602–611. https://doi.org/10.1016/j.jksus.2017.12.004.

Filioglou, M., Nikandrova, A., Niemelä, S., Baars, H., Mielonen, T., Leskinen, A., Brus, D., Romakkaniemi, S., Giannakaki, E., Komppula, M., 2017. Profiling water vapor mixing ratios in Finland by means of a Raman lidar, a satellite and a model. Atmos. Meas. Techn. 10, 4303–4316. https://doi.org/10.5194/amt-10-4303-2017.

García-Díez, M., Fernández, J., Fita, L., Yagüe, C., 2013. Seasonal dependence of WRF model biases and sensitivity to PBL schemes over Europe. Q. J. R. Meteorol. Soc. 139, 501–514. https://doi.org/10.1002/qj.1976.

Garratt, J., 1994. Review: the atmospheric boundary layer. Earth Sci. Rev. 37, 89–134. https://doi.org/10.1016/0012-8252(94)90026-4.

González-Alonso de Linaje, N., Mattar, C., Borvarán, D., 2019. Quantifying the wind energy potential differences using different WRF initial conditions on Mediterranean coast of Chile. Energy 188, 116027. https://doi.org/10.1016/j.energy.2019.116027.

Hariprasad, K.B.R.R., Srinivas, C.V., Singh, A.B., Vijaya Bhaskara Rao, S., Baskaran, R., Venkatraman, B., 2014. Numerical simulation and intercomparison of boundary layer structure with different PBL schemes in WRF using experimental observations at a tropical site. Atmos. Res. 145–146, 27–44. https://doi.org/10.1016/j.atmosres.2014.03.023.

Hassanli, H., Rahimzadegan, M., 2019. Investigating extracted total precipitable water vapor from Weather Research and Forecasting (WRF) model and MODIS measurements. J. Atmos. Sol. Terr. Phys. 193 https://doi.org/10.1016/j.jastp.2019.105060, 105060.

Held, I.M., Soden, B.J., 2000. Water vapor feedback and global warming. Annu. Rev. Energy Environ. 25, 441–475. https://doi.org/10.1146/annurev.energy.25.1.441.

Hersbach, H., Bell, B., Berrisford, P., Hirahara, S., Horányi, A., Muñoz-Sabater, J., Nicolas, J., Peubey, C., Radu, R., Schepers, D., Simmons, A., Soci, C., Abdalla, S., Abellan, X., Balsamo, G., Bechtold, P., Biavati, G., Bidlot, J., Bonavita, M., de Chiara, G., Dahlgren, P., Dee, D., Diamantakis, M., Dragani, R., Flemming, J., Forbes, R., Fuentes, M., Geer, A., Haimberger, L., Healy, S., Hogan, R.J., Hólm, E., Janisková, M., Keeley, S., Laloyaux, P., Lopez, P., Lupu, C., Radnoti, G., de Rosnay, P., Rozum, I., Vamborg, F., Villaume, S., Thépaut, J.N., 2020. The ERA5 global reanalysis. Quar. J. Royal Meteorol. Soc. 1–51. https://doi.org/10.1002/qj.3803.

Holt, T., Raman, S., 1988. A review and comparative evaluation of multilevel boundary layer parameterizations for first-order and turbulent kinetic energy closure schemes. Rev. Geophys. 26, 761–780. https://doi.org/10.1029/RG026i004p00761.

Hong, S.-Y., Noh, Y., Dudhia, J., 2006. A new vertical diffusion package with an explicit treatment of entrainment processes. Mon. Weather Rev. 134, 2318–2341. https://doi.org/10.1175/MWR3199.1.

Hong, S.-Y., Pan, H.-L., 1996. Nonlocal boundary layer vertical diffusion in a medium-range forecast model. Mon. Weather Rev. 124, 2322–2339. https://doi.org/10.1175/1520-0493(1996)124<2322:NBLVDI>2.0.CO;2.

Hu, X.-M., Nielsen-Gammon, J.W., Zhang, F., 2010. Evaluation of three planetary boundary layer schemes in the WRF model. J. Appl. Meteorol. Climatol. 49, 1831–1844. https://doi.org/10.1175/2010JAMC2432.1.

Janjić, Z.I., 2002. Nonsingular implementation of the mellor-yamada level 2.5 scheme in the NCEP meso model. NCEP Office Note.
Janjić, Z.I., 1996. The surface layer in the NCEP ETA model. In: Eleventh Conference on Numerical Weather Prediction. Amer. Meteor. Soc., pp. 354–355. Norfolk, VA.
Janjić, Z.I., 1994. The step-mountain Eta coordinate model: further developments of the convection, viscous sublayer, and turbulence closure schemes. Mon. Weather Rev. 122, 927–945. https://doi.org/10.1175/1520-0493(1994)122<0927:TSMECM>2.0.CO;2.
Jia, W., Zhang, X., 2020. The role of the planetary boundary layer parameterization schemes on the meteorological and aerosol pollution simulations: a review. Atmos. Res. 239 https://doi.org/10.1016/j.atmosres.2020.104890, 104890.
Jiang, J., Zhou, T., Zhang, W., 2019. Evaluation of satellite and reanalysis precipitable water vapor data sets against radiosonde observations in central Asia. Earth Space Sci. 6, 1129–1148. https://doi.org/10.1029/2019EA000654.
Jiménez, P.A., Dudhia, J., González-Rouco, J.F., Navarro, J., Montávez, J.P., García-Bustamante, E., 2012. A revised scheme for the WRF surface layer formulation. Mon. Weather Rev. 140, 898–918. https://doi.org/10.1175/MWR-D-11-00056.1.
Jiménez-Muñoz, J.C., Sobrino, J.A., Mattar, C., Franch, B., 2010. Atmospheric correction of optical imagery from MODIS and Reanalysis atmospheric products. Rem. Sens. Environ. 114, 2195–2210. https://doi.org/10.1016/j.rse.2010.04.022.
Khanal, S., Fulton, J., Shearer, S., 2017. An overview of current and potential applications of thermal remote sensing in precision agriculture. Comput. Electron. Agric. 139, 22–32. https://doi.org/10.1016/j.compag.2017.05.001.
Kioutsioukis, I., de Meij, A., Jakobs, H., Katragkou, E., Vinuesa, J., Kazantzidis, A., 2016. High resolution WRF ensemble forecasting for irrigation: multi-variable evaluation. Atmos. Res. 167, 156–174. https://doi.org/10.1016/j.atmosres.2015.07.015.
Knievel, J.C., Bryan, G.H., Hacker, J.P., 2007. Explicit numerical diffusion in the WRF model. Mon. Weather Rev. 135, 3808–3824. https://doi.org/10.1175/2007MWR2100.1.
Lemus-Canovas, M., Martin-Vide, J., Moreno-Garcia, M.C., Lopez-Bustins, J.A., 2020. Estimating Barcelona's metropolitan daytime hot and cold poles using Landsat-8 Land Surface Temperature. Sci. Total Environ. 699 https://doi.org/10.1016/j.scitotenv.2019.134307, 134307.
Li, Y., Barth, M.C., Steiner, A.L., 2019. Comparing turbulent mixing of atmospheric oxidants across model scales. Atmos. Environ. 199, 88–101. https://doi.org/10.1016/j.atmosenv.2018.11.004.
Li, Y., Lu, G., Wu, Z., He, H., He, J., 2017. High-resolution dynamical downscaling of seasonal precipitation forecasts for the hanjiang basin in China using the weather research and forecasting model. J. Appl. Meteorol. Climatol. 56 https://doi.org/10.1175/JAMC-D-16-0268.1.
Li, Z., Muller, J.P., Cross, P., 2003. Comparison of precipitable water vapor derived from radiosonde, GPS, and Moderate-Resolution Imaging Spectroradiometer measurements. J. Geophys. Res. Atmos. 108 https://doi.org/10.1029/2003JD003372.
Li, Z.-L., Tang, B.-H., Wu, H., Ren, H., Yan, G., Wan, Z., Trigo, I.F., Sobrino, J.A., 2013. Satellite-derived land surface temperature: current status and perspectives. Rem. Sens. Environ. 131, 14–37. https://doi.org/10.1016/j.rse.2012.12.008.
Lin, C., Chen, D., Yang, K., Ou, T., 2018. Impact of model resolution on simulating the water vapor transport through the central Himalayas: implication for models' wet bias over the Tibetan Plateau. Clim. Dynam. 51, 3195–3207. https://doi.org/10.1007/s00382-018-4074-x.
Ma, S., Zhou, L., Li, F., Zhu, J., 2020. Evaluation of WRF land surface schemes in land-atmosphere exchange simulations over grassland in Southeast Tibet. Atmos. Res. 234 https://doi.org/10.1016/j.atmosres.2019.104739.
Madala, S., Satyanarayana, A.N.V., Rao, T.N., 2014. Performance evaluation of PBL and cumulus parameterization schemes of WRF ARW model in simulating severe thunderstorm events over Gadanki MST radar facility - case study. Atmos. Res. 139, 1–17. https://doi.org/10.1016/j.atmosres.2013.12.017.
Maffei, C., Alfieri, S.M., Menenti, M., 2018. Relating spatiotemporal patterns of forest fires burned area and duration to diurnal land surface temperature anomalies. Remote Sensing 10. https://doi.org/10.3390/rs10111777.
Matzenauer, R., Radin, B., Almeida, I.R. de, 2011. Atlas Climático Do Rio Grande Do Sul. Porto Alegre.
Meng, X., Cheng, J., 2018. Evaluating eight global reanalysis products for atmospheric correction of thermal infrared sensor—application to Landsat 8 TIRS10 data. Rem. Sens. 10 (474) https://doi.org/10.3390/rs10030474.
Mlawer, E.J., Taubman, S.J., Brown, P.D., Iacono, M.J., Clough, S.A., 1997. Radiative transfer for inhomogeneous atmospheres: RRTM, a validated correlated-k model for the longwave. J. Geophys. Res.: Atmospheres 102, 16663–16682. https://doi.org/10.1029/97JD00237.
Mohan, M., Sati, A.P., 2016. WRF model performance analysis for a suite of simulation design. Atmos. Res. 169, 280–291. https://doi.org/10.1016/j.atmosres.2015.10.013.
Monin, A.S., Obukhov, A.M., 1954. Basic laws of turbulent mixing in the surface layer of the atmosphere. Contrib. Geophys. Inst. Acad. Sci. USSR 24, 163–187.
Mooney, P.A., Mulligan, F.J., Fealy, R., 2011. Comparison of ERA-40, ERA-Interim and NCEP/NCAR reanalysis data with observed surface air temperatures over Ireland. Int. J. Climatol. 31, 545–557. https://doi.org/10.1002/joc.2098.
Moya-Álvarez, A.S., Estevan, R., Kumar, S., Flores Rojas, J.L., Ticse, J.J., Martínez-Castro, D., Silva, Y., 2020. Influence of PBL parameterization schemes in WRF_ARW model on short - range precipitation's forecasts in the complex orography of Peruvian Central Andes. Atmos. Res. 233 https://doi.org/10.1016/j.atmosres.2019.104708, 104708.
Naakka, T., Nygård, T., Tjernström, M., Vihma, T., Pirazzini, R., Brooks, I.M., 2019. The impact of radiosounding observations on numerical weather prediction analyses in the arctic. Geophys. Res. Lett. 46, 8527–8535. https://doi.org/10.1029/2019GL083332.
Onwukwe, C., Jackson, P.L., 2020. Meteorological downscaling with wrf model, version 4.0, and comparative evaluation of planetary boundary layer schemes over a complex coastal airshed. J. Appl. Meteorol. Climatol. 59, 1295–1319. https://doi.org/10.1175/JAMC-D-19-0212.1.
Pérez-Jordán, G., Castro-Almazán, J.A., Muñoz-Tuñón, C., Codina, B., Vernin, J., 2015. Forecasting the precipitable water vapour content: validation for astronomical observatories using radiosoundings. Mon. Not. Roy. Astron. Soc. 452, 1992–2003. https://doi.org/10.1093/mnras/stv1394.
Powers, J.G., Klemp, J.B., Skamarock, W.C., Davis, C.A., Dudhia, J., Gill, D.O., Coen, J.L., Gochis, D.J., Ahmadov, R., Peckham, S.E., Grell, G.A., Michalakes, J., Trahan, S., Benjamin, S.G., Alexander, C.R., Dimego, G.J., Wang, W., Schwartz, C.S., Romine, G. S., Liu, Z., Snyder, C., Chen, F., Barlage, M.J., Yu, W., Duda, M.G., 2017. The weather research and forecasting model: overview, system efforts, and future directions. Bull. Am. Meteorol. Soc. 98, 1717–1737. https://doi.org/10.1175/BAMS-D-15-00308.1.
Prasad, A.A., Sherwood, S.C., Brogniez, H., 2020. Using Megha-Tropiques satellite data to constrain humidity in regional convective simulations: a northern Australian test case. Q. J. R. Meteorol. Soc. 1–21. https://doi.org/10.1002/qj.3816.
Raja, M.K.R.V., Gutman, S.I., Yoe, J.G., McMillin, L.M., Zhao, J., 2008. The validation of AIRS retrievals of integrated precipitable water vapor using measurements from a network of ground-based GPS receivers over contiguous United States. J. Atmos. Ocean. Technol. 25, 416–428. https://doi.org/10.1175/2007JTECHA889.1.
Rao, V.K., Mitra, A.K., Singh, K.K., Bharathi, G., Ramakrishnna, S.S.V.S., Sateesh, M., Navria, K., Chauhan, A., Singh, V., Ramesh, K.J., 2020. Validating INSAT-3D atmospheric temperature retrievals over India using radiosonde measurements and other satellite observations. Meteorol. Atmos. Phys. 132, 583–601. https://doi.org/10.1007/s00703-019-00710-8.
Rocha, N.S., da Käfer, P.S., Skokovic, D., Veeck, G., Diaz, L.R., Kaiser, E.A., Carvalho, C. M., Cruz, R.C., Sobrino, J.A., Roberti, D.R., Rolim, S.B.A., 2020. The influence of land surface temperature in evapotranspiration estimated by the S-sebi model. Atmosphere 11, 1059. https://doi.org/10.3390/atmos11101059.
Rosas, J., Houborg, R., McCabe, M.F., 2017. Sensitivity of Landsat 8 surface temperature estimates to atmospheric profile data: a study using MODTRAN in dryland irrigated systems. Rem. Sens. 9 (988) https://doi.org/10.3390/rs9100988.
Ruiz, J.J., Saulo, C., Nogués-Paegle, J., 2010. WRF model sensitivity to choice of parameterization over South America: validation against surface variables. Mon. Weather Rev. 138, 3342–3355. https://doi.org/10.1175/2010MWR3358.1.
Saha, S., Moorthi, S., Wu, X., Wang, J., Nadiga, S., Tripp, P., Behringer, D., Hou, Y.-T., Chuang, H., Iredell, M., Ek, M., Meng, J., Yang, R., Mendez, M.P., van den Dool, H., Zhang, Q., Wang, W., Chen, M., Becker, E., 2014. The NCEP climate forecast system version 2. J. Clim. 27, 2185–2208. https://doi.org/10.1175/JCLI-D-12-00823.1.
Santos, D.C., Nascimento, E.D.L., 2016. Numerical simulations of the South American low level Jet in two episodes of MCSs: sensitivity to PBL and convective parameterization schemes. Adv. Meteorol. 2016, 1–18. https://doi.org/10.1155/2016/2812978.
Schafer, R., Avery, S.K., Gage, K.S., 2003. A comparison of VHF wind profiler observations and the NCEP-NCAR reanalysis over the tropical Pacific. J. Appl. Meteorol. 42, 873–889. https://doi.org/10.1175/1520-0450(2003)042<0873:ACOVWP>2.0.CO;2.
Sekertekin, A., 2019. Validation of physical radiative transfer equation-based land surface temperature using Landsat 8 satellite imagery and SURFRAD in-situ measurements. J. Atmos. Sol. Terr. Phys. 196 https://doi.org/10.1016/j.jastp.2019.105161, 105161.
Sekertekin, A., Inyurt, S., Yaprak, S., 2020. Pre-seismic ionospheric anomalies and spatio-temporal analyses of MODIS Land surface temperature and aerosols associated with Sep, 24 2013 Pakistan Earthquake. J. Atmos. Sol. Terr. Phys. 200 https://doi.org/10.1016/j.jastp.2020.105218, 105218.
Sherwood, S.C., Roca, R., Weckwerth, T.M., Andronova, N.G., 2010. Tropospheric water vapor, convection, and climate. Rev. Geophys. 48, RG2001. https://doi.org/10.1029/2009RG000301.
Shin, H.H., Hong, S.Y., 2011. Intercomparison of planetary boundary-layer parametrizations in the WRF model for a single day from CASES-99. Boundary-Layer Meteorol. 139, 261–281. https://doi.org/10.1007/s10546-010-9583-z.
Siegmund, J., Bliefernicht, J., Laux, P., Kunstmann, H., 2015. Toward a seasonal precipitation prediction system for West Africa: performance of CFSv2 and high-resolution dynamical downscaling. Journal of Geophysical Research. Atmospheres 120. https://doi.org/10.1002/2014JD022692.
Siuta, D., West, G., Stull, R., 2017. WRF hub-height wind forecast sensitivity to PBL scheme, grid length, and initial condition choice in complex terrain. Weather Forecast. 32, 493–509. https://doi.org/10.1175/WAF-D-16-0120.1.
Skamarock, W.C., Klemp, J.B., Dudhia, J., Gill, D.O., Zhiquan, L., Berner, J., Wang, W., Powers, J.G., Duda, M.G., Barker, D.M., Huang, X.-Y., 2019. A description of the advanced research WRF model version 4. In: NCAR Technical Note NCAR/TN-475+STR. https://doi.org/10.5065/1dfh-6p97. Boulder, Colorado.
Sobrino, J.A., Coll, C., Caselles, V., 1991. Atmospheric correction for land surface temperature using NOAA-11 AVHRR channels 4 and 5. Rem. Sens. Environ. 38, 19–34. https://doi.org/10.1016/0034-4257(91)90069-I.
Sobrino, J.A., Jiménez-Muñoz, J.C., Mattar, C., Sòria, G., 2015. Evaluation of Terra/MODIS atmospheric profiles product (MOD07) over the Iberian Peninsula: a comparison with radiosonde stations. Int. J. Digit. Earth 8, 771–783. https://doi.org/10.1080/17538947.2014.936973.
Stensrud, D.J., 2007. Parameterization Schemes, Parameterization Schemes: Keys to Understanding Numerical Weather Prediction Models. Cambridge University Press, Cambridge. https://doi.org/10.1017/CBO9780511812590.

Stull, R., 2017. Practical Meteorology: an Algebra-Based Survey of Atmospheric Science, 1.02b. University of British Columbia, Vancouver.

Tardy, B., Rivalland, V., Huc, M., Hagolle, O., Marcq, S., Boulet, G., 2016. A software tool for atmospheric correction and surface temperature estimation of Landsat infrared thermal data. Rem. Sens. 8 (696) https://doi.org/10.3390/rs8090696.

Tewari, M., Chen, F., Wang, W., Dudhia, J., LeMone, M.A., Mitchell, K., Ek, M., Gayno, G., Wegiel, J., Cuenca, R.H., 2004. Implementation and verification of the unified noah land surface model in the WRF model. Bull. Am. Meteorol. Soc. 2165–2170. https://doi.org/10.1007/s11269-013-0452-7.

Thorne, P.W., Parker, D.E., Christy, J.R., Mears, C.A., 2005. Uncertainties in climate trends: lessons from upper-air temperature records. Bull. Am. Meteorol. Soc. 86, 1437–1442. https://doi.org/10.1175/BAMS-86-10-1437.

Tonooka, H., 2001. An atmospheric correction algorithm for thermal infrared multispectral data over land-a water-vapor scaling method. IEEE Trans. Geosci. Rem. Sens. 39, 682–692. https://doi.org/10.1109/36.911125.

Turner, D.D., Feltz, W.F., Ferrare, R.A., 2000. Continuous water vapor profiles from operational ground-based active and passive remote sensors. Bull. Am. Meteorol. Soc. 81, 1301–1317. https://doi.org/10.1175/1520-0477(2000)081<1301:CWBPFO>2.3.CO;2.

Tyagi, B., Magliulo, V., Finardi, S., Gasbarra, D., Carlucci, P., Toscano, P., Zaldei, A., Riccio, A., Calori, G., D'Allura, A., Gioli, B., 2018. Performance analysis of planetary boundary layer parameterization schemes in WRF modeling set up over Southern Italy. Atmosphere 9, 1–22. https://doi.org/10.3390/atmos9070272.

Vanhellemont, Q., 2020. Automated water surface temperature retrieval from Landsat 8/TIRS. Rem. Sens. Environ. 237 https://doi.org/10.1016/j.rse.2019.111518, 111518.

Wang, A., Zeng, X., 2012. Evaluation of multireanalysis products with in situ observations over the Tibetan Plateau. J. Geophys. Res. Atmos. 117, 1–12. https://doi.org/10.1029/2011JD016553.

Wang, W., Bruyere, C., Michael, D., Duhia, J., Dave, G., Kavulich, M., Werner, K., Chen, M., Hui-Chuan, L., Michalakes, J., Rizvi, S., 2019. Advanced research WRF (ARW) version 4. Model. Syst. Useŕs Guide.

Wee, T.K., Kuo, Y.H., Lee, D., kyou Liu, Z., Wang, W., Chen, S.Y., 2012. Two overlooked biases of the advanced research wrf (arw) model in geopotential height and temperature. Mon. Weather Rev. 140, 3907–3918. https://doi.org/10.1175/MWR-D-12-00045.1.

Wilks, D.S., 2006. Statistical methods in the atmospheric sciences. In: International Geophysics Series, second ed. Elsevier Inc., Burlington.

Willmott, C.J., Matsuura, K., 2005. Advantages of the mean absolute error (MAE) over the root mean square error (RMSE) in assessing average model performance. Clim. Res. 30, 79–82. https://doi.org/10.3354/cr030079.

Xie, B., Fung, J.C.H., Chan, A., Lau, A., 2012. Evaluation of nonlocal and local planetary boundary layer schemes in the WRF model. J. Geophys. Res. Atmos. 117, 1–26. https://doi.org/10.1029/2011JD017080.

Xie, B., Hunt, J.C.R., Carruthers, D.J., Fung, J.C.H., Barlow, J.F., 2013. Structure of the planetary boundary layer over Southeast England: modeling and measurements. J. Geophys. Res. Atmos. 118, 7799–7818. https://doi.org/10.1002/jgrd.50621.

Xu, G., Xi, B., Zhang, W., Cui, C., Dong, X., Liu, Y., Yan, G., 2015. Comparison of atmospheric profiles between microwave radiometer retrievals and radiosonde soundings. J. Geophys. Res. 120, 10313–10323. https://doi.org/10.1002/2015JD023438.

Yang, J., Duan, S.B., Zhang, X., Wu, P., Huang, C., Leng, P., Gao, M., 2020. Evaluation of seven atmospheric profiles from reanalysis and satellite-derived products: implication for single-channel land surface temperature retrieval. Rem. Sens. 12 https://doi.org/10.3390/rs12050791.

Zhao, Y., Yan, H., Wu, P., Zhou, D., 2020. Linear correction method for improved atmospheric vertical profile retrieval based on ground-based microwave radiometer. Atmos. Res. 232, 104678. https://doi.org/10.1016/j.atmosres.2019.104678.

Supplementary material

1. Vertical profiles analyzed in the study

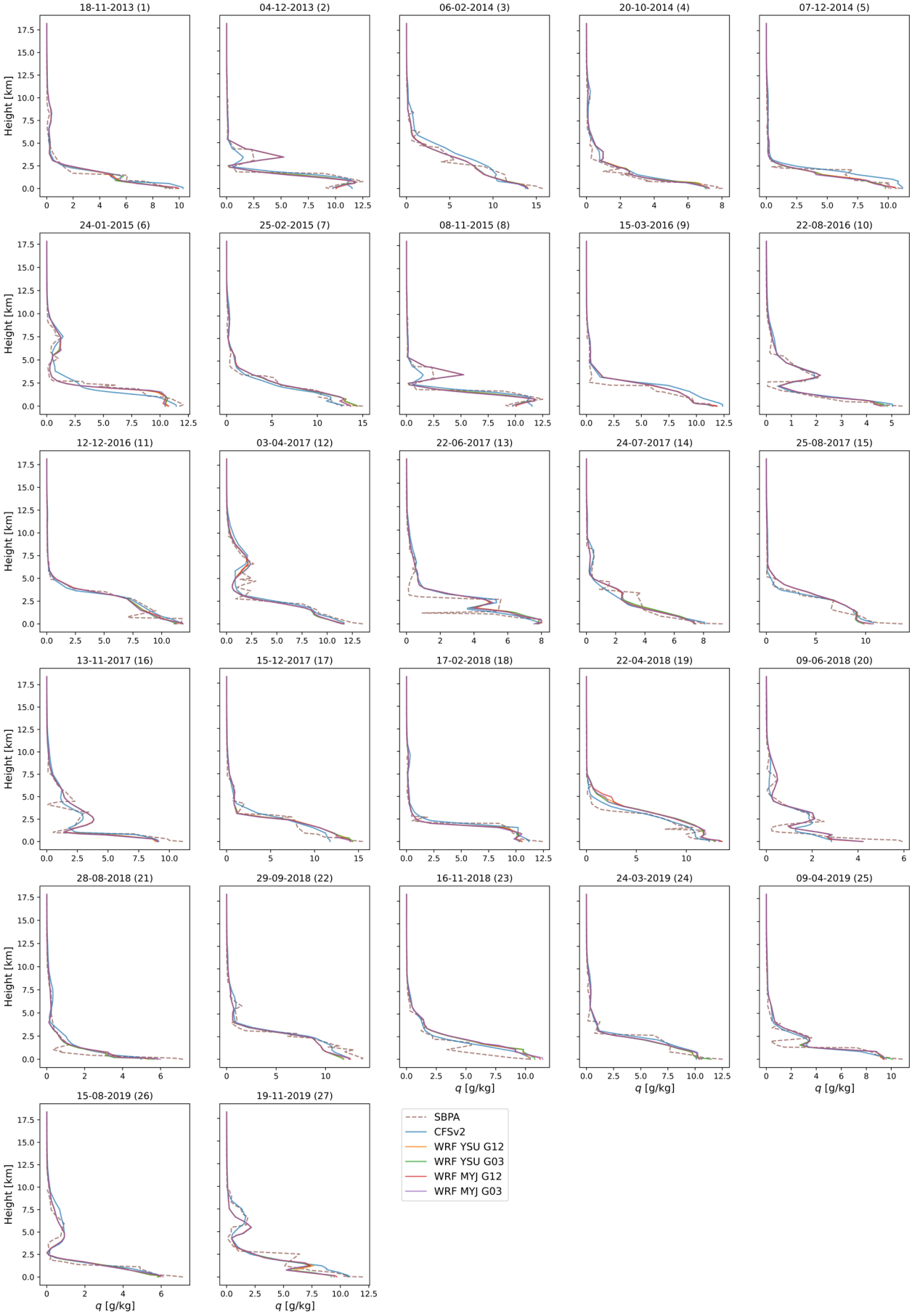

Fig. S1. Vertical profiles of water vapor mixing ratio (q) for each case day.

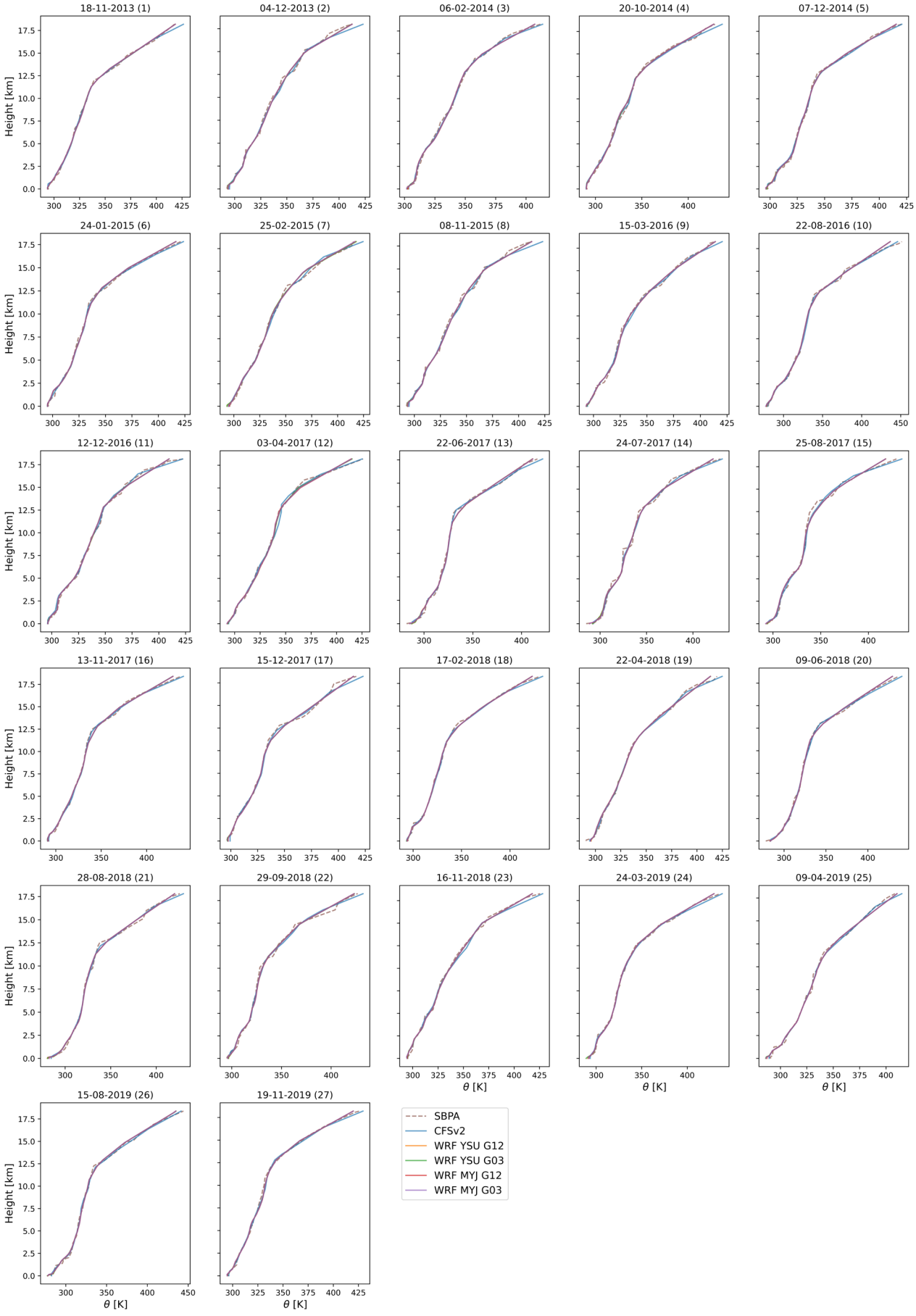

Fig. S2. Vertical profiles of potential temperature (θ) for each case day.

2. Vertical profiles limited to the lowest 3 km of the atmosphere

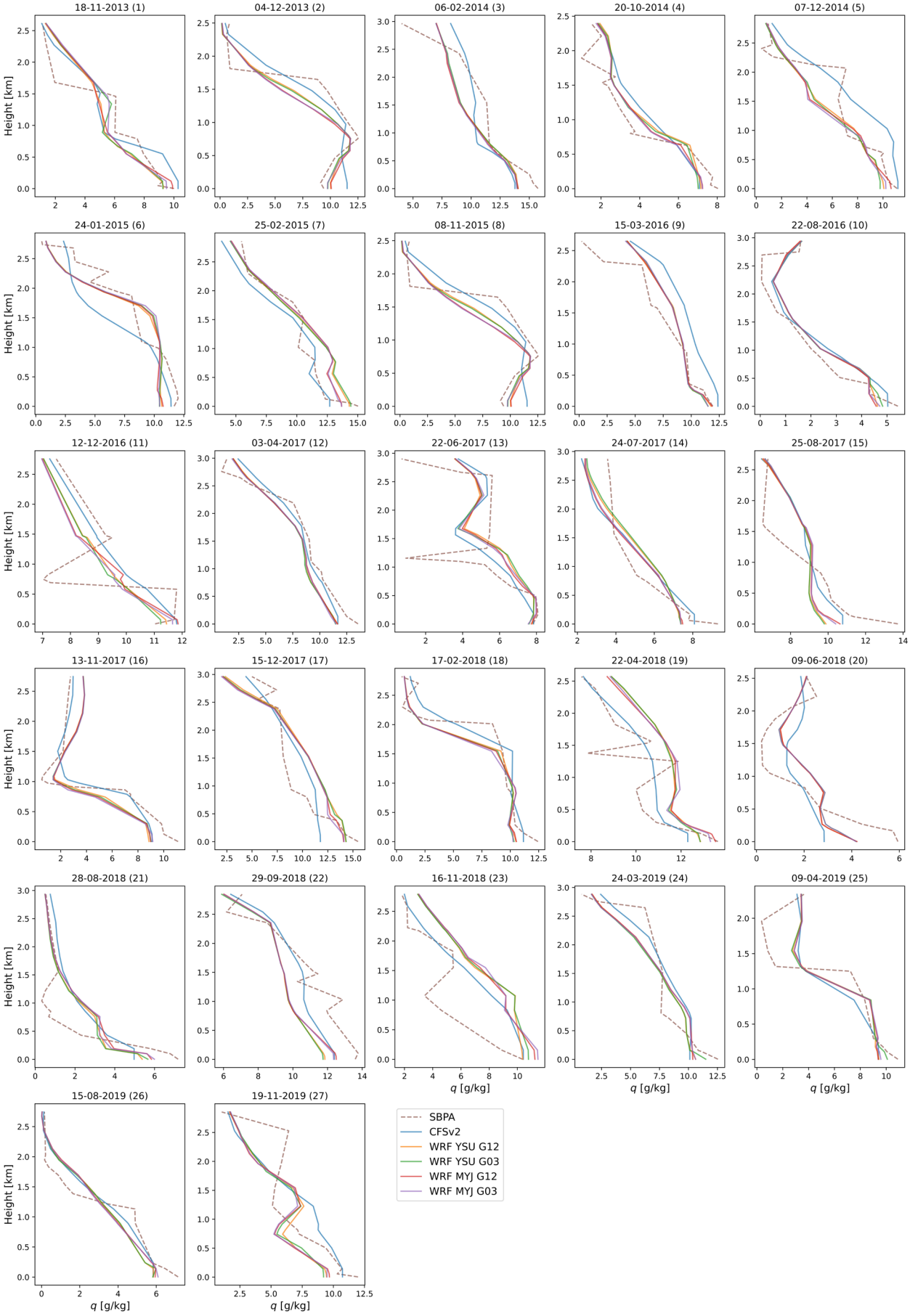

Fig. S3. Lowest 3 km vertical profiles of water vapor mixing ratio (q) for each case day.

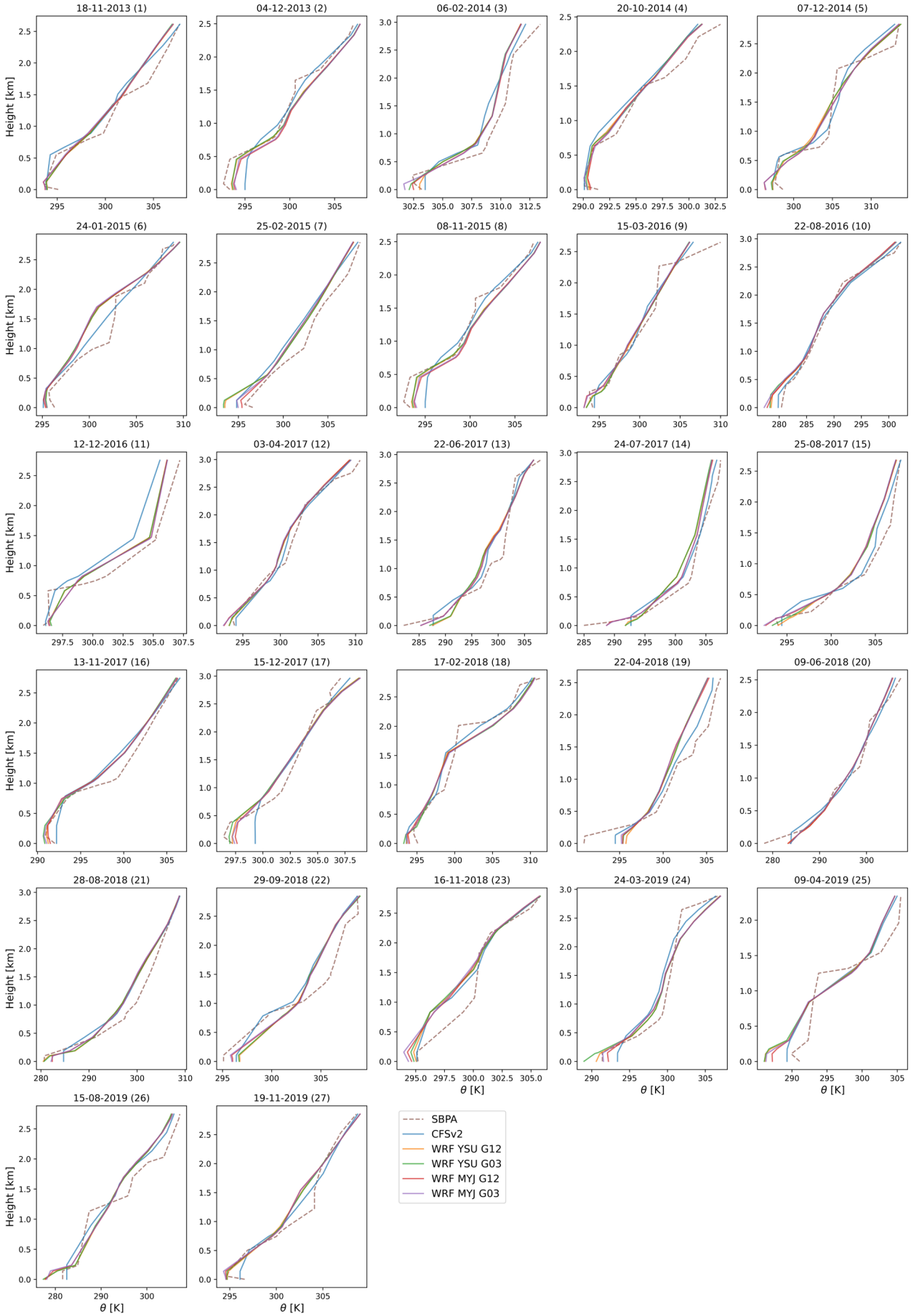

Fig. S4. Lowest 3 km vertical profiles of potential temperature (θ) for each case day.

3. Meteorological conditions on case days

Table S1. Meteorological conditions on case days measured in SBPA station at 12 UTC.

Case Day	Date	Season	Air T [ºC]	PWV [mm]	Wind Speed [m/s]
1	18-Nov-13	spring	23.0	15.71	9.72
2	4-Dec-13	spring	21.0	24.31	7.78
3	6-Feb-14	summer	31.0	41.00	11.66
4	20-Oct-14	spring	19.8	11.77	7.78
5	7-Dec-14	spring	26.6	19.94	13.61
6	24-Jan-15	summer	24.4	26.56	7.78
7	25-Feb-15	summer	24.6	32.59	5.83
8	8-Nov-15	spring	24.4	27.94	15.55
9	15-Mar-16	summer	22.8	22.33	9.72
10	22-Aug-16	winter	9.4	9.11	11.66
11	12-Dec-16	summer	23.4	32.65	17.49
12	3-Apr-17	autumn	22.0	33.12	11.66
13	22-Jun-17	winter	10.6	18.49	5.83
14	24-Jul-17	winter	13.4	19.32	1.94
15	25-Aug-17	winter	22.2	28.23	5.83
16	13-Nov-17	spring	20.0	18.28	11.66
17	15-Dec-17	spring	25.2	31.74	5.83
18	17-Feb-18	summer	23.4	23.63	17.49
19	22-Apr-18	autumn	19.0	32.63	3.89
20	9-Jun-18	autumn	6.6	8.43	0.00
21	28-Aug-18	winter	9.4	6.03	5.83
22	29-Sep-18	spring	23.0	35.96	9.72
23	16-Nov-18	spring	23.6	17.40	9.72
24	24-Mar-19	autumn	25.8	25.28	7.78
25	9-Apr-19	autumn	19.6	17.23	3.89
26	15-Aug-19	winter	10.8	10.82	5.83
27	19-Nov-19	spring	24.8	23.32	3.89

3.2 Artigo 2: Land Surface Temperature retrieval using high-resolution vertical profiles simulated by WRF model

Artigo submetido para avaliação e que contempla os dois últimos objetivos específicos desta dissertação.

DIAZ, Lucas Ribeiro *et al*. Land Surface Temperature retrieval using high-resolution vertical profiles simulated by WRF model. 2021.

Land Surface Temperature retrieval using high-resolution vertical profiles simulated by WRF model

Abstract: This work gives a first insight into the potential of the Weather Research and Forecasting (WRF) model to provide high-resolution vertical profiles for Land Surface Temperature (LST) retrieval from Thermal infrared (TIR) remote sensing. WRF numerical simulations were conducted to downscaling NCEP Climate Forecast System Version 2 (CFSv2) reanalysis profiles, using two nested grids with horizontal resolutions of 12 km (G12) and 3 km (G03). We investigated the utility of these profiles in the atmospheric correction of TIR data and LST estimation. For that, the MODerate resolution atmospheric TRANsmission (MODTRAN) model and Landsat 8 TIRS10 band were used. The accuracy evaluation was performed using in situ radiosondes in Southern Brazil. We included in the comparative analysis the NASA's Atmospheric Correction Parameter Calculator (ACPC) web-tool and profiles directly from the NCEP CFSv2 reanalysis. The atmospheric parameters from ACPC, followed by CFSv2, were in better agreement with those calculated using in situ radiosondes. When applied into the Radiative Transfer Equation (RTE) to retrieve LST, the best results (RMSE) were, in descending order: CFSv2 (0.55 K), ACPC (0.56 K), WRF G12 (0.79 K), and WRF G03 (0.82 K). Our findings suggest that there is no special need to increase the horizontal resolution of reanalysis profiles aiming at RTE-based LST retrieval. However, the WRF results are yet satisfactory and promising, encouraging further assessments. We endorse the use of the well-known ACPC and recommend the NCEP CFSv2 profiles for TIR remote sensing atmospheric correction and LST single-channel retrieval.

Keywords: Thermal infrared (TIR); Reanalysis; Landsat; Radiative Transfer Equation (RTE); NCEP CFSv2; Numerical Weather Prediction (NWP).

1. Introduction

Land Surface Temperature (LST) is one of the Essential Climate Variables (ECVs) of the Global Climate Observation System (GCOS) (Cao et al., 2019; WMO, 2016). It is closely connected to Earth-atmosphere interactions, playing a pivotal role in surface energy and water balances at both local and global scales (Anderson et al., 2008; Tardy et al., 2016; Wu et al., 2021). Therefore, LST is a key parameter in a wide range of environmental applications (Sobrino et al., 2016): urban heat islands studies (Montaner-Fernández et al., 2020); numerical weather prediction (Candy et al., 2017); agricultural, forests, and drought monitoring (Hu et al., 2019; Jiménez-Muñoz et al., 2016; Magarreiro et al., 2019); monitoring of geothermal activities and natural hazards (Gemitzi et al., 2021; Pavlidou et al., 2019); evapotranspiration estimation (Anderson et al., 2021; Rocha et al., 2020); fire detection (Maffei et al., 2018; Singh et al., 2020); water resource management (Anderson et al., 2012; Tavares et al., 2020). It is worth mentioning that the LST should not be confused with the near-surface air temperature (typically measured by meteorological/in situ stations), the LST refers to the so-called "skin temperature" (Jiménez-Muñoz et al., 2016).

Thermal infrared (TIR) remote sensing is a one-off way of obtaining the LST at regional and global scales (Meng and Cheng, 2018; Rosas et al., 2017). However, the spectral radiance measured by TIR sensors onboard satellites is influenced not only by the surface parameters (emissivity and temperature) but also by the composition and structure of the atmosphere (mainly water vapor) (Jiménez-Muñoz et al., 2010; Z.-L. Li et al., 2013). Thus, these atmospheric effects must be removed to the appropriate use of TIR remote sensing data in temperature research applications (Galve et al., 2018; Tang and Li, 2014; Tardy et al., 2016). In general terms, the conversion of the Top Of the Atmosphere (TOA) measurements to the ground-level. This process is referred to as Atmospheric Correction (AC) and its neglect results in systematic errors in the estimation of the LST for any atmosphere (Barsi et al., 2005; Jiménez-Muñoz et al., 2010).

One of the widely applied methodologies to AC and LST retrieval is the physics-based Radiative Transfer Equation (RTE) method (Price, 1983). It involves a simple inversion of the RTE for a particular channel and can provide theoretically accurate LST retrieval (Z.-L. Li et al., 2013). The RTE approach requires vertical atmospheric profiles. This information is introduced into a Radiative Transfer Model (RTM) to calculate the three atmospheric parameters necessary for AC: atmospheric transmittance, upwelling atmospheric radiance, and downwelling atmospheric radiance (Barsi et al., 2003; Jiménez-Muñoz et al., 2010). In situ radiosonde profiles launched simultaneously with the satellite overpass are ideal for AC (Sekertekin, 2019; Sobrino et al., 2004). Nevertheless, this kind of profile is unavailable under the most realistic conditions (Coll et al., 2012; Meng and Cheng, 2018; Pérez-Planells et al., 2015), as local radiosonde launching has a significant financial cost (Jiménez-Muñoz et al., 2010; Z.-L. Li et al., 2013). There are radiosonde stations with atmospheric profiles databases, launched daily around the globe (e.g., in airports). But these data may be either non-synchronously or too far away from the scene footprint (Mira et al., 2014; Tardy et al., 2016). Hence, local radiosondes became suitable only for particular local studies and validation at specific sites mainly (Coll et al., 2005; Rosas et al., 2017).

Therefore, atmospheric profile products from different sources have been used to surrogate radiosondes in TIR atmospheric correction, resulting in LSTs with acceptable accuracy (Duan et al., 2018; Galve et al., 2018; Malakar et al., 2018; Mattar et al., 2015; Tardy et al., 2016; Vanhellemont, 2020a). Satellite-derived profiles overcome the spatial limitations of local radiosondes. These are available at the satellite pixel scale, providing a large spatial extent. Even though have a high spatial resolution, the satellite-derived profiles can be compromised by low temporal ones (only at the satellite overpassing time) (Rosas et al., 2017; Yang et al., 2020). Thus, the results may not be desirable when the sensor of interest is not (or concurrent with) the one witch the profiles are derived (Coll et al., 2012; Galve et al., 2018). Surpassing this temporal limitation, profiles from global reanalysis data provide a flexible temporal resolution (typically 3 and 6 hourly) and are a practical alternative to the radiosondes spatial constraint (Rosas et al., 2017). Reanalysis datasets are global gridded extended homogeneous time series, with no spatial nor temporal gaps (Alghamdi, 2020).

Barsi et al. (2005, 2003) proposed an atmospheric web-based correction tool (Atmospheric Correction Parameter Calculator – ACPC) for Landsat 5, 7, and 8 thermal bands. It uses reanalysis profiles from the National Center for Environmental Prediction (NCEP) and the code of the MODerate resolution atmospheric TRANsmission (MODTRAN) model (Berk et al., 2014) to directly provide the three atmospheric parameters for AC. Additionally, researchers have evaluated and compared the efficacy of different reanalysis and satellite-based profile products for AC/LST retrieval. NCEP reanalysis (Reanalysis 1 (Kalnay et al., 1996) and FNL (NCEP et al., 2000)) and Moderate Resolution Radiometer (MODIS) atmospheric profiles product (MOD07) (Borbas and Menzel, 2017) were analyzed for different sites in Spain (Jiménez-Muñoz et al., 2010; Pérez-Planells et al., 2015; Skokovic et al., 2017) and in China (H. Li et al., 2013) for TIR sensors as Landsat, ASTER, and HJ-1B IRS. Coll et al. (2012), also in Spain, added the satellite-based profiles from Atmospheric Infrared Sounder (AIRS) (Aumann et al., 2003) in the comparison. Rosas et al. (2017) in its turn included the European Centre for Medium-Range Weather Forecasts (ECMWF) ERA-Interim reanalysis product (Dee et al., 2011) along with previous profiles for Landsat 8 LST estimates in Saudi Arabia. More recently, assessments with a greater number of different profile products were carried out. Meng and Cheng (2018) evaluated reanalysis products from Modern Era Retrospective-Analysis for Research and Applications (MERRA) (Rienecker et al., 2011) 1 and 2, ERA-Interim, NCEP FNL and NCEP Reanalysis 2 (Kanamitsu et al., 2002), and Japanese Reanalysis (JRA)-55 (Kobayashi et al., 2015). Their validation included profiles distributed around the globe and 32 Landsat 8 band 10 images over China. Yang et al. (2020) assessed seven profiles source (AIRS, MOD07, ERA-Interim, MERRA 2, and NCEP FNL, Reanalysis 2, GFS) using 17 radiosonde stations over Europe and in situ LST measurements in China. Overall, the accuracies of AC parameters and retrieved LST using satellite-derived profiles are lower than that using reanalysis ones (Coll et al., 2012; H. Li et al., 2013; Pérez-Planells et al., 2015; Skokovic et al., 2017; Yang et al., 2020).

However, reanalysis profiles also have their disadvantages. The spatial resolution with several degrees (varying for each product) can be considered low. The accuracy is usually poorer for regions with less coverage of permanent observatories, like the oceans and many Southern Hemisphere zones (Alghamdi, 2020; Chen and Liu, 2016; Chen et al., 2014). Since the data is spaced at grid points with time intervals of commonly 6 h, the description of meteorological phenomena on a sub-grid or variable time scale may be affected (Tonooka, 2001). On the other hand, modern numerical weather models benefit from computing performance and physical processes parameterization to downscaling the reanalysis data. Mesoscale atmospheric models use global (re)analysis models as initial and boundary conditions for local applications (Hassanli and Rahimzadegan, 2019; Wee et al., 2012). Lee et al., (2020) employed high-resolution (1.5 and 12 km) Numerical Weather Prediction (NWP) models distributed by the Korea Meteorological Administration (KMA) as input atmospheric data for AC and sea surface temperature estimation with Visible Infrared Imaging Radiometer Suite (VIIRS) bands. Their KMA NWP dataset is restricted to eastern Asia, but the approach of high-resolution NWP models combined with RTM is an interesting background for studies of TIR remote sensing atmospheric correction.

The Weather Research and Forecasting (WRF) model (Skamarock et al., 2019) is an atmospheric modeling system designed for both research and NWP. It is a state-of-the-art mesoscale model and the world's most widely used. Non-hydrostatic, open-source, free, community-based, and with a wide range of parameterization options, the WRF model provides a spectrum of capabilities for a variety of applications in atmospheric science and weather prediction (Powers et al., 2017). From that, the WRF model has been extensively employed for estimating high-resolution meteorological data (Fekih and Mohamed, 2019; Kioutsioukis et al., 2016; Moya-Álvarez et al., 2020; Mylonas et al., 2019; Onwukwe and Jackson, 2020).

It is imperative to assess the reasonableness of using the WRF model to generate high-resolution atmospheric vertical profiles to, in conjunction with an RTM, have a higher AC/LST retrieval accuracy. Moreover, almost all studies that evaluated different profile sources for LST retrieval were performed over Asia and Europe. To the best of our knowledge, no paper has carried out such an assessment in South America. There is also a lack of studies using newer and finer reanalysis profiles (e.g., ERA5 (Hersbach et al., 2020) and NCEP Climate Forecast System Version 2 (CFSv2) (Saha et al., 2014)) for AC and LST estimation (Vanhellemont, 2020a, 2020b).

This study conducts simulations with the WRF Model using NCEP CFSv2 reanalysis data as initial and boundary conditions. Its objective is to generate high-resolution vertical profiles, improving the spatial, temporal, and vertical resolutions of the global reanalysis. We intend to investigate the utility of these profiles in TIR atmospheric correction and LST retrieval, in relation to the ACPC web-tool and profiles extracted directly from the NCEP CFSv2 reanalysis. We take Landsat 8 TIRS band 10 as an example to retrieve LST values, through an RTE inversion-based algorithm in conjunction with the MODTRAN radiative transfer model. The accuracy assessment was performed using local radiosonde observation in Southern Brazil.

2. Materials and Methods

2.1. Study area and in situ radiosonde data

The Porto Alegre International Airport (SBPA), Rio Grande do Sul State, Brazil was selected as the study area. The airport includes a radiosonde station, which made this site a useful environment for studies that aim to evaluate atmospheric profiles. The selected area covers the official limits of the Anchieta district (Porto Alegre City Hall, 2016), with an area of around 9.2 km² (Fig. 1). According to Köppen's climate classification, the local climate is subtropical humid with hot summers (Cfa) (Alvares et al., 2013), with a mean annual air temperature of 19.6 ºC, mean annual relative humidity of 76.1 %, and mean annual precipitation of 1397 mm (Matzenauer et al., 2011).

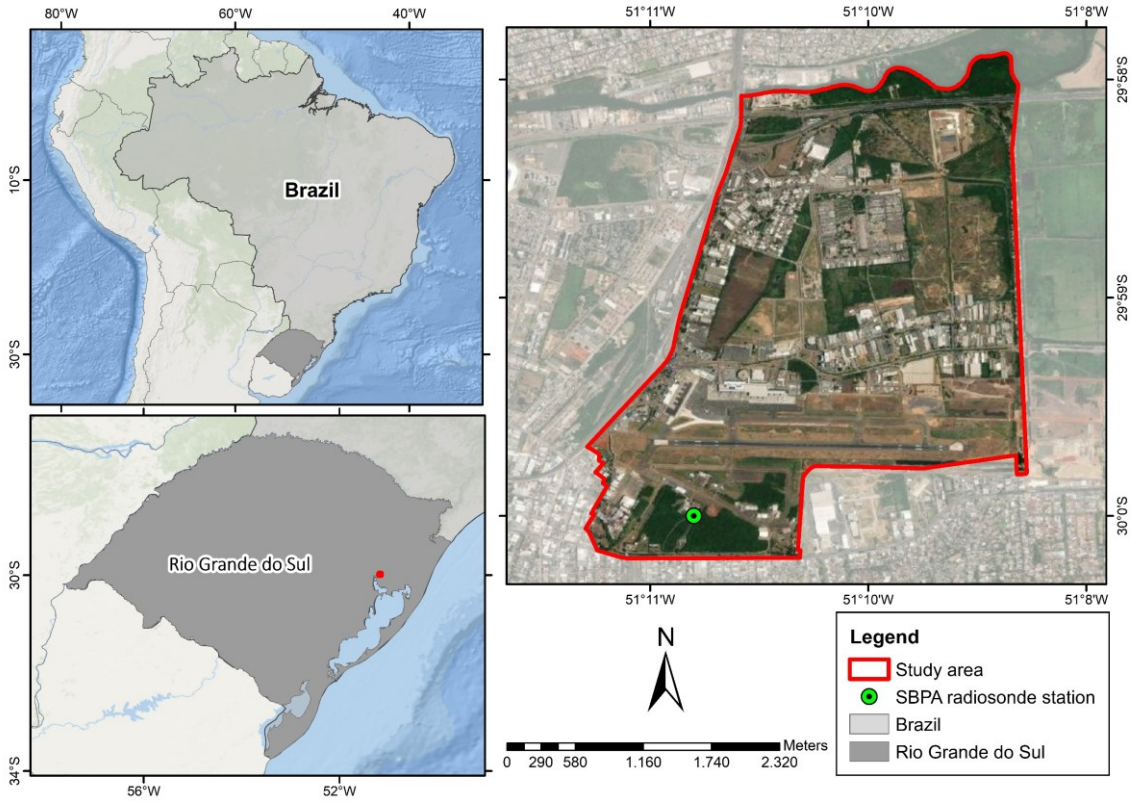

Fig. 1. Map of the study area showing the Porto Alegre Airport (SBPA) radiosonde station, Southern Brazil.

The SBPA station is located at 30.00º S and 51.18º W, 3.0 m above mean sea level, and its identifier number is 83971. In this station, radiosondes are launched twice a day, at 00:00 and 12:00 UTC. In this paper, we used the 12:00 UTC radiosonde profiles, as this is the closest time to the Landsat 8 crossing time over the study site (~13 UTC). Data were obtained from the University of Wyoming website (http://weather.uwyo.edu/upperair/sounding.html). This dataset allows characterizing the vertical structure of the atmosphere with profiles of air temperature, pressure, humidity with up to 99 vertical levels. The radiosonde observations, as well as the parameters calculated from them, are considered as ground truth for the assessments in this study.

2.2. Landsat 8 satellite data and case days

The Landsat mission has been providing moderate-resolution space-based surface observations for almost 50 years. Landsat 8 is the most recent operational satellite of the series and was launched in February 2013. It carries a two-sensor payload: the Operational Land Imager (OLI) thas has nine reflective (visible, near-infrared, and short-wave infrared) bands with 30-m spatial resolution and the Thermal Infrared Sensor (TIRS) with two bands in the TIR region. The TIRS bands have a 100-m spatial resolution but it is resampled and provided at 30-m by the United States Geological Survey (USGS) to be consistent with the OLI bands (Roy et al., 2014; Sekertekin and Bonafoni, 2020a).

In this study, we acquired all Landsat 8 images (Collection 1) available under daily clear-sky conditions over the study area from 2013 to 2019. Which resulted in a total of 27 scenes at Path-Row 221-81, with acquisition scene center time around 13:20 UTC. The full swath Landsat data were subset to a 10,184 pixels region covering the study area of Fig. 1. Table 1 presents the specifications of Landsat 8 data utilized in the study, as well as the case days that henceforward will be used to refer to each one. Seeking to illustrate the meteorological conditions near the acquisition time, we also bring in Table 1 the air temperature and the water vapor content in the atmosphere, through the Precipitable Water Vapor (PWV) for the entire radiosonde column measured by the SBPA station. The TIRS band 10 (10.60–11.19 μm) is used for RTE-based LST retrieval (Section 2.6.2) and OLI bands 4 – red (0.64–0.67 μm) and 5 – near-infrared (0.85–0.88 μm) for land surface emissivity estimation (Section 2.5).

Table 1. Information about Landsat 8 data used in the paper (27 images from 2013 to 2019, Path-Row 221-81). The last columns present meteorological conditions measured by the SBPA station.

Scene ID	Acquisition Date	Case Day	Season	Air T [ºC]	PWV [g/cm²]
LC82210812013322LGN01	18-Nov-13	1	spring	23	1.57
LC82210812013338LGN01	04-Dec-13	2	spring	21	2.43
LC82210812014037LGN01	06-Feb-14	3	summer	31	4.10
LC82210812014293LGN01	20-Oct-14	4	spring	19.8	1.18
LC82210812014341LGN01	07-Dec-14	5	spring	26.6	1.99
LC82210812015024LGN01	24-Jan-15	6	summer	24.4	2.66
LC82210812015056LGN01	25-Feb-15	7	summer	24.6	3.26
LC82210812015312LGN01	08-Nov-15	8	spring	24.4	2.79
LC82210812016075LGN01	15-Mar-16	9	summer	22.8	2.23
LC82210812016235LGN02	22-Aug-16	10	winter	9.4	0.91
LC82210812016347LGN01	12-Dec-16	11	summer	23.4	3.27
LC82210812017093LGN01	03-Apr-17	12	autumn	22	3.31
LC82210812017173LGN00	22-Jun-17	13	winter	10.6	1.85
LC82210812017205LGN00	24-Jul-17	14	winter	13.4	1.93
LC82210812017237LGN00	25-Aug-17	15	winter	22.2	2.82
LC82210812017317LGN00	13-Nov-17	16	spring	20	1.83
LC82210812017349LGN00	15-Dec-17	17	spring	25.2	3.17
LC82210812018048LGN00	17-Feb-18	18	summer	23.4	2.36
LC82210812018112LGN00	22-Apr-18	19	autumn	19	3.26
LC82210812018160LGN00	09-Jun-18	20	autumn	6.6	0.84
LC82210812018240LGN00	28-Aug-18	21	winter	9.4	0.60
LC82210812018272LGN00	29-Sep-18	22	spring	23	3.60
LC82210812018320LGN00	16-Nov-18	23	spring	23.6	1.74
LC82210812019083LGN00	24-Mar-19	24	autumn	25.8	2.53
LC82210812019099LGN00	09-Apr-19	25	autumn	19.6	1.72
LC82210812019227LGN00	15-Aug-19	26	winter	10.8	1.08
LC82210812019323LGN00	19-Nov-19	27	spring	24.8	2.33

2.3. Reanalysis data

NCEP Climate Forecast System Version 2 (CFSv2) (Saha et al., 2014) reanalysis data is produced using the NCEP Global Forecasting System (GFS) atmospheric model and the Grid point Statistical Interpolation (GSI) analysis system with three-dimensional variational data assimilation (3D-Var). It is arranged in grids with a horizontal resolution of 0.5º x 0.5º and in 37 vertical (pressure) levels (1000 – 1 mbar), and 0.205º for surface parameters. We used CFSv2 reanalysis data from the 6-hourly product as initial and boundary conditions for the WRF simulations. In addition, profiles retrieved directly from NCEP CFSv2 were included in the analysis, to assess the WRF model downscaling performance. These profiles were extracted from the grid point closest to the SBPA station.

2.4. WRF Model configuration

The WRF Model version 4.1.2 with the Advanced Research WRF (ARW) dynamical solver (Skamarock et al., 2019; Wang et al., 2019) was used to perform high-resolution numerical simulations. We configured the WRF domains with two nested grids, in one-way mode, centered at SBPA station, with horizontal resolutions of 12 km (G12) and 3 km (G03) (4:1 parent grid ratio), and 33 sigma vertical levels with 50 hPa top pressure value. Fig. 2 exhibits the grids and also an asterisk that indicates where the profiles resulted from simulations were extracted, it refers to the grid point closest to the SBPA station. The time step used for the outermost domain was 72s with a 4:1 parent ratio. Geographical static data such as land use, topography, albedo, and reflectance, are inserted into the modeling process by the land use categories of USGS.

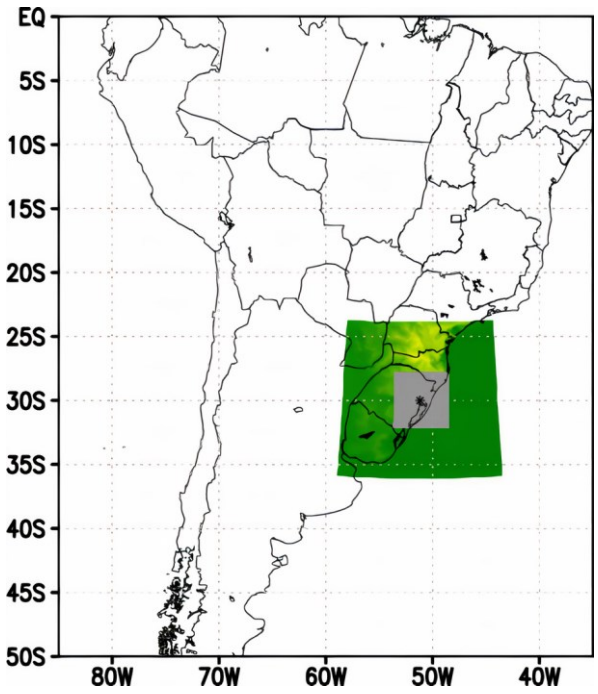

Fig. 2. WRF nested grids used in the study: G12 (shades of green) and G03 (gray). The asterisk indicates the point where the results were retrieved.

Some atmospheric physical processes cannot be directly resolved by the numerical model and so need to be parameterized. Parametrization schemes represent the contribution of unresolved, but important, phenomena in terms of variables resolved at the model discrete grid (García-Díez et al., 2013; Stensrud, 2007; Xie et al., 2012). The WRF model has a vast range of parameterization scheme options. The physics parameterization chosen for our simulations included: Purdue Lin microphysics parametrization (Chen and Sun, 2002); Yonsei University (YSU) Planetary Boundary Layer (PBL) scheme (Hong et al., 2006); Betts–Miller–Janjic (BMJ) cumulus scheme (Janjić, 1994); Dudhia shortwave radiation (Dudhia, 1989); Rapid Radiative Transfer Model (RRTM) longwave radiation option (Mlawer et al., 1997); Unified NOAH Land-Surface Model (LSM) (Tewari et al., 2004); and Revised MM5 surface-layer scheme (Jiménez et al., 2012). In our previous paper (Diaz et al., 2021), we tested some parametrization options for the same SBPA area and the set used here is based on its results and in those of Santos and Nascimento (2016). The WRF configurations are summarized in Table 2.

Table 2. Overview of WRF model setting.

WRF Model Configuration	
Version	4.1.2
Dynamical solver	ARW
Initial and boundary conditions	NCEP CFSv2
Map projection	Lambert
Grid size	Domain 1: (119 x 116) x 33 Domain 2: (169 x 165) x 33
Horizontal resolution	Domain 1: 12 km Domain 2: 3 km
Nesting	One-way
Time step	72s
Static geographical data	USGS
Cloud Microphysics	Purdue Lin
PBL	YSU
Cumulus	BMJ (Domain 1 only)
Shortwave Radiation	Dudhia
Longwave Radiation	RRTM
LSM	Unified NOAH
Surface-layer	Revised MM5

The WRF model was run in the above configurations for each of the case days in Table 1. We conduct simulations of 24-h duration and the resulting profiles were extracted at 12:00 UTC, to match with the local radiosonde observations. Hence, the first 12 h of the simulation was considered for spin up time. The model output for each domain was stored every 30 minutes.

2.5. Land Surface Emissivity Estimation

Land Surface Emissivity (LSE) is one of the key parameters to retrieve LST from remote sensing data. It is a measure of the surface intrinsic ability in converting heat energy

into radiant energy. LSE is a function of the composition, roughness, and moisture of the surface and the observation conditions (Z. L. Li et al., 2013; Sekertekin and Bonafoni, 2020a; Sobrino et al., 2001). Among the methods for LSE retrieval from space, Normalized Difference Vegetation Index (NDVI)-based ones are operational and the most applied, with satisfactory results (Käfer et al., 2019; Li and Jiang, 2018; Sobrino et al., 2001, 2008; Valor and Caselles, 1996; Van de Griend and Owe, 1993; Yu et al., 2014). Sekertekin and Bonafoni (2020a, 2020b) examined the influence of six NDVI-based LSE models on the performance of LST retrieval. Based on their results, we opted to use the NDVI threshold method ($NDVI^{THM}$) of Sobrino et al. (2008). The LSE estimation from satellites inevitably has errors and NDVI-based methods also have their limitations, especially in urban environments (Oltra-Carrió et al., 2012). On the other hand, a recent study (Harod et al., 2021) reported that the use of LSE estimated by different methods resulted in no significant variations in the LST accuracy. Anyway, assessing the LSE estimation is beyond the scope of this paper.

To calculate NDVI from Landsat 8 data, the first step is to convert Digital Number (DN) values of bands 4 (red) and 5 (near-infrared – NIR) to reflectance using Equation (1). And then, NDVI is obtained from Equation (2) (Ihlen and Zanter, 2019; Sekertekin and Bonafoni, 2020b). It is not necessary to correct atmospheric effects in red and NIR bands to estimate LSE (Jiménez-Muñoz et al., 2009).

$$\rho_\lambda = \frac{M_p \cdot Q_{CAL} + A_p}{\sin \theta_{SE}} \tag{1}$$

where ρ_λ is the reflectance of the corresponding band, M_p is the multiplicative rescaling factor of the corresponding band, Q_{CAL} is the calibrated and quantized standard product pixel values (DNs), A_p is the additive rescaling factor of the corresponding band, and θ_{SE} is the local sun elevation angle.

$$NDVI = \frac{\rho_{NIR} - \rho_R}{\rho_{NIR} + \rho_R} \tag{2}$$

where ρ_{NIR} is the reflectance of the NIR band and ρ_R the reflectance of the red one.

From NDVI it is possible to calculate the Fractional Vegetation Cover (P_V) from Equation (3) (Carlson and Ripley, 1997). The P_V is an important factor in the LSE estimation.

$$P_V = \left[\frac{NDVI - NDVI_{min}}{NDVI_{max} - NDVI_{min}}\right]^2 \tag{3}$$

where $NDVI_{min}$ = 0.2 and $NDVI_{max}$ = 0.5 in a global context (Sobrino et al., 2008, 2004; Sobrino and Raissouni, 2000).

The $NDVI^{THM}$ proposed by (Sobrino et al., 2008) estimates LSE considering three different cases as presented in Equation (4), for Landsat 8 (Sekertekin and Bonafoni, 2020a).

For NDVI < 0.2, the pixel is considered as bare soil, and the emissivity is calculated using the reflectance of the red band. In the second case (0.2 ≤ NDVI ≤ 0.5), the pixel is considered composed of a mixture of bare soil and vegetation and the LSE depends on the P_V value. The pixels with NDVI values higher than 0.5 are considered as fully vegetated areas and the emissivity is assumed as 0.99.

$$\varepsilon = \begin{cases} 0.979 - 0.035\rho_R & NDVI < 0.2 \\ 0.004P_V + 0.986 & 0.2 \leq NDVI \leq 0.5 \\ 0.99 & NDVI > 0.5 \end{cases} \quad (4)$$

where ε is the Land Surface Emissivity (LSE).

2.6. Atmospheric correction and LST Retrieval

2.6.1. Atmospheric parameters calculation with MODTRAN and ACPC

The MODTRAN (MODerate resolution atmospheric TRANsmission) is a commercial and widely employed atmospheric RTM developed by the U.S. Air Force and the Spectral Sciences Inc. (Berk et al., 2014). The present study used the MODTRAN4 v3r1 (Berk et al., 2003) to estimate the three atmospheric correction parameters (i.e., atmospheric transmittance, upwelling atmospheric radiance, and downwelling atmospheric radiance) in the Landsat TIR spectrum. We introduced into the MODTRAN as input vertical profiles of pressure, air temperature, and relative humidity from: (i) SBPA radiosonde; (ii) NCEP CFSv2 reanalysis; (iii) WRF G12; and (iv) WRF G03. The atmospheric parameters calculated from SBPA profiles are treated as ground truth data.

The methodology of Barsi et al. (2003) to fulfill the profiles was adopted. To predict space-reaching atmospheric parameters, the MODTRAN requires atmospheric profiles reaching “space”, or 100 km above sea level. Since the radiosondes and NCEP CFSv2 are from the surface to about 30 and 50 km, respectively, the upper atmosphere layers (to 100 km) are extracted from the MODTRAN standard atmospheres and pasted onto our site-specific profiles. We take on the standard mid-latitude summer profile for case days in hot seasons (spring and summer) and the mid-latitude winter profile for those in cold seasons (autumn and winter). This results in surface-to-space vertical profiles of air temperature, pressure, and water vapor. These completed profiles are those that are inserted into a MODTRAN input file and then processed (Barsi et al., 2005, 2003).

MODTRAN outputs are provided in the model's spectral resolution, so an integration has to be performed between the bounds defined by the spectral response curve of the sensors band (Equation (5)) (Tardy et al., 2016). In this case, the Landsat 8 TIRS band 10 (TIRS10).

$$var\ (\lambda_i) = \frac{\int_{\lambda_{i,min}}^{\lambda_{i,max}} var\ (\lambda) R_s(\lambda) d\lambda}{\int_{\lambda_{i,min}}^{\lambda_{i,max}} R_s(\lambda) d\lambda} \quad (5)$$

where R_s is the spectral response of the sensor at the center wavelength λ_i of a band with a spectral window of $\lambda_{i,min} - \lambda_{i,max}$. var alternatively denotes the atmospheric parameter (transmittance, upwelling, or downwelling radiance) value extracted from the MODTRAN output file, between the edges wavelengths.

Additionally, we include in the comparative analysis the atmospheric parameters estimated by the well-established NASA's Atmospheric Correction Parameter Calculator (ACPC) web-tool (Barsi et al., 2005, 2003). As mentioned above, the ACPC uses NCEP reanalysis profiles (with 1°x1° horizontal resolution and 28 vertical levels), MODTRAN code, and a suite of integration algorithms to provide the AC parameters for a particular date, time, and location inputted. The option of using the atmospheric profile from the closest integer coordinate to the inputted location (SBPA station) was set. The mid-latitude standard upper profiles varied according to the season of each case day.

2.6.2. Radiative Transfer Equation (RTE) based LST Retrieval method

The inverse solution of RTE (Price, 1983) is a direct and *a priori* the most appropriate procedure for LST retrieval using a single TIR band (Jiménez-Muñoz et al., 2009). The RTE applied to a particular TIR band/wavelength (λ) can be simplified and given by:

$$L_\lambda^{sen} = \left[\varepsilon_\lambda B_\lambda(T_s) + (1-\varepsilon_\lambda)L_\lambda^{\downarrow}\right]\tau_\lambda + L_\lambda^{\uparrow} \tag{6}$$

where L_λ^{sen} ($W{\cdot}m^{-2}{\cdot}sr^{-1}{\cdot}\mu m^{-1}$) is the at-sensor (TOA) spectral radiance of the corresponding TIR band (in this paper, TIRS10), ε_λ refers to the LSE (dimensionless), B_λ ($W{\cdot}m^{-2}{\cdot}sr^{-1}{\cdot}\mu m^{-1}$) is the blackbody radiance, T_s (Kelvin) represents the LST, $L_\lambda^{\downarrow}$ and $L_\lambda^{\uparrow}$ ($W{\cdot}m^{-2}{\cdot}sr^{-1}{\cdot}\mu m^{-1}$) refer to the downwelling and upwelling radiances, respectively, and τ_λ is the atmospheric transmittance (dimensionless). So the emitted radiance for a black body at a temperature T_s is given by the inversion of Equation (6):

$$B_\lambda(T_s) = \frac{L_\lambda^{sen} - L_\lambda^{\uparrow} - \tau(1-\varepsilon_\lambda)L_\lambda^{\downarrow}}{\tau_\lambda \varepsilon_\lambda} \tag{7}$$

the L_λ^{sen} of Landsat 8 TIRS10 is obtained converting the DN values (Q_{CAL}) applying Equation (8) (Ihlen and Zanter, 2019):

$$L_\lambda^{sen} = M_L \cdot Q_{CAL} + A_L \tag{8}$$

where M_L and A_L are the multiplicative and additive rescaling factors of the corresponding band (TIRS10). In addition, B_λ comes from Planck's law:

$$B_\lambda(T) = \frac{C_1}{\lambda^5(e^{C_2/\lambda T} - 1)} \tag{9}$$

where C_1 = 1.19104 x 10^8 W·μm^4·m^{-2}·sr^{-1} and C_2 = 14387.7 μm·K are Planck's radiation constants. Thus, the T_s is calculated by inverting Planck's law in Equation (7):

$$T_s = \frac{C_2}{\lambda}\left[\ln\left(\frac{C_1}{\lambda^5\left[\frac{L_\lambda^{sen} - L_\lambda^{\uparrow}}{\varepsilon_\lambda \tau_\lambda} - \left(\frac{1-\varepsilon_\lambda}{\varepsilon_\lambda}\right)L_\lambda^{\downarrow}\right]} + 1\right)\right]^{-1} \quad (10)$$

finally, Equation (10) can be simplified and the LST (T_s) from Landsat 8 TIRS10 is estimated as:

$$LST = \frac{K_2}{\ln\left(\frac{K_1}{\frac{L_\lambda^{sen} - L_\lambda^{\uparrow} - \tau_\lambda(1-\varepsilon_\lambda)L_\lambda^{\downarrow}}{\tau_\lambda \varepsilon_\lambda}} + 1\right)} \quad (11)$$

where K_1 and K_2 refers to calibration constants, whose values for the Landsat 8 TIRS10 are 774.89 W·m^{-2}·sr^{-1}·μm^{-1} and 1321.08 K, respectively (Ihlen and Zanter, 2019). Henceforth, the spectral notation (λ) will be omitted, since here only a single TIR band is used.

The aforementioned procedure was applied with τ, $L^{\uparrow}$, and $L^{\downarrow}$ calculated using profiles from:

(1) SBPA local radiosonde;
(2) NCEP CFSv2 reanalysis;
(3) WRF G12;
(4) WRF G03;
(5) ACPC.

The LST images retrieved using atmospheric parameters from SBPA radiosondes are considered as a "ground truth", and LST retrievals considering the other cases have been compared to it. As detailed in the next section.

2.7. Metrics for performance evaluation

To evaluate the performance of the WRF model and other profiles we take into account the atmospheric parameters (τ, $L^{\uparrow}$, and $L^{\downarrow}$) and LST images. The SBPA radiosondes are the available in situ observations. Hence, the AC parameters and LSTs calculated using SBPA profiles are considered our references. To perform the comparative assessment, Pearson's correlation coefficient (R), bias (mean error), Mean Absolute Error (MAE), and Root Mean Square Error (RMSE) were used as statistical criteria. These metrics are widely

employed to evaluate and compare models (Chai and Draxler, 2014; Sekertekin, 2019; Willmott and Matsuura, 2005). The metrics' equations are given as follows:

$$\mathrm{R} = \frac{\sum_{i=1}^{n}(p_i - \bar{p})(o_i - \bar{o})}{\sqrt{\sum_{i=1}^{n}(p_i - \bar{p})^2}\sqrt{\sum_{i=1}^{n}(o_i - \bar{o})^2}} \tag{12}$$

where p_i and o_i are pairwise predicted and observed values, respectively, n is the number of pairs, and terms with overbars are respective mean values. R scores range from -1 to 1, and values approaching 1 indicate stronger correlations.

$$\mathrm{bias} = \frac{1}{n}\sum_{i=1}^{n} p_i - o_i \tag{13}$$

bias is useful in determining if the model is underestimating (bias < 0) or overestimating (bias > 0) the observed values.

$$\mathrm{MAE} = \frac{1}{n}\sum_{i=1}^{n} |p_i - o_i| \tag{14}$$

is the average of the absolute difference between the predictions and the observations, despite model overestimation or underestimation. It is a negatively oriented index (values closer to zero are better).

$$\mathrm{RMSE} = \sqrt{\frac{1}{n}\sum_{i=1}^{n}(p_i - o_i)^2} \tag{15}$$

RMSE is also negatively oriented. It indicates the deviation between modeled and observed values and is more sensitive to outliers as the errors are squared before summing.

3. Results and discussion

3.1. Evaluation of atmospheric parameters

3.1.1. Overall results

The AC parameters (τ, $L^{\uparrow}$, and $L^{\downarrow}$) calculated with different sources of estimated vertical profiles (CFSv2, WRF G12, WRF G03, and ACPC) were compared against those using observational SBPA radiosondes (Fig. 3). In Table 3, the accuracy of atmospheric parameters estimations is presented. All the profile sources provide AC parameters with high correlation coefficients, all greater than 0.9, in relation to the reference (SBPA). The R values of ACPC, followed by CFSv2, are slightly better. There is a general but small tendency of overestimating the transmittance values. On the other hand, the atmospheric radiances tend to be underestimated, except for ACPC downwelling. The smallest biases were from the WRF

for all three parameters. The largest ones were from CFSv2. Concerning MAE and RMSE, the best results were from ACPC followed by CFSv2. The biggest RMSE value founded was 0.43 $W \cdot m^{-2} \cdot sr^{-1} \cdot \mu m^{-1}$ of the downwelling calculated with WRF G03 profiles.

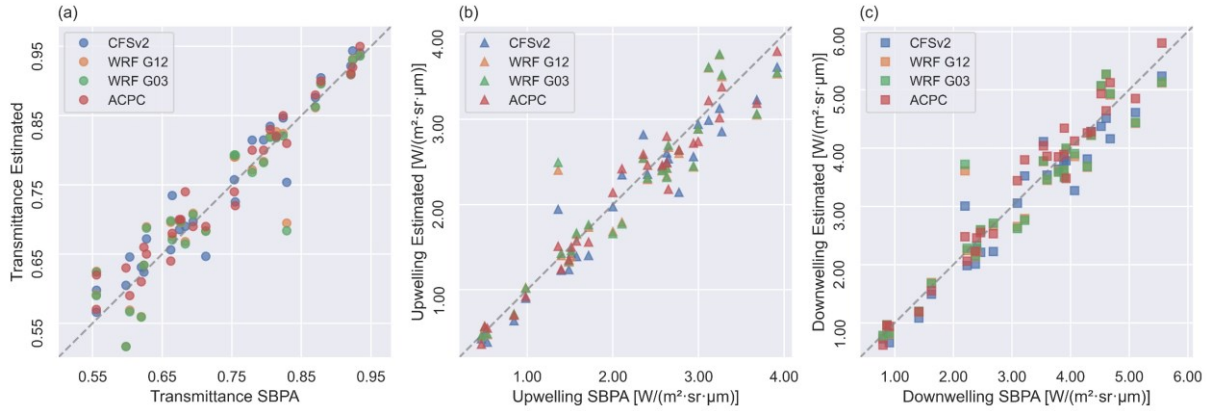

Fig. 3. Comparison of (a) atmospheric transmittance, (b) upwelling radiance, and (c) downwelling radiance calculated with SBPA in situ radiosondes and estimated profile sources. The dashed line represents the "1:1 line".

Table 3. Statistical metrics of atmospheric parameters estimated from different atmospheric profiles. Bias, MAE, and RMSE are in the parameter of interest units, i.e., $W \cdot m^{-2} \cdot sr^{-1} \cdot \mu m^{-1}$ for atmospheric radiances and the transmittance is dimensionless.

		CFSv2	WRF G12	WRF G03	ACPC
Transmittance	R	0.96	0.93	0.93	0.97
	bias	0.01	~0.00	~0.00	0.01
	MAE	0.02	0.03	0.03	0.02
	RMSE	0.03	0.04	0.04	0.03
Upwelling	R	0.97	0.94	0.94	0.98
	bias	-0.12	-0.04	-0.02	-0.06
	MAE	0.21	0.24	0.24	0.16
	RMSE	0.27	0.33	0.34	0.20
Downwelling	R	0.97	0.95	0.95	0.98
	bias	-0.15	-0.05	-0.03	0.08
	MAE	0.28	0.30	0.30	0.21
	RMSE	0.35	0.42	0.43	0.27

The higher negative bias of the atmospheric radiances with NCEP CFSv2 in our findings may be due to these reanalysis profiles have the lowest level at 1000 hPa, which means around 60 – 250 m for SBPA station in our case days. So the lowest layer of the atmosphere (which typically present the largest water vapor content and warmest temperature) is neglected in these profiles. This fact was indicated by Coll et al. (2012) and Meng and Cheng (2018). We had tried to reduce this limitation by downscaling the CFSv2 reanalysis

profiles with the WRF model. The WRF profiles bring the first level at around 1 m above the surface.

Fig. 4 illustrates the performance of the AC parameters from the different profile sources through Taylor diagrams (Taylor, 2001). Those quantify the agreement of the modeled profiles with the observational ones in terms of the graphical representations of three statistics combined: standard deviation, Root Mean Squared Deviation (RMSD, same as RMSE), and correlation coefficient. Fig. 4 corroborates the results shown in Table 3. It indicates that ACPC obtained better results than the other profiles for all 3 atmospheric parameters. After, comes the CFSv2 reanalysis profiles. The diagrams clearly point out that the profiles from WRF G12 and G03 had very similar accuracies. Actually, no significant statistical differences were found between the parameters from the WRF grids G12 and G03. It suggests that computation costs can be saved by using profiles from a WRF domain with coarse horizontal resolution. Despite other aims, scholars have already reported this kind of result with WRF model grids (Hassanli and Rahimzadegan, 2019; Lin et al., 2018; Mohan and Sati, 2016; Pérez-Jordán et al., 2015).

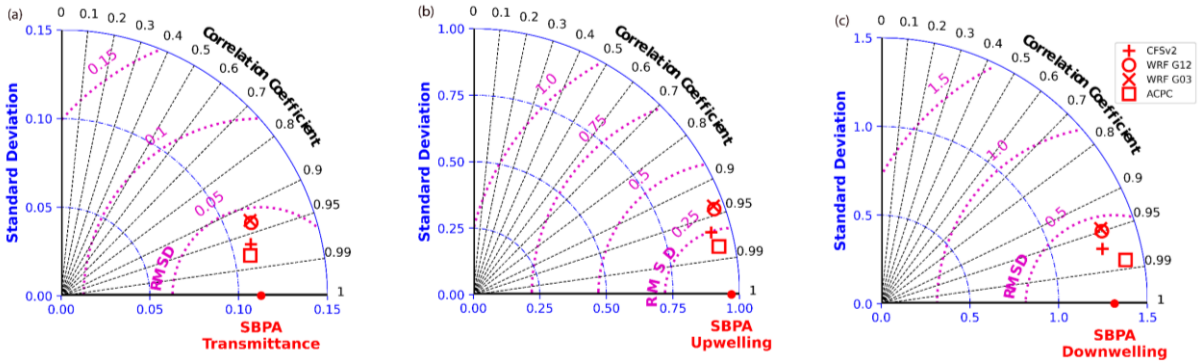

Fig. 4. Taylor diagrams of (a) atmospheric transmittance, (b) upwelling radiance, and (c) downwelling radiance. The parameters calculated with SBPA radiosondes are the references. The black dashed lines represent the correlation coefficient (R), blue dash-dot lines represent the standard deviation, and the magenta dotted lines represent the root mean squared deviation (RMSD = RMSE).

Our RMSE range is in agreement with those findings for reanalysis profiles in Meng and Cheng (2018) for the 3 parameters. The authors analyzed 30,715 atmospheric profiles in 163 stations around the globe. The RMSE values of Yang et al., (2020) were overall slightly lower than ours. But their assessment just includes profiles from Europe. In our previous work (Diaz et al., 2021), we compared the vertical distribution of air temperature and water vapor of the SBPA radiosondes, CFSv2 reanalysis, and WRF (G12 and G03) profiles. The evaluation of the profiles themselves shows that both CFSv2 and WRF model skillfully represent the vertical profiles of temperature and water vapor. Nevertheless, the statistical metrics indicated that increasing the horizontal resolution did not improve significantly the quality of the simulated atmospheric profile. This is in line with the above results of the atmospheric parameters comparison.

3.1.2. Analysis by meteorological conditions

The errors in the estimation of atmospheric parameters for each case day are shown in Fig. 5. It points out that despite ACPC presented the best overall metrics, none of the profile sources outperformed in all cases. For instance, in 8 of the case days, one of the WRF profiles had the best results in calculating the downwelling radiance. In case day 23, the WRF model plainly produced the largest errors, whereas in cases such as 26 the model successfully reduced the largest error of the driving reanalysis data. Therefore, it is pertinent to assess the dependence of meteorological conditions on the different profile sources performance.

Fig. 5. Errors in the estimation of (a) atmospheric transmittance, (b) upwelling radiance, and (c) downwelling radiance from the different profiles for each case day.

Fig. 6 brings RMSE values of the AC parameters calculated taking into account specific ranges of Precipitable Water Vapor (PWV) for the entire atmospheric column (measured by SBPA radiosondes) and air temperature observed at the SBPA station (Table 1). The WRF model performs better under dry and cold conditions. It overcomes the other profile sources in the range of 2-3 g/cm² PWV. Under almost all moisture and temperature conditions, the profiles ACPC presented better results than the NCEP CFSv2 ones. All the different profiles presented minor errors in the situations of the lowest water vapor and air temperature. However, it is important to mention that the number of case days under these

conditions was less than under the other ranges. This is consistent with the research of Meng and Cheng (2018), which noticed the best global RMSEs for profiles under water vapor content lower than 1 g/cm². Furthermore, they indicated that the largest RMSEs occur when the water vapor is between 3 and 4 g/cm². Concerning the air temperature, our results suggest that errors in estimating the atmospheric parameters are higher on warmer days.

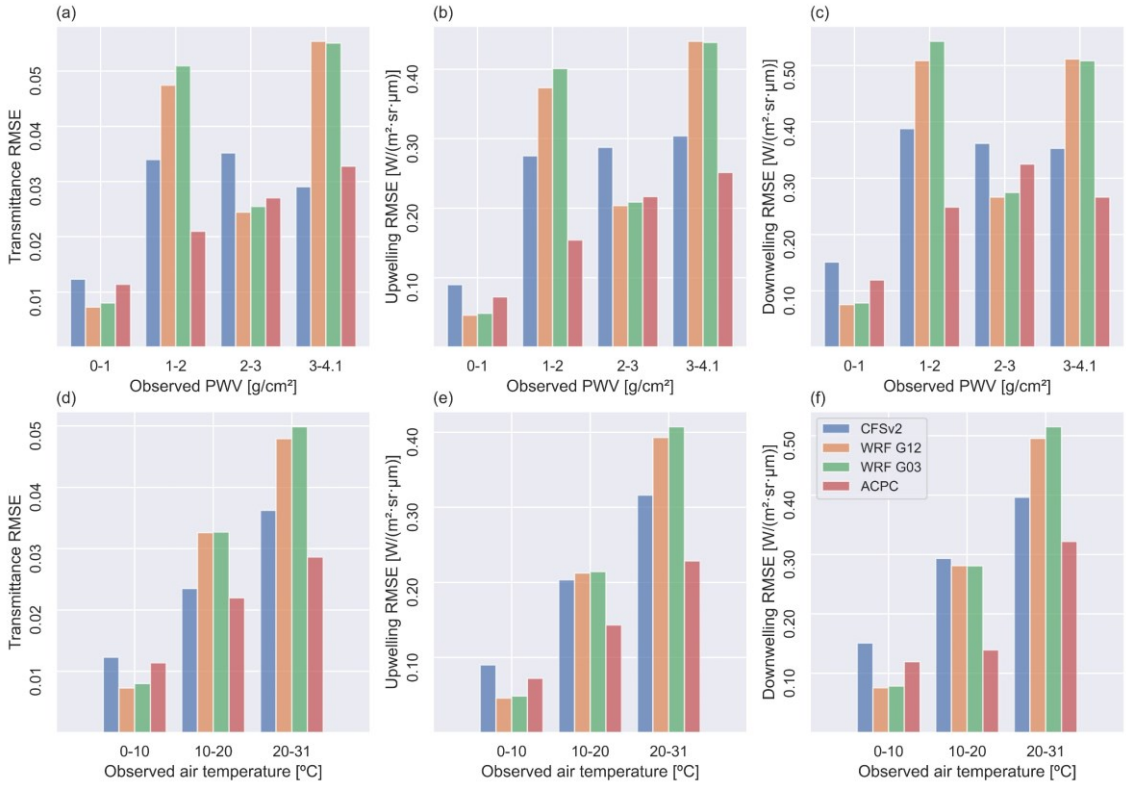

Fig. 6. Atmospheric parameters RMSE values calculated by specific ranges of observed Precipitable Water Vapor (PWV) (a-b) and air temperature (d-f).

3.2. Application to RTE-based LST retrieval

To further assess the different atmospheric profiles, the retrieved LSTs by RTE inversion with atmospheric parameters, Landsat 8 TIRS10 radiance, and $NDVI^{THM}$ emissivity were intercompared. Once more, the LST images that used SBPA profiles were assumed as reference data. Except for the atmospheric parameters calculated from the different profile sources, the other variables in Equation (11) were the same for each pixel of the scenes. Therefore, the differences in LST values that were retrieved with SBPA profiles and the other sources are due to the discrepancies among the profiles (Yang et al., 2020). Fig. 7 illustrates an example (case day 25) of the LST spatial distribution in the study area. Note that the hottest pixels are over the airstrip and adjacent buildings of the airport.

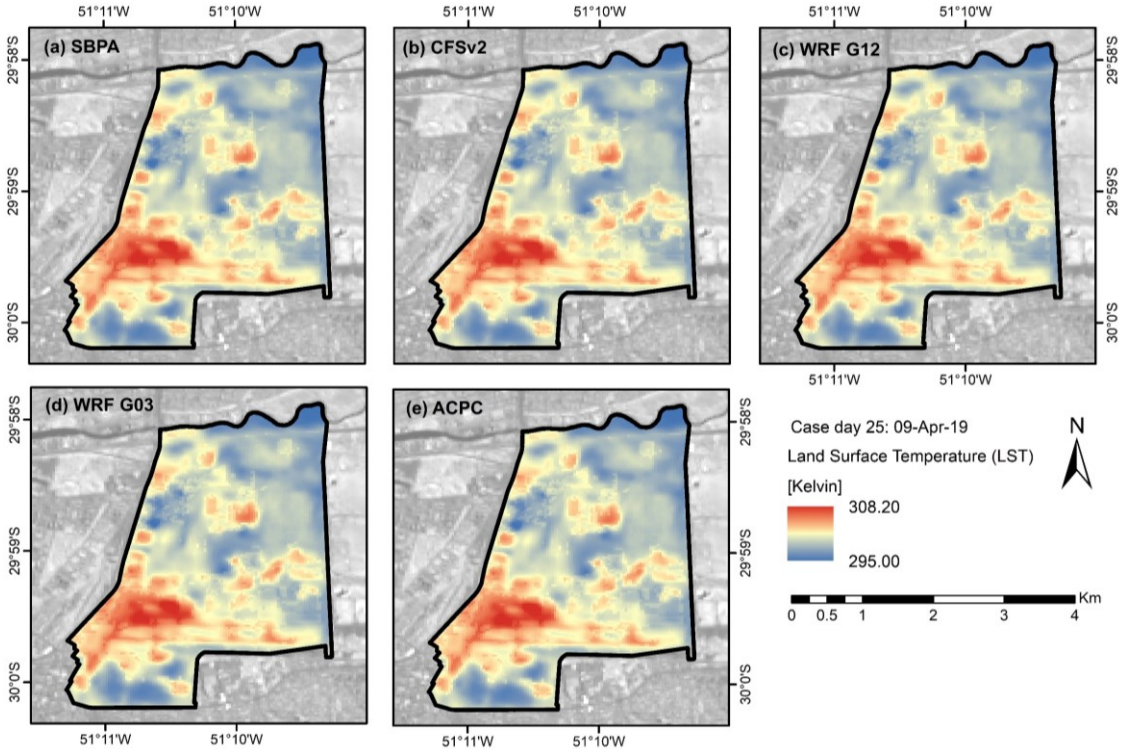

Fig. 7. LST images retrieved with atmospheric parameters from (a) SBPA, (b) CFSv2, (c) WRF G12, (d) WRF G03, and (e) ACPC, for the case day 25 (09-Apr-19).

Histograms of LST errors take in all the 10,184 pixels in the study area of the 27 case days are shown in Fig. 8. These represent the frequency distribution of the errors in the retrieval of LST using the different atmospheric profile sources. For all profiles, more than 50 % of the errors are of ± 1 K. Yang et al. (2020) also found most of LST differences in this range, using different reanalysis and satellite-derived profiles. The histograms in Fig. 8b and 8c indicate that WRF profiles tend to overestimate the LST. Whereas ACPC tends to underestimate it (Fig. 8d). Using WRF profiles, LST errors can reach more than 4 K, although in a very small number of cases. For ACPC and both WRF grids, the error range that occurs most often is between 0 and -1 K. The distribution of CFSv2 LST errors is more symmetrical than in the other profiles.

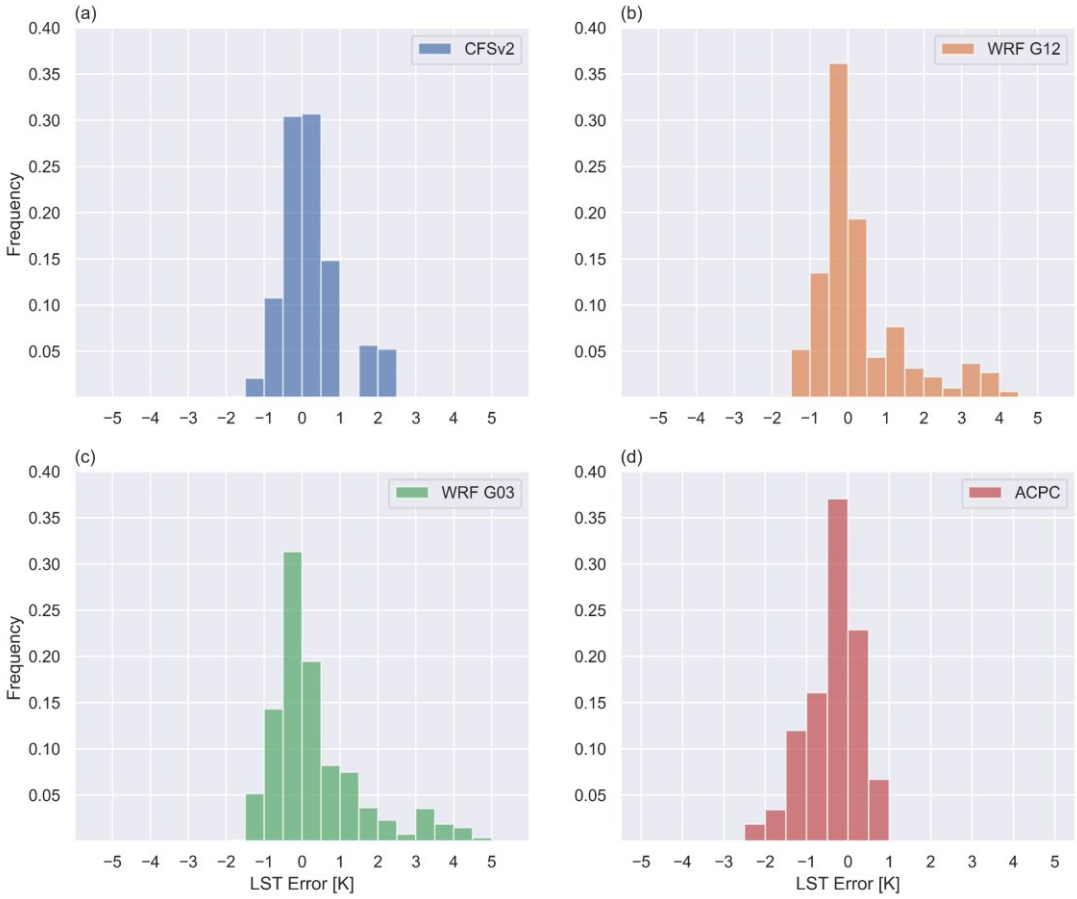

Fig. 8. Normalized histograms of the LST error using profiles from (a) CFSv2, (b) WRF G12, (c) WRF G03, and (d) ACPC.

Table 4 summarizes the metrics of the LST retrieval comparative analysis. Overall, the LST values of the four profile sources analyzed in this study were found in good agreement with the reference. All of them showed a very strong correlation and relatively low bias, MAE, and RMSE values. CFSv2, WRF G12, and WRF G03 presented an average positive bias and ACPC a negative one. This corroborates with the histogram analysis in Fig. 8. The mean error criteria (MAE and RMSE) indicate that the profiles with the best performance in the AC and RTE-based LST retrieval are, in descending order: CFSv2, ACPC, WRF G12, and WRF G03. The differences between CFSv2 and ACPC overall MAE and RMSE values were very small. The same for WRF G12 and G03.

Table 4. Statistical metrics of Land Surface Temperature (LST) retrieved using atmospheric parameters from different profile sources. The LST values calculated with SBPA parameters were considered as references.

		CFSv2	WRF G12	WRF G03	ACPC
LST [K]	R	0.99	0.99	0.99	0.99
	bias	0.23	0.32	0.36	-0.38
	MAE	0.54	0.79	0.81	0.56
	RMSE	0.55	0.79	0.82	0.56

Comparing with previous studies that evaluated the application of different atmospheric profiles in the LST retrieval, Meng and Cheng (2018) reported overall LST RMSE values higher than ours for eight different reanalysis profile sources analyzed around the globe. All their eight average RMSEs were largest than 1 K. The authors mention that ERA-Interim and MERRA (6-hour product) showed the lowest RMSEs, 1.09 K and 1.07 K respectively. They also indicate an average tendency to overestimate the LST, except for the JRA-55. In Yang et al. (2020) study, RMSEs were smaller than 0.6 K using profiles from ERA-Interim, MERRA2, NCEP GFS, and NCEP FNL, over Europe. Their worst accuracy (RMSE of 1 K) was obtained using MOD07 satellite-based profiles. Retrieving LST from three MODIS thermal bands, Pérez-Planells et al. (2015) showed RMSEs between 0.6 and 0.9 K using ACPC/NCEP and between 1.3 and 3 K for MOD07 profiles, depending on the band and the altitude of the study sites in Spain.

Fig. 9 displays the distribution of LST bias and RMSE along the case days. Fig. 9a evidences the ACPC and WRF settings average tendency of under and overestimate the LST, respectively. We found better RMSE values using CFSv2 in 11 of the 27 cases days, and in 8 using ACPC. Although the metrics of mean errors are greater for WRF profiles, in 11 case days the model improves the results of the reanalysis. Besides, the finer grid (G03) succeeded in downscaling the G12 11 times. The fact is that the largest errors were achieved when using the WRF model (e.g., case days 23, 19, and 17), and it contributes to the higher overall RMSE values. In general, the days with larger errors in atmospheric parameters (Fig. 5) are the days with larger LST RMSEs, as evinces the case 23. Conversely, in case 22, the errors in atmospheric parameters using ACPC are less than those using WRF profiles, but the highest LST RMSE on this day is with ACPC. Jiménez-Muñoz et al. (2010) advocate that cases like this may be explained due to compensation among AC parameters errors. For instance, a significant positive difference in transmittance and significant but negative differences in the atmospheric radiances. Fig. 10 endorses how errors in the atmospheric parameters propagate to the retrieved LST. The sensitivity analysis of Sekertekin and Bonafoni (2020a) reports that an uncertainty of ±0.01 in atmospheric transmittance impacts ±0.97 K on RTE-based LST retrieval. For upwelling and dowelling uncertainties of ±10 % led to ±1.82 K and ±0.07 K error in LST, respectively. Rosas et al. (2017) mentioned that an introduced uncertainty of 20 % in relative humidity profile can result in LST errors as large as 1.5 K in arid environments.

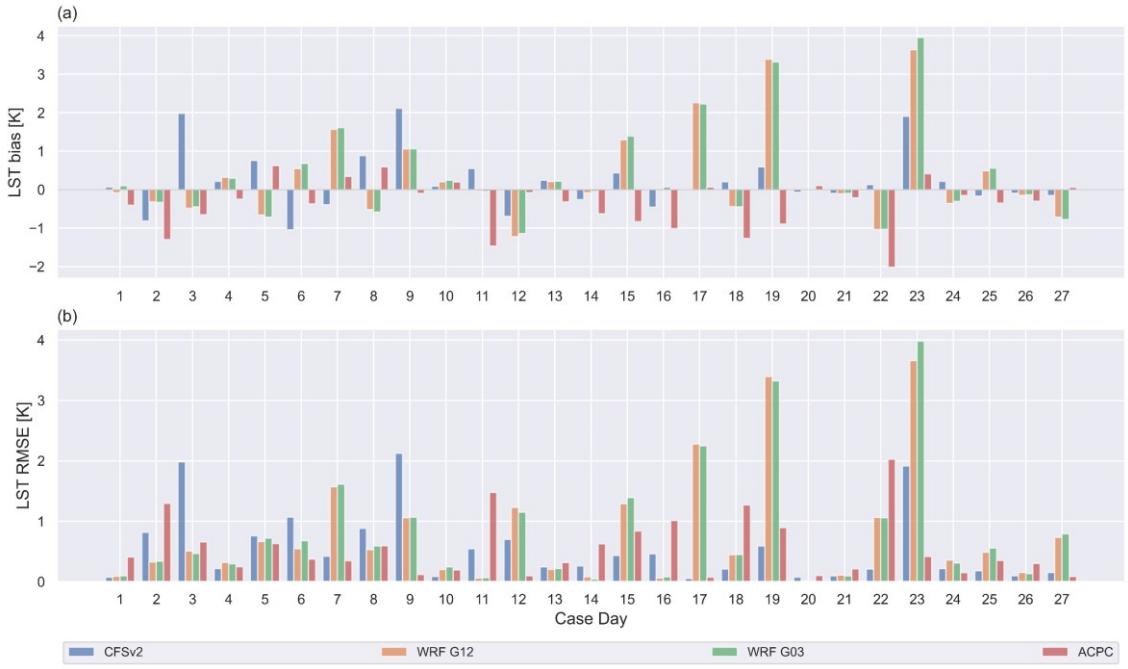

Fig. 9. LST (a) bias and (b) RMSE for each case day.

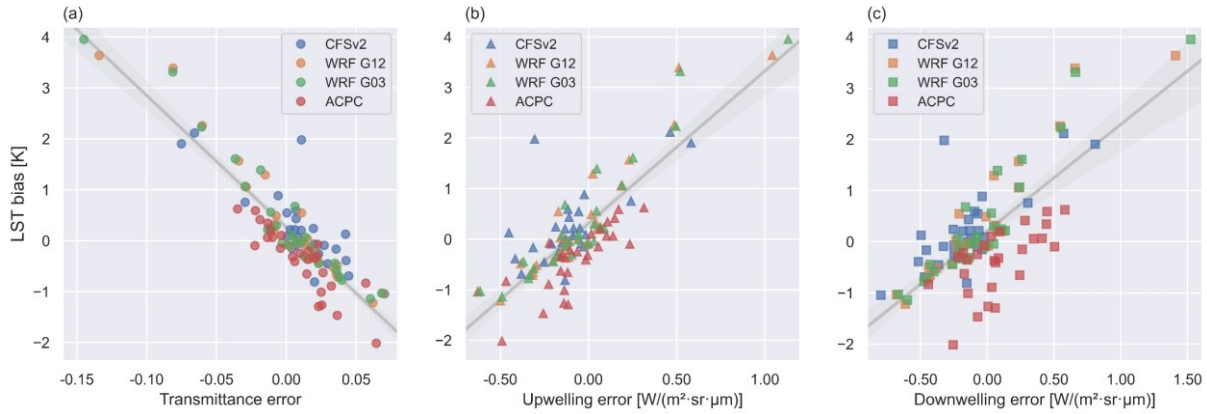

Fig. 10. Relation of daily LST bias with errors in (a) transmittance, (b) upwelling, and (c) downwelling radiances in each case day. The gray line represents the linear regression for all data.

In summary, the essay of downscaling the horizontal resolution of reanalysis data from 0.5º (~56 km) to 12 km and so to 3 km, aiming to reduce errors in the calculation of atmospheric parameters and hence in LST retrieval, did not perform as theoretically expected. With WRF simulations we also improved the vertical resolution in the lowest atmospheric levels. However, no significant improvement was found using the WRF profiles in the AC. In some cases, using a finer grid resolution profile even resulted in greater differences in atmospheric parameters and LST estimation. Rosas et al. (2017) reported that the higher vertical resolution of NCEP and ECMWF profiles in their study did not seem to play a significant role in the atmospheric correction. Even if naturally data with higher resolution tend to better represent the atmosphere parameters, it is not a strictly direct relationship (Meng

and Cheng, 2018; Yang et al., 2020). Furthermore, the ACPC that uses profiles with 1ºx1º (~111 km) horizontal resolution showed good results. Although these profiles have a coarser horizontal resolution, previous studies have been finding satisfactory results using the ACPC, even surpassing other methods (Coll et al., 2010; García-Santos et al., 2018; Jiménez-Muñoz et al., 2010; Käfer et al., 2020; Sekertekin, 2019; Skokovic et al., 2017; Tavares et al., 2019; Windahl and Beurs, 2016; Yu et al., 2014). It is important to note that in this study the WRF resulting profiles were extracted at 12 UTC to match with the available radiosonde data. Nevertheless, it could be set for the exact time of the satellite overpass. In ACPC and, in general, for reanalysis profiles, this time synchronization is done through linear interpolation. Which may not be the most appropriate strategy for sampling weather fronts and diurnal heating cycles (Barsi et al., 2005, 2003; Meng and Cheng, 2018).

4. Conclusions

Vertical atmospheric profiles are key inputs in the atmospheric correction for estimating LST using the RTE inversion single-channel approach. This study evaluated the use of the WRF numerical model to simulate high-resolution profiles improving horizontal, temporal, and vertical resolutions of NCEP CFSv2 reanalysis data. The profiles were incorporated in the MODTRAN RTM to compute the atmospheric correction parameters, which were then applied in the RTE to retrieve LST values from Landsat 8 TIRS10 data. We included in the comparison analysis: in situ radiosondes observations as ground truth (SBPA); vertical profiles from two grids of the WRF model with horizontal resolutions of 12 km (WRF G12) and 3 km (WRF G03); NCEP CFSv2 reanalysis data; and the wide applied ACPC web-tool. The assessment took into account 27 clear-sky Landsat 8 scenes over a radiosonde station in Southern Brazil.

The obtained results showed that for the three atmospheric parameters (atmospheric transmittance, upwelling, and downwelling radiances) the ACPC provided parameters in better agreement with those calculated using the radiosondes. The seconds-lowest uncertainties were using CFSv2 profiles. No significant statistical differences were found between the parameters from the two WRF grids. None of the profile sources outperformed in all case days analyzed. The overall metrics of WRF profiles were influenced by some cases with large errors. There is a tendency of overestimating the transmittance and underestimating the upwelling and the downwelling (except for ACPC). As a whole, the assessed profile sources better represent the atmosphere in dry and cold conditions. The RMSEs ranged between 0.03 and 0.04 for transmittance, 0.20 and 0.34 $W \cdot m^{-2} \cdot sr^{-1} \cdot \mu m^{-1}$ for upwelling radiance, and from 0.27 to 0.43 $W \cdot m^{-2} \cdot sr^{-1} \cdot \mu m^{-1}$ for downwelling radiance. Concerning retrieved LST values, using those calculated by SBPA profile as reference, CFSv2 had the best results. With an RMSE of 0.55 K, it was slightly accurate than ACPC (RMSE of 0.56 K). WRF G12 and G03 showed RMSE values of 0.79 and 0.82 K, respectively. Both WRF grids and CFSv2 generated a positive LST bias, while ACPC generated a negative one. On balance, all the profile sources presented relatively good results in estimating the LST.

From the above findings, our main conclusion is that there is no special need to increase the horizontal resolution of reanalysis profiles aiming at general RTE-based LST

retrieval. We recommend the use of NCEP CFSv2 profiles for these applications. Moreover, our results reinforce the ACPC validity and feasibility, which is free of charge. Even though the overall statistical metrics for WRF profiles were inferior, their results were satisfactory. Both in the estimation of atmospheric parameters and LST values. Despite some studies used the WRF model to simulate the skin temperature (Wang et al., 2021, 2020), to the best of our knowledge, this paper is the first effort applying the WRF model to aid the atmospheric correction of thermal remote sensing data. Its use showed potential and our findings encourage further validations. Our proposal joins the background for studies combing TIR satellite images and high-resolution NWP models.

Acknowledgments

The Landsat-8 data are courtesy of the US Geological Survey Earth Resources Observation and Science Center. The CFSv2 reanalysis data are provided by the National Centers for Environmental Prediction (NCEP), available at the Research Data Archive (RDA) – National Center for Atmospheric Research (NCAR). The radiosonde observations were obtained from the University of Wyoming website. This study was financed in part by the Coordenação de Aperfeiçoamento de Pessoal de Nível Superior – Brazil (CAPES), finance code 001. The anonymous reviewers are thanked for their valuable contributions. We are also grateful to Dr. Luis Morales-Salinas (University of Chile) and Dr. Dražen Skokovic (University of Valencia) for their support regarding the MODTRAN model.

References

Alghamdi, A.S., 2020. Evaluation of four reanalysis datasets against radiosonde over Southwest Asia. Atmosphere 11. https://doi.org/10.3390/ATMOS11040402

Alvares, C.A., Stape, J.L., Sentelhas, P.C., De Moraes Gonçalves, J.L., Sparovek, G., 2013. Köppen's climate classification map for Brazil. Meteorologische Zeitschrift 22, 711–728. https://doi.org/10.1127/0941-2948/2013/0507

Anderson, M.C., Allen, R.G., Morse, A., Kustas, W.P., 2012. Use of Landsat thermal imagery in monitoring evapotranspiration and managing water resources. Remote Sensing of Environment 122, 50–65. https://doi.org/10.1016/j.rse.2011.08.025

Anderson, M.C., Norman, J.M., Kustas, W.P., Houborg, R., Starks, P.J., Agam, N., 2008. A thermal-based remote sensing technique for routine mapping of land-surface carbon, water and energy fluxes from field to regional scales. Remote Sensing of Environment 112, 4227–4241. https://doi.org/10.1016/j.rse.2008.07.009

Anderson, M.C., Yang, Yang, Xue, J., Knipper, K.R., Yang, Yun, Gao, F., Hain, C.R., Kustas, W.P., Cawse-Nicholson, K., Hulley, G., Fisher, J.B., Alfieri, J.G., Meyers, T.P., Prueger, J., Baldocchi, D.D., Rey-Sanchez, C., 2021. Interoperability of ECOSTRESS and Landsat for mapping evapotranspiration time series at sub-field scales. Remote Sensing of Environment 252, 112189. https://doi.org/10.1016/j.rse.2020.112189

Aumann, H.H., Chahine, M.T., Gautier, C., Goldberg, M.D., Kalnay, E., McMillin, L.M., Revercomb, H., Rosenkranz, P.W., Smith, W.L., Staelin, D.H., Strow, L.L., Susskind, J., 2003. AIRS/AMSU/HSB on the aqua mission: design, science objectives, data products, and processing systems. IEEE Transactions on Geoscience and Remote Sensing 41, 253–264. https://doi.org/10.1109/TGRS.2002.808356

Barsi, J.A., Barker, J.L., Schott, J.R., 2003. An Atmospheric Correction Parameter Calculator for a single thermal band earth-sensing instrument, in: IGARSS 2003. 2003 IEEE International Geoscience and Remote Sensing Symposium. Proceedings (IEEE Cat. No.03CH37477). IEEE, pp. 3014–3016. https://doi.org/10.1109/IGARSS.2003.1294665

Barsi, J.A., Schott, J.R., Palluconi, F.D., Hook, S.J., 2005. Validation of a web-based atmospheric correction tool for single thermal band instruments, in: Butler, J.J. (Ed.), Earth Observing Systems X. p. 58820E. https://doi.org/10.1117/12.619990

Berk, A., Anderson, G.P., Acharya, P.K., Hoke, M.L., Chetwynd, J.H., Bernstein, L.S., Shettle, E.P., Matthew, M.W., Adler-Golden, S.M., 2003. MODTRAN4 Version 3 Revision 1 USER'S MANUAL.

Berk, A., Conforti, P., Kennett, R., Perkins, T., Hawes, F., van den Bosch, J., 2014. MODTRAN6: a major upgrade of the MODTRAN radiative transfer code, in: Velez-Reyes, M., Kruse, F.A. (Eds.), Workshop on Hyperspectral Image and Signal Processing, Evolution in Remote Sensing. p. 90880H. https://doi.org/10.1117/12.2050433

Borbas, E., Menzel, P., 2017. MODIS Atmosphere L2 Atmosphere Profile Product. https://doi.org/10.5067/MODIS/MOD07_L2.061

Candy, B., Saunders, R.W., Ghent, D., Bulgin, C.E., 2017. The Impact of Satellite-Derived Land Surface Temperatures on Numerical Weather Prediction Analyses and Forecasts. Journal of Geophysical Research: Atmospheres 122, 9783–9802. https://doi.org/10.1002/2016JD026417

Cao, B., Liu, Q., Du, Y., Roujean, J.L., Gastellu-Etchegorry, J.P., Trigo, I.F., Zhan, W., Yu, Y., Cheng, J., Jacob, F., Lagouarde, J.P., Bian, Z., Li, H., Hu, T., Xiao, Q., 2019. A review of earth surface thermal radiation directionality observing and modeling: Historical development, current status and perspectives. Remote Sensing of Environment 232, 111304. https://doi.org/10.1016/j.rse.2019.111304

Carlson, T.N., Ripley, D.A., 1997. On the relation between NDVI, fractional vegetation cover, and leaf area index. Remote Sensing of Environment 62, 241–252. https://doi.org/10.1016/S0034-4257(97)00104-1

Chai, T., Draxler, R.R., 2014. Root mean square error (RMSE) or mean absolute error (MAE)? – Arguments against avoiding RMSE in the literature. Geoscientific Model Development 7, 1247–1250. https://doi.org/10.5194/gmd-7-1247-2014

Chen, B., Liu, Z., 2016. Global water vapor variability and trend from the latest 36 year (1979 to 2014) data of ECMWF and NCEP reanalyses, radiosonde, GPS, and microwave satellite. Journal of Geophysical Research: Atmospheres 121, 11,442-11,462. https://doi.org/10.1002/2016JD024917

Chen, G., Iwasaki, T., Qin, H., Sha, W., 2014. Evaluation of the warm-season diurnal variability over East Asia in recent reanalyses JRA-55, ERA-Interim, NCEP CFSR, and NASA MERRA. Journal of Climate 27, 5517–5537. https://doi.org/10.1175/JCLI-D-14-00005.1

Chen, S.-H., Sun, W.-Y., 2002. A One-dimensional Time Dependent Cloud Model. Journal of the Meteorological Society of Japan. Ser. II 80, 99–118. https://doi.org/10.2151/jmsj.80.99

Coll, C., Caselles, V., Galve, J.M., Valor, E., Niclòs, R., Sánchez, J.M., Rivas, R., 2005. Ground measurements for the validation of land surface temperatures derived from AATSR and MODIS data. Remote Sensing of Environment 97, 288–300. https://doi.org/10.1016/j.rse.2005.05.007

Coll, C., Caselles, V., Valor, E., Niclòs, R., 2012. Comparison between different sources of atmospheric profiles for land surface temperature retrieval from single channel thermal infrared data. Remote Sensing of Environment 117, 199–210. https://doi.org/10.1016/j.rse.2011.09.018

Coll, C., Galve, J.M., Sanchez, J.M., Caselles, V., 2010. Validation of Landsat-7/ETM+ Thermal-Band Calibration and Atmospheric Correction With Ground-Based Measurements. IEEE Transactions on Geoscience and Remote Sensing 48, 547–555. https://doi.org/10.1109/TGRS.2009.2024934

Dee, D.P., Uppala, S.M., Simmons, A.J., Berrisford, P., Poli, P., Kobayashi, S., Andrae, U., Balmaseda, M.A., Balsamo, G., Bauer, P., Bechtold, P., Beljaars, A.C.M.M., van de Berg, L., Bidlot, J., Bormann, N., Delsol, C., Dragani, R., Fuentes, M., Geer, A.J., Haimberger, L., Healy, S.B., Hersbach, H., Hólm, E. V., Isaksen, L., Kållberg, P., Köhler, M., Matricardi, M., McNally, A.P., Monge-Sanz, B.M., Morcrette, J.-J., Park, B.-K., Peubey, C., de Rosnay, P., Tavolato, C., Thépaut, J.-N., Vitart, F., 2011. The ERA-Interim reanalysis: configuration and performance of the data assimilation system. Quarterly Journal of the Royal Meteorological Society 137, 553–597. https://doi.org/10.1002/qj.828

Diaz, L.R., Santos, D.C., Käfer, P.S., Iglesias, M.L., da Rocha, N.S., da Costa, S.T.L., Kaiser, E.A., Rolim, S.B.A., 2021. Reanalysis profile downscaling with WRF model and sensitivity to PBL parameterization schemes over a subtropical station. Journal of Atmospheric and Solar-Terrestrial Physics 222, 105724. https://doi.org/10.1016/j.jastp.2021.105724

Duan, S.-B., Li, Z.-L., Wang, C., Zhang, S., Tang, B.-H., Leng, P., Gao, M.-F., 2018. Land-surface temperature retrieval from Landsat 8 single-channel thermal infrared data in combination with NCEP reanalysis data and ASTER GED product. International Journal of Remote Sensing 40, 1763–1778. https://doi.org/10.1080/01431161.2018.1460513

Dudhia, J., 1989. Numerical Study of Convection Observed during the Winter Monsoon Experiment Using a Mesoscale Two-Dimensional Model. Journal of the Atmospheric Sciences 46, 3077–3107. https://doi.org/10.1175/1520-0469(1989)046<3077:NSOCOD>2.0.CO;2

Fekih, A., Mohamed, A., 2019. Evaluation of the WRF model on simulating the vertical structure and diurnal cycle of the atmospheric boundary layer over Bordj Badji Mokhtar (southwestern Algeria). Journal of King Saud University - Science 31, 602–611. https://doi.org/10.1016/j.jksus.2017.12.004

Galve, J.M., Sánchez, J.M., Coll, C., Villodre, J., 2018. A new single-band pixel-by-pixel atmospheric correction method to improve the accuracy in remote sensing estimates of LST. Application to landsat 7-ETM+. Remote Sensing 10. https://doi.org/10.3390/rs10060826

García-Díez, M., Fernández, J., Fita, L., Yagüe, C., 2013. Seasonal dependence of WRF model biases and sensitivity to PBL schemes over Europe. Quarterly Journal of the Royal Meteorological Society 139, 501–514. https://doi.org/10.1002/qj.1976

García-Santos, V., Cuxart, J., Martínez-Villagrasa, D., Jiménez, M.A., Simó, G., 2018. Comparison of three methods for estimating land surface temperature from Landsat 8-TIRS Sensor data. Remote Sensing 10, 1–13. https://doi.org/10.3390/rs10091450

Gemitzi, A., Dalampakis, P., Falalakis, G., 2021. International Journal of Applied Earth Observations and Geoinformation Detecting geothermal anomalies using Landsat 8 thermal infrared remotely sensed data. International Journal of Applied Earth Observations and Geoinformation 96, 102283. https://doi.org/10.1016/j.jag.2020.102283

Harod, R., Eswar, R., Bhattacharya, B.K., 2021. Effect of surface emissivity and retrieval algorithms on the accuracy of Land Surface Temperature retrieved from Landsat data. Remote Sensing Letters 12, 983–993. https://doi.org/10.1080/2150704X.2021.1957511

Hassanli, H., Rahimzadegan, M., 2019. Investigating extracted total precipitable water vapor from Weather Research and Forecasting (WRF) model and MODIS measurements. Journal of Atmospheric and Solar-Terrestrial Physics 193, 105060. https://doi.org/10.1016/j.jastp.2019.105060

Hersbach, H., Bell, B., Berrisford, P., Hirahara, S., Horányi, A., Muñoz-Sabater, J., Nicolas, J., Peubey, C., Radu, R., Schepers, D., Simmons, A., Soci, C., Abdalla, S., Abellan, X., Balsamo, G., Bechtold, P., Biavati, G., Bidlot, J., Bonavita, M., De Chiara, G., Dahlgren, P., Dee, D., Diamantakis, M., Dragani, R., Flemming, J., Forbes, R., Fuentes, M., Geer, A., Haimberger, L., Healy, S., Hogan, R.J., Hólm, E., Janisková, M., Keeley, S., Laloyaux, P., Lopez, P., Lupu, C., Radnoti, G., de Rosnay, P., Rozum, I., Vamborg, F., Villaume, S., Thépaut, J.N., 2020. The ERA5 global reanalysis. Quarterly Journal of the Royal Meteorological Society 1–51. https://doi.org/10.1002/qj.3803

Hong, S.-Y., Noh, Y., Dudhia, J., 2006. A New Vertical Diffusion Package with an Explicit Treatment of Entrainment Processes. Monthly Weather Review 134, 2318–2341. https://doi.org/10.1175/MWR3199.1

Hu, X., Ren, H., Tansey, K., Zheng, Y., Ghent, D., Liu, X., Yan, L., 2019. Agricultural drought monitoring using European Space Agency Sentinel 3A land surface temperature and normalized difference vegetation index imageries. Agricultural and Forest Meteorology 279, 107707. https://doi.org/10.1016/j.agrformet.2019.107707

Ihlen, V., Zanter, K., 2019. Landsat 8 (L8) Data Users Handbook, Version 5.0, LSDS-1574. Sioux Falls, South Dakota.

Janjić, Z.I., 1994. The Step-Mountain Eta Coordinate Model: Further Developments of the Convection, Viscous Sublayer, and Turbulence Closure Schemes. Monthly Weather Review 122, 927–945. https://doi.org/10.1175/1520-0493(1994)122<0927:TSMECM>2.0.CO;2

Jiménez, P.A., Dudhia, J., González-Rouco, J.F., Navarro, J., Montávez, J.P., García-Bustamante, E., 2012. A Revised Scheme for the WRF Surface Layer Formulation. Monthly Weather Review 140, 898–918. https://doi.org/10.1175/MWR-D-11-00056.1

Jiménez-Muñoz, J.C., Cristobal, J., Sobrino, J.A.J.A., Sòria, G., Ninyerola, M., Pons, X., Jimenez-Munoz, J.C., Cristobal, J., Sobrino, J.A.J.A., Soria, G., Ninyerola, M., Pons, X., Pons, X., 2009. Revision of the Single-Channel Algorithm for Land Surface Temperature Retrieval From Landsat Thermal-Infrared Data. IEEE Transactions on Geoscience and Remote Sensing 47, 339–349. https://doi.org/10.1109/TGRS.2008.2007125

Jiménez-Muñoz, J.C., Mattar, C., Sobrino, J.A., Malhi, Y., 2016. Digital thermal monitoring of the Amazon forest: an intercomparison of satellite and reanalysis products. International Journal of Digital Earth 9, 477–498. https://doi.org/10.1080/17538947.2015.1056559

Jiménez-Muñoz, J.C., Sobrino, J.A., Mattar, C., Franch, B., 2010. Atmospheric correction of optical imagery from MODIS and Reanalysis atmospheric products. Remote Sensing of Environment 114, 2195–2210. https://doi.org/10.1016/j.rse.2010.04.022

Käfer, P.S., Rolim, S.B.A., Diaz, L.R., Rocha, N.S. da, Iglesias, M.L., Rex, F.E., 2020. Comparative analysis of split-window and single-channel algorithms for land surface temperature retrieval of a pseudo-invariant target. Bulletin of Geodetic Sciences 26, 1–17. https://doi.org/10.1590/s1982-21702020000200008

Käfer, P.S.P.S., Rolim, S.B.A., Iglesias, M.L., da Rocha, N.S., Diaz, L.R., 2019. Land Surface Temperature Retrieval by LANDSAT 8 Thermal Band: Applications of Laboratory and Field Measurements. IEEE Journal of Selected Topics in Applied Earth Observations and Remote Sensing 12, 2332–2341. https://doi.org/10.1109/JSTARS.2019.2913822

Kalnay, E., Kanamitsu, M., Kistler, R., Collins, W., Deaven, D., Gandin, L., Iredell, M., Saha, S., White, G., Woollen, J., Zhu, Y., Leetmaa, A., Reynolds, R., Chelliah, M., Ebisuzaki, W., Higgins, W., Janowiak, J., Mo, K.C., Ropelewski, C., Wang, J., Jenne, R., Joseph, D., 1996. The NCEP/NCAR 40-Year Reanalysis Project. Bulletin of the American Meteorological Society 77, 437–471. https://doi.org/10.1175/1520-0477(1996)077<0437:TNYRP>2.0.CO;2

Kanamitsu, M., Ebisuzaki, W., Woollen, J., Yang, S.K., Hnilo, J.J., Fiorino, M., Potter, G.L., 2002. NCEP-DOE AMIP-II reanalysis (R-2). Bulletin of the American Meteorological Society 83, 1631-1643+1559. https://doi.org/10.1175/BAMS-83-11-1631(2002)083<1631:NAR>2.3.CO;2

Kioutsioukis, I., de Meij, A., Jakobs, H., Katragkou, E., Vinuesa, J., Kazantzidis, A., 2016. High resolution WRF ensemble forecasting for irrigation: Multi-variable evaluation. Atmospheric Research 167, 156–174. https://doi.org/10.1016/j.atmosres.2015.07.015

Kobayashi, S., Ota, Y., Harada, Y., Ebita, A., Moriya, M., Onoda, H., Onogi, K., Kamahori, H., Kobayashi, C., Endo, H., Miyaoka, K., Takahashi, K., Onada, H., Onogi, K., Kamahori, H., Kobayashi, C., Endo, H., Miyaoka, K., Takahashi, K., 2015. The JRA-55 Reanalysis: General Specifications and Basic Characteristics. Journal of the Meteorological Society of Japan. Ser. II 93, 5–48. https://doi.org/10.2151/jmsj.2015-001

Lee, H., Won, J.S., Park, W., 2020. An atmospheric correction using high resolution numericalweather prediction models for satellite-borne single-channel mid-wavelength and thermal infrared imaging sensors. Remote Sensing 12. https://doi.org/10.3390/rs12050853

Li, H., Liu, Q., Du, Y., Jiang, J., Wang, H., 2013. Evaluation of the NCEP and MODIS Atmospheric Products for Single Channel Land Surface Temperature Retrieval With Ground Measurements: A

Case Study of HJ-1B IRS Data. IEEE Journal of Selected Topics in Applied Earth Observations and Remote Sensing 6, 1399–1408. https://doi.org/10.1109/JSTARS.2013.2255118

Li, S., Jiang, G.-M., 2018. Land Surface Temperature Retrieval From Landsat-8 Data With the Generalized Split-Window Algorithm. IEEE Access 6, 18149–18162. https://doi.org/10.1109/ACCESS.2018.2818741

Li, Z.-L., Tang, B.-H., Wu, H., Ren, H., Yan, G., Wan, Z., Trigo, I.F., Sobrino, J.A., 2013. Satellite-derived land surface temperature: Current status and perspectives. Remote Sensing of Environment 131, 14–37. https://doi.org/10.1016/j.rse.2012.12.008

Li, Z.L., Wu, H., Wang, N., Qiu, S., Sobrino, J.A., Wan, Z., Tang, B.H., Yan, G., 2013. Land surface emissivity retrieval from satellite data. International Journal of Remote Sensing 34, 3084–3127. https://doi.org/10.1080/01431161.2012.716540

Lin, C., Chen, D., Yang, K., Ou, T., 2018. Impact of model resolution on simulating the water vapor transport through the central Himalayas: implication for models' wet bias over the Tibetan Plateau. Climate Dynamics 51, 3195–3207. https://doi.org/10.1007/s00382-018-4074-x

Maffei, C., Alfieri, S.M., Menenti, M., 2018. Relating spatiotemporal patterns of forest fires burned area and duration to diurnal land surface temperature anomalies. Remote Sensing 10. https://doi.org/10.3390/rs10111777

Magarreiro, C., Gouveia, C., Barroso, C., Trigo, I., 2019. Modelling of Wine Production Using Land Surface Temperature and FAPAR—The Case of the Douro Wine Region. Remote Sensing 11, 604. https://doi.org/10.3390/rs11060604

Malakar, N.K., Hulley, G.C., Hook, S.J., Laraby, K., Cook, M., Schott, J.R., 2018. An Operational Land Surface Temperature Product for Landsat Thermal Data: Methodology and Validation. IEEE Transactions on Geoscience and Remote Sensing 56, 5717–5735. https://doi.org/10.1109/TGRS.2018.2824828

Mattar, C., Durán-Alarcón, C., Jiménez-Muñoz, J.C., Santamaría-Artigas, A., Olivera-Guerra, L., Sobrino, J.A., 2015. Global Atmospheric Profiles from Reanalysis Information (GAPRI): a new database for earth surface temperature retrieval. International Journal of Remote Sensing 36, 5045–5060. https://doi.org/10.1080/01431161.2015.1054965

Matzenauer, R., Radin, B., Almeida, I.R. de, 2011. Atlas Climático do Rio Grande do Sul. Porto Alegre.

Meng, X., Cheng, J., 2018. Evaluating Eight Global Reanalysis Products for Atmospheric Correction of Thermal Infrared Sensor—Application to Landsat 8 TIRS10 Data. Remote Sensing 10, 474. https://doi.org/10.3390/rs10030474

Mira, M., Olioso, A., Rivalland, V., Courault, D., Marloie, O., Guillevic, P., 2014. Quantifying uncertainties in land surface temperature due to atmospheric correction: Application to Landsat-7 data over a Mediterranean agricultural region, in: 2014 IEEE Geoscience and Remote Sensing Symposium. IEEE, pp. 2375–2378. https://doi.org/10.1109/IGARSS.2014.6946949

Mlawer, E.J., Taubman, S.J., Brown, P.D., Iacono, M.J., Clough, S.A., 1997. Radiative transfer for inhomogeneous atmospheres: RRTM, a validated correlated-k model for the longwave. Journal of Geophysical Research: Atmospheres 102, 16663–16682. https://doi.org/10.1029/97JD00237

Mohan, M., Sati, A.P., 2016. WRF model performance analysis for a suite of simulation design. Atmospheric Research 169, 280–291. https://doi.org/10.1016/j.atmosres.2015.10.013

Montaner-Fernández, D., Morales-Salinas, L., Rodriguez, J.S., Cárdenas-Jirón, L., Huete, A., Fuentes-Jaque, G., Pérez-Martínez, W., Cabezas, J., 2020. Spatio-temporal variation of the urban heat island in Santiago, Chile during summers 2005–2017. Remote Sensing 12, 1–19. https://doi.org/10.3390/rs12203345

Moya-Álvarez, A.S., Estevan, R., Kumar, S., Flores Rojas, J.L., Ticse, J.J., Martínez-Castro, D., Silva, Y., 2020. Influence of PBL parameterization schemes in WRF_ARW model on short - range precipitation's forecasts in the complex orography of Peruvian Central Andes. Atmospheric Research 233, 104708. https://doi.org/10.1016/j.atmosres.2019.104708

Mylonas, M.P., Douvis, K.C., Polychroni, I.D., Politi, N., Nastos, P.T., 2019. Analysis of a Mediterranean Tropical-Like Cyclone. Sensitivity to WRF Parameterizations and Horizontal Resolution. Atmosphere 10, 425. https://doi.org/10.3390/atmos10080425

NCEP, National Weather Service, NOAA, U.S. Department of Commerce, 2000. NCEP FNL Operational Model Global Tropospheric Analyses, continuing from July 1999. Research Data Archive at the National Center for Atmospheric Research, Computational and Information Systems Laboratory. https://doi.org/10.5065/D6M043C6

Oltra-Carrió, R., Sobrino, J.A., Franch, B., Nerry, F., 2012. Land surface emissivity retrieval from airborne sensor over urban areas. Remote Sensing of Environment 123, 298–305. https://doi.org/10.1016/j.rse.2012.03.007

Onwukwe, C., Jackson, P.L., 2020. Meteorological downscaling with wrf model, version 4.0, and comparative evaluation of planetary boundary layer schemes over a complex coastal airshed. Journal of Applied Meteorology and Climatology 59, 1295–1319. https://doi.org/10.1175/JAMC-D-19-0212.1

Pavlidou, E., van der Meijde, M., van der Werff, H., Hecker, C., 2019. Time series analysis of land surface temperatures in 20 earthquake casesworldwide. Remote Sensing 11. https://doi.org/10.3390/rs11010061

Pérez-Jordán, G., Castro-Almazán, J.A., Muñoz-Tuñón, C., Codina, B., Vernin, J., 2015. Forecasting the precipitable water vapour content: validation for astronomical observatories using radiosoundings. Monthly Notices of the Royal Astronomical Society 452, 1992–2003. https://doi.org/10.1093/mnras/stv1394

Pérez-Planells, L., García-Santos, V., Caselles, V., 2015. Comparing different profiles to characterize the atmosphere for three MODIS TIR bands. Atmospheric Research 161–162, 108–115. https://doi.org/10.1016/j.atmosres.2015.04.001

Porto Alegre City Hall, 2016. Neighborhood Law No. 12.112/16. Brazil.

Powers, J.G., Klemp, J.B., Skamarock, W.C., Davis, C.A., Dudhia, J., Gill, D.O., Coen, J.L., Gochis, D.J., Ahmadov, R., Peckham, S.E., Grell, G.A., Michalakes, J., Trahan, S., Benjamin, S.G., Alexander, C.R., Dimego, G.J., Wang, W., Schwartz, C.S., Romine, G.S., Liu, Z., Snyder, C., Chen, F., Barlage, M.J., Yu, W., Duda, M.G., 2017. The Weather Research and Forecasting

Model: Overview, System Efforts, and Future Directions. Bulletin of the American Meteorological Society 98, 1717–1737. https://doi.org/10.1175/BAMS-D-15-00308.1

Price, J.C., 1983. Estimating surface temperatures from satellite thermal infrared data—A simple formulation for the atmospheric effect. Remote Sensing of Environment 13, 353–361. https://doi.org/10.1016/0034-4257(83)90036-6

Rienecker, M.M., Suarez, M.J., Gelaro, R., Todling, R., Bacmeister, J., Liu, E., Bosilovich, M.G., Schubert, S.D., Takacs, L., Kim, G.K., Bloom, S., Chen, J., Collins, D., Conaty, A., Da Silva, A., Gu, W., Joiner, J., Koster, R.D., Lucchesi, R., Molod, A., Owens, T., Pawson, S., Pegion, P., Redder, C.R., Reichle, R., Robertson, F.R., Ruddick, A.G., Sienkiewicz, M., Woollen, J., 2011. MERRA: NASA's modern-era retrospective analysis for research and applications. Journal of Climate 24, 3624–3648. https://doi.org/10.1175/JCLI-D-11-00015.1

Rocha, N.S. da, Käfer, P.S., Skokovic, D., Veeck, G., Diaz, L.R., Kaiser, E.A., Carvalho, C.M., Cruz, R.C., Sobrino, J.A., Roberti, D.R., Rolim, S.B.A., 2020. The Influence of Land Surface Temperature in Evapotranspiration Estimated by the S-SEBI Model. Atmosphere 11, 1059. https://doi.org/10.3390/atmos11101059

Rosas, J., Houborg, R., McCabe, M.F., 2017. Sensitivity of Landsat 8 Surface Temperature Estimates to Atmospheric Profile Data: A Study Using MODTRAN in Dryland Irrigated Systems. Remote Sensing 9, 988. https://doi.org/10.3390/rs9100988

Roy, D.P., Wulder, M.A., Loveland, T.R., C.E., W., Allen, R.G., Anderson, M.C., Helder, D., Irons, J.R., Johnson, D.M., Kennedy, R., Scambos, T.A., Schaaf, C.B., Schott, J.R., Sheng, Y., Vermote, E.F., Belward, A.S., Bindschadler, R., Cohen, W.B., Gao, F., Hipple, J.D., Hostert, P., Huntington, J., Justice, C.O., Kilic, A., Kovalskyy, V., Lee, Z.P., Lymburner, L., Masek, J.G., McCorkel, J., Shuai, Y., Trezza, R., Vogelmann, J., Wynne, R.H., Zhu, Z., 2014. Landsat-8: Science and product vision for terrestrial global change research. Remote Sensing of Environment 145, 154–172. https://doi.org/10.1016/j.rse.2014.02.001

Saha, S., Moorthi, S., Wu, X., Wang, J., Nadiga, S., Tripp, P., Behringer, D., Hou, Y.-T., Chuang, H., Iredell, M., Ek, M., Meng, J., Yang, R., Mendez, M.P., van den Dool, H., Zhang, Q., Wang, W., Chen, M., Becker, E., 2014. The NCEP Climate Forecast System Version 2. Journal of Climate 27, 2185–2208. https://doi.org/10.1175/JCLI-D-12-00823.1

Santos, D.C., Nascimento, E.D.L., 2016. Numerical Simulations of the South American Low Level Jet in Two Episodes of MCSs: Sensitivity to PBL and Convective Parameterization Schemes. Advances in Meteorology 2016, 1–18. https://doi.org/10.1155/2016/2812978

Sekertekin, A., 2019. Validation of Physical Radiative Transfer Equation-Based Land Surface Temperature Using Landsat 8 Satellite Imagery and SURFRAD in-situ Measurements. Journal of Atmospheric and Solar-Terrestrial Physics 196, 105161. https://doi.org/10.1016/j.jastp.2019.105161

Sekertekin, A., Bonafoni, S., 2020a. Land surface temperature retrieval from Landsat 5, 7, and 8 over rural areas: Assessment of different retrieval algorithms and emissivity models and toolbox implementation. Remote Sensing 12. https://doi.org/10.3390/rs12020294

Sekertekin, A., Bonafoni, S., 2020b. Sensitivity analysis and validation of daytime and nighttime land surface temperature retrievals from landsat 8 using different algorithms and emissivity models. Remote Sensing 12. https://doi.org/10.3390/RS12172776

Singh, N., Chatterjee, R.S., Kumar, D., Panigrahi, D.C., Mujawdiya, R., 2020. Retrieval of precise land surface temperature from ASTER night-time thermal infrared data by split window algorithm for improved coal fire detection in Jharia Coalfield, India. Geocarto International 1–18. https://doi.org/10.1080/10106049.2020.1753820

Skamarock, W.C., Klemp, J.B., Dudhia, J., Gill, D.O., Zhiquan, L., Berner, J., Wang, W., Powers, J.G., Duda, M.G., Barker, D.M., Huang, X.-Y., 2019. A Description of the Advanced Research WRF Model Version 4, NCAR Technical Note NCAR/TN-475+STR. Boulder, Colorado. https://doi.org/10.5065/1dfh-6p97

Skokovic, D., Sobrino, J.A., Jimenez-Munoz, J.C., 2017. Vicarious Calibration of the Landsat 7 Thermal Infrared Band and LST Algorithm Validation of the ETM+ Instrument Using Three Global Atmospheric Profiles. IEEE Transactions on Geoscience and Remote Sensing 55, 1804–1811. https://doi.org/10.1109/TGRS.2016.2633810

Sobrino, J., Raissouni, N., Li, Z.-L., 2001. A Comparative Study of Land Surface Emissivity Retrieval from NOAA Data. Remote Sensing of Environment 75, 256–266. https://doi.org/10.1016/S0034-4257(00)00171-1

Sobrino, J.A., Del Frate, F., Drusch, M., Jiménez-Muñoz, J.C., Manunta, P., Regan, A., 2016. Review of thermal infrared applications and requirements for future high-resolution sensors. IEEE Transactions on Geoscience and Remote Sensing 54, 2963–2972. https://doi.org/10.1109/TGRS.2015.2509179

Sobrino, J.A., Jiménez-Muñoz, J.C., Paolini, L., 2004. Land surface temperature retrieval from LANDSAT TM 5. Remote Sensing of Environment 90, 434–440. https://doi.org/10.1016/j.rse.2004.02.003

Sobrino, J.A., Jimenez-Munoz, J.C., Soria, G., Romaguera, M., Guanter, L., Moreno, J., Plaza, A., Martinez, P., 2008. Land Surface Emissivity Retrieval From Different VNIR and TIR Sensors. IEEE Transactions on Geoscience and Remote Sensing 46, 316–327. https://doi.org/10.1109/TGRS.2007.904834

Sobrino, J.A., Raissouni, N., 2000. Toward remote sensing methods for land cover dynamic monitoring: Application to Morocco. International Journal of Remote Sensing 21, 353–366. https://doi.org/10.1080/014311600210876

Stensrud, D.J., 2007. Parameterization Schemes, Parameterization Schemes: Keys to Understanding Numerical Weather Prediction Models. Cambridge University Press, Cambridge. https://doi.org/10.1017/CBO9780511812590

Tang, H., Li, Z.-L., 2014. Quantitative Remote Sensing in Thermal Infrared, Quantitative Remote Sensing in Thermal Infrared, Springer Remote Sensing/Photogrammetry. Springer Berlin Heidelberg, Berlin, Heidelberg. https://doi.org/10.1007/978-3-642-42027-6

Tardy, B., Rivalland, V., Huc, M., Hagolle, O., Marcq, S., Boulet, G., 2016. A Software Tool for Atmospheric Correction and Surface Temperature Estimation of Landsat Infrared Thermal Data. Remote Sensing 8, 696. https://doi.org/10.3390/rs8090696

Tavares, M.H., Cunha, A.H.F., Motta-Marques, D., Ruhoff, A.L., Cavalcanti, J.R., Fragoso, C.R., Bravo, J.M., Munar, A.M., Fan, F.M., Rodrigues, L.H.R., 2019. Comparison of methods to estimate lake-surface-water temperature using landsat 7 ETM+ and MODIS imagery: Case study of a large shallow subtropical lake in Southern Brazil. Water (Switzerland) 11, 1–21. https://doi.org/10.3390/w11010168

Tavares, M.H., Cunha, A.H.F., Motta-Marques, D., Ruhoff, A.L., Fragoso, C.R., Munar, A.M., Bonnet, M.P., 2020. Derivation of consistent, continuous daily river temperature data series by combining remote sensing and water temperature models. Remote Sensing of Environment 241, 111721. https://doi.org/10.1016/j.rse.2020.111721

Taylor, K.E., 2001. Summarizing multiple aspects of model performance in a single diagram. Journal of Geophysical Research: Atmospheres 106, 7183–7192. https://doi.org/10.1029/2000JD900719

Tewari, M., Chen, F., Wang, W., Dudhia, J., LeMone, M.A., Mitchell, K., Ek, M., Gayno, G., Wegiel, J., Cuenca, R.H., 2004. Implementation and verification of the unified noah land surface model in the WRF model. Bulletin of the American Meteorological Society 2165–2170. https://doi.org/10.1007/s11269-013-0452-7

Tonooka, H., 2001. An atmospheric correction algorithm for thermal infrared multispectral data over land-a water-vapor scaling method. IEEE Transactions on Geoscience and Remote Sensing 39, 682–692. https://doi.org/10.1109/36.911125

Valor, E., Caselles, V., 1996. Mapping land surface emissivity from NDVI: Application to European, African, and South American areas. Remote Sensing of Environment 57, 167–184. https://doi.org/10.1016/0034-4257(96)00039-9

Van de Griend, A.A., Owe, M., 1993. On the relationship between thermal emissivity and the normalized difference vegetation index for natural surfaces. International Journal of Remote Sensing 14, 1119–1131. https://doi.org/10.1080/01431169308904400

Vanhellemont, Q., 2020a. Automated water surface temperature retrieval from Landsat 8/TIRS. Remote Sensing of Environment 237, 111518. https://doi.org/10.1016/j.rse.2019.111518

Vanhellemont, Q., 2020b. Combined land surface emissivity and temperature estimation from Landsat 8 OLI and TIRS. ISPRS Journal of Photogrammetry and Remote Sensing 166, 390–402. https://doi.org/10.1016/j.isprsjprs.2020.06.007

Wang, D., Liu, Y., Yu, T., Zhang, Y., Liu, Q., Chen, X., Zhan, Y., 2020. A Method of Using WRF-Simulated Surface Temperature to Estimate Daily Evapotranspiration. Journal of Applied Meteorology and Climatology 59, 901–914. https://doi.org/10.1175/JAMC-D-19-0287.1

Wang, D., Yu, T., Liu, Y., Gu, X., Mi, X., Shi, S., Ma, M., Chen, X., Zhang, Y., Liu, Q., Mumtaz, F., Zhan, Y., 2021. Estimating daily actual evapotranspiration at a landsat-like scale utilizing simulated and remote sensing surface temperature. Remote Sensing 13, 1–19. https://doi.org/10.3390/rs13020225

Wang, W., Bruyere, C., Michael, D., Duhia, J., Dave, G., Kavulich, M., Werner, K., Chen, M., Hui-Chuan, L., Michalakes, J., Rizvi, S., 2019. Advanced Research WRF (ARW) Version 4 Modeling System User´s Guide.

Wee, T.K., Kuo, Y.H., Lee, D. kyou, Liu, Z., Wang, W., Chen, S.Y., 2012. Two overlooked biases of the advanced research wrf (arw) model in geopotential height and temperature. Monthly Weather Review 140, 3907–3918. https://doi.org/10.1175/MWR-D-12-00045.1

Willmott, C.J., Matsuura, K., 2005. Advantages of the mean absolute error (MAE) over the root mean square error (RMSE) in assessing average model performance. Climate Research 30, 79–82. https://doi.org/10.3354/cr030079

Windahl, E., Beurs, K. de, 2016. An intercomparison of Landsat land surface temperature retrieval methods under variable atmospheric conditions using in situ skin temperature. International Journal of Applied Earth Observation and Geoinformation 51, 11–27. https://doi.org/10.1016/j.jag.2016.04.003

WMO, 2016. The Global Observing System for Climate: Implementation Needs, GCOS - 200.

Wu, P., Yin, Z., Zeng, C., Duan, S.-B., Gottsche, F.-M., Li, X., Ma, X., Yang, H., Shen, H., 2021. Spatially Continuous and High-Resolution Land Surface Temperature Product Generation: A Review of Reconstruction and Spatiotemporal Fusion Techniques. IEEE Geoscience and Remote Sensing Magazine 2, 0–0. https://doi.org/10.1109/MGRS.2021.3050782

Xie, B., Fung, J.C.H., Chan, A., Lau, A., 2012. Evaluation of nonlocal and local planetary boundary layer schemes in the WRF model. Journal of Geophysical Research Atmospheres 117, 1–26. https://doi.org/10.1029/2011JD017080

Yang, J., Duan, S.B., Zhang, X., Wu, P., Huang, C., Leng, P., Gao, M., 2020. Evaluation of seven atmospheric profiles from reanalysis and satellite-derived products: Implication for single-channel land surface temperature retrieval. Remote Sensing 12. https://doi.org/10.3390/rs12050791

Yu, X., Guo, X., Wu, Z., 2014. Land Surface Temperature Retrieval from Landsat 8 TIRS—Comparison between Radiative Transfer Equation-Based Method, Split Window Algorithm and Single Channel Method. Remote Sensing 6, 9829–9852. https://doi.org/10.3390/rs6109829

4 CONCLUSÕES

Perfis atmosféricos verticais são *inputs* essenciais para a correção atmosférica de dados de sensoriamento remoto no infravermelho termal e estimativa de temperatura da superfície (LST). O presente trabalho propôs-se a analisar a utilização do modelo WRF na geração de perfis atmosféricos de alta resolução, refinando dados globais de reanálise, e a aplicação dos mesmos na correção atmosférica/cálculo de LST, por meio da inversão direta da Equação de Transferência Radiativa (RTE).

Nesse processo, avaliar a performance do modelo na simulação dos perfis verticais propriamente ditos é de grande importância, uma vez que erros nessa modelagem podem propagar-se para a aplicação final, neste caso a recuperação de LST. Sendo assim, a primeira parte dessa dissertação buscou examinar o desempenho do WRF na representação da distribuição vertical, na coluna atmosférica, da razão de mistura do vapor de água (q) e da temperatura potencial (θ). Uma série de simulações foram realizadas utilizando dados de reanálise do NCEP CFSv2 como condições iniciais e configurando o modelo com duas grades aninhadas com resoluções horizontais de 12 km (G12) e 3 km (G03). Adicionalmente, devido a importância da camada limite (PBL) na concentração do vapor de água atmosférico, o principal responsável pela perturbação do sinal no sensoriamento remoto no TIR, foi realizada uma análise de sensibilidade do modelo a dois esquemas de parametrização de PBL: YSU (não-local) e MYJ (local). A validação dos perfis de q e θ deu-se utilizando radiossondagens locais, lançadas no Aeroporto Internacional de Porto Alegre (SBPA), no sul do Brasil.

Os resultados indicaram que o modelo WRF simulou de maneira satisfatória os perfis verticais de razão de mistura do vapor de água e temperatura potencial. A comparação estatística desses com dados *in situ* resultou em altos valores de coeficiente de correlação, vieses significativamente pequenos e valores relativamente baixos de RMSE e erro médio absoluto (*Mean Absolute Error* – MAE). Todavia, não foram encontradas diferenças significativas nas métricas gerais dos perfis do WRF ao variar a resolução horizontal da grade do modelo de 12 para 3 km e também com relação aos perfis extraídos diretamente dos dados de reanálise NCEP CFSv2. Em alguns casos, o aumento da resolução resultou, até mesmo, em

maiores discrepâncias na comparação com os perfis observados. Esses resultados indicam que o aumento da resolução horizontal não melhorou significativamente a qualidade do perfil atmosférico simulado. Portanto, é possível concluir que não há uma necessidade especial de aumentar a resolução espacial para aplicações que visem uma caracterização geral de atmosferas locais. Uma vez que, nesses casos, isso acrescenta um custo computacional significativo sem uma melhora expressiva dos perfis simulados. Recomenda-se o uso de um espaçamento de grade menor que 3 km apenas para estudos locais específicos em que haja a necessidade de tal resolução. E ainda, devido a constatação do menor impacto da resolução horizontal na simulação do perfil atmosférico, esse estudo encoraja uma atenção para o aumento da resolução vertical em trabalhos futuros.

A análise de sensibilidade, aos esquemas de parametrização de PBL YSU e MYJ, revelou que nenhum dos esquemas destacou-se amplamente em todos os casos analisados. A configuração com melhor resultado variou ao longo das datas estudadas. Essa constatação enfatiza que a definição do esquema de parametrização de PBL mais apropriado é dependente de condições sazonais e meteorológicas e da variável que está sendo analisada. Ademais, as medidas estatísticas obtidas com os diferentes esquemas de parametrização são análogas. Desse modo, esse trabalho mostra que a escolha entre um desses esquemas de PBL, um local e outro não-local, pode não ser fundamental para uma representação satisfatória de perfis atmosféricos de temperatura e vapor de água. Mais estudos são necessários para corroborar essa hipótese.

A segunda parte da presente dissertação refere-se à aplicação dos perfis simulados utilizando o WRF na correção atmosférica para estimativa de LST. Para tal, os perfis foram incorporados, como dados de entrada, no modelo de transferência radiativa MODTRAN – que possibilita o cálculo dos três parâmetros de correção atmosférica: transmitância, *upwelling* e *downwelling*. Esses parâmetros foram então inseridos na RTE para a recuperação de valores de LST, a partir de dados de radiância da banda 10 do sensor Landsat 8 TIRS. Foram incluídos na análise comparativa: radiossondagens *in situ* (SBPA), perfis simulados pelo WRF nas grades G12 e G03 (optou-se pela utilização do esquema YSU nesta etapa), perfis extraídos diretamente da reanálise NCEP CSFv2 e, ainda, a amplamente utilizada Calculadora de Parâmetros de Correção Atmosférica da NASA (ACPC). As

fontes de perfis atmosféricos foram avaliadas por meio da comparação tanto dos parâmetros atmosféricos como da LST – essa calculada para os pixels de 27 cenas Landsat 8 TIRS10 sobre a estação SBPA e em condições de céu claro. Os valores assumidos como verdade de campo foram aqueles calculados utilizando os perfis de radiossonda observados.

Os resultados obtidos mostraram que a ACPC, quando comparada com as demais fontes de perfis verticais, forneceu parâmetros atmosféricos em melhor concordância com aqueles calculados a partir das radiossondagens. A segunda menor diferença geral foi encontrada utilizando os perfis CFSv2. Ainda não foram identificadas diferenças significativas entre os parâmetros obtidos a partir dos perfis das duas grades do WRF. Nenhuma mesma fonte de perfis atmosféricos superou as demais em todos os dias estudados. As métricas gerais dos perfis WRF foram influenciadas por alguns casos que apresentaram notadamente grandes erros. Foi identificada uma tendência de superestimar a transmitância e subestimar as radiações *upwelling* e *downwelling* (com exceção da ACPC). Além disso, as fontes de perfis analisadas, como um todo, descrevem melhor a coluna atmosférica em condições frias e de baixa umidade. Os RMSEs encontrados nessa pesquisa variaram entre: 0,03 e 0,04 para transmitância; 0,20 e 0,34 $W \cdot m^{-2} \cdot sr^{-1} \cdot \mu m^{-1}$ para *upwelling;* 0,27 e 0,43 $W \cdot m^{-2} \cdot sr^{-1} \cdot \mu m^{-1}$ para *downwelling*.

No que diz respeito aos valores calculados de LST, a utilização dos perfis de reanálise NCEP CFSv2 mostrou os melhores resultados, em relação a referência (LST calculadas com os perfis SBPA). Esses dados com um RMSE de 0,55 K foram ligeiramente mais acurados que os recuperados utilizando a ACPC (RMSE de 0,56 K). Já o uso dos perfis WRF G12 e G03 resultaram em valores de RMSE de 0,79 e 0,82 K, respectivamente. Ambas as grades do WRF e a reanálise CFSv2 geraram um viés positivo para a LST, enquanto a calculadora da NASA apresentou viés geral negativo. Em suma, todas as fontes de perfis atmosféricos analisadas apresentaram bons resultados na estimativa da LST.

Entretanto, a hipótese de melhorar a resolução horizontal dos dados de reanálise de 0,5º (~56 km) para 12 km e então para 3 km, com o objetivo de reduzir os erros no cálculo dos parâmetros atmosféricos e, por consequência, na estimativa de LST – não ocorreu como o pressuposto. Com as simulações no WRF, também foi incrementada a resolução vertical dos perfis nos níveis mais próximos da superfície.

No entanto, nenhuma melhora significativa foi demonstrada utilizando os perfis gerados pelo WRF na correção atmosférica no TIR. Em alguns casos, o uso de um perfil de uma grade mais refinada, inclusive, resultou em maiores incertezas nos parâmetros atmosféricos e na LST, assim como constatado na avaliação direta dos perfis verticais. Além disso, a ACPC, que utiliza perfis de reanálise com resolução horizontal de 1º (~111 km), apresentou resultados bastante satisfatórios. Por outro lado, é importante notar que, neste estudo, os perfis resultantes das simulações com o modelo WRF foram extraídos para as 12 UTC, para corresponder com os dados de radiossondagem disponíveis. Esses poderiam, todavia, ser extraídos para o horário exato de passagem do satélite sobre a área de estudo. Na ACPC e, em geral, para perfis de reanálise, essa sincronização é feita por meio de uma interpolação linear – o que pode não ser a estratégia mais adequada para amostrar frentes meteorológicas e ciclos diários de aquecimento.

Diante do exposto, a principal conclusão dessa dissertação é de que não há uma necessidade particular de refinar a resolução horizontal dos perfis de reanálise visando a recuperação de LST, baseada no método de canal único de inversão da RTE. Os achados dessa pesquisa recomendam o uso de perfis de reanálise NCEP CFSv2 para essa aplicação. Também, se reforça a utilidade da já estabelecida ACPC, que é acessível e gratuita. Embora as métricas estatísticas gerais obtidas com os perfis simulados pelo WRF tenham sido inferiores, seus resultados são considerados satisfatórios. Tanto na simulação dos perfis verticais propriamente ditos, como para o cálculo dos parâmetros de correção atmosférica e da LST. Esse fato estimula a realização de estudos adicionais, testando diferentes configurações do modelo com, por exemplo, outros domínios (com variadas resoluções horizontais e verticais) e outras opções de parametrizações físicas. Ainda sobre trabalhos futuros, sugere-se a validação com dados de campo de temperatura de superfície, além da inclusão de outras áreas de estudo, para que as conclusões aqui estabelecidas possam ser extrapoladas e corroboradas para diferentes ambientes e atmosferas.

Por fim, essa pesquisa contribui para o *background* de estudos que se utilizam de modelos numéricos atmosféricos para realizar a correção atmosférica de dados de sensoriamento remoto termais – inovando ao constituir, até onde se sabe, a primeira tentativa de se testar o modelo WRF para essa aplicação.

FINANCIAMENTO

O presente trabalho foi realizado com apoio da Coordenação de Aperfeiçoamento de Pessoal de Nível Superior – Brasil (CAPES) – Código de Financiamento 001, através de bolsa de mestrado.

REFERÊNCIAS

ALGHAMDI, A. S. Evaluation of Four Reanalysis Datasets against Radiosonde over Southwest Asia. **Atmosphere**, v. 11, n. 4, p. 402, 2020. Disponível em: https://www.mdpi.com/2073-4433/11/4/402.

ANDERSON, M. C. *et al.* A thermal-based remote sensing technique for routine mapping of land-surface carbon, water and energy fluxes from field to regional scales. **Remote Sensing of Environment**, v. 112, n. 12, p. 4227–4241, 2008. Disponível em: http://dx.doi.org/10.1016/j.rse.2008.07.009.

ANDERSON, M. C. *et al.* Use of Landsat thermal imagery in monitoring evapotranspiration and managing water resources. **Remote Sensing of Environment**, v. 122, p. 50–65, 2012. Disponível em: http://dx.doi.org/10.1016/j.rse.2011.08.025.

ARABI ALIABAD, F.; ZARE, M.; GHAFARIAN MALAMIRI, H. Comparison of the accuracy of daytime land surface temperature retrieval methods using Landsat 8 images in arid regions. **Infrared Physics & Technology**, v. 115, n. October 2020, p. 103692, 2021. Disponível em: https://doi.org/10.1016/j.infrared.2021.103692.

AUMANN, H. H. *et al.* AIRS/AMSU/HSB on the aqua mission: design, science objectives, data products, and processing systems. **IEEE Transactions on Geoscience and Remote Sensing**, v. 41, n. 2, p. 253–264, 2003. Disponível em: http://ieeexplore.ieee.org/document/1196043/.

BANKS, R. F. *et al.* Sensitivity of boundary-layer variables to PBL schemes in the WRF model based on surface meteorological observations, lidar, and radiosondes during the HygrA-CD campaign. **Atmospheric Research**, v. 176–177, p. 185–201, 2016. Disponível em: http://dx.doi.org/10.1016/j.atmosres.2016.02.024.

BARSI, J. *et al.* Landsat-8 Thermal Infrared Sensor (TIRS) Vicarious Radiometric Calibration. **Remote Sensing**, v. 6, n. 11, p. 11607–11626, 2014. Disponível em: http://www.mdpi.com/2072-4292/6/11/11607.

BARSI, J. A. *et al.* Validation of a web-based atmospheric correction tool for single thermal band instruments. *In*: 2005. (J. J. Butler, Org.) **Earth Observing Systems X**. 2005. p. 58820E. Disponível em: http://proceedings.spiedigitallibrary.org/proceeding.aspx?doi=10.1117/12.619990.

BARSI, J. A.; BARKER, J. L.; SCHOTT, J. R. An Atmospheric Correction Parameter Calculator for a single thermal band earth-sensing instrument. *In*: 2003. **IGARSS 2003. 2003 IEEE International Geoscience and Remote Sensing Symposium. Proceedings (IEEE Cat. No.03CH37477)**. IEEE, 2003. p. 3014–3016. Disponível em: http://ieeexplore.ieee.org/document/1294665/.

BECKER, F.; LI, Z.-L. Surface temperature and emissivity at various scales: definition, measurement and related problems. **Remote Sensing Reviews**, v. 12, n. 3–4, p. 225–253, 1995.

BECKER, F.; LI, Z. L. Towards a local split window method over land surfaces. **International Journal of Remote Sensing**, v. 11, n. 3, p. 369–393, 1990.

BERK, A. *et al.* MODTRAN6: a major upgrade of the MODTRAN radiative transfer code. *In*: 2014. (M. Velez-Reyes & F. A. Kruse, Org.) **Workshop on Hyperspectral Image and Signal Processing, Evolution in Remote Sensing**. 2014. p. 90880H. Disponível em: http://proceedings.spiedigitallibrary.org/proceeding.aspx?doi=10.1117/12.2050433.

BOADH, R. *et al.* Sensitivity of PBL schemes of the WRF-ARW model in simulating the boundary layer flow parameters for their application to air pollution dispersion modeling over a tropical station. **Atmósfera**, v. 29, n. 1, p. 61–81, 2016. Disponível em: http://www.revistascca.unam.mx/atm/index.php/atm/article/view/ATM.2016.29.01.05/46533.

BORBAS, E.; MENZEL, P. **MODIS Atmosphere L2 Atmosphere Profile Product**. NASA MODIS Adaptive Processing System, Goddard Space Flight Center, 2017. Disponível em: https://modis-atmos.gsfc.nasa.gov/products/atm-profile.

CAO, B. *et al.* A review of earth surface thermal radiation directionality observing and modeling: Historical development, current status and perspectives. **Remote Sensing of Environment**, v. 232, n. May, p. 111304, 2019. Disponível em: https://doi.org/10.1016/j.rse.2019.111304.

CARLSON, T. N.; RIPLEY, D. A. On the relation between NDVI, fractional vegetation cover, and leaf area index. **Remote Sensing of Environment**, v. 62, n. 3, p. 241–252, 1997. Disponível em: https://linkinghub.elsevier.com/retrieve/pii/S0034425797001041.

CHAOUCH, N. *et al.* Sensitivity of the meteorological model WRF-ARW to planetary boundary layer schemes during fog conditions in a coastal arid region. **Atmospheric Research**, v. 187, p. 106–127, 2017. Disponível em: http://dx.doi.org/10.1016/j.atmosres.2016.12.009.

CHAUMAT, L. *et al.* **4A/OP Reference Documentation**. Versão NOV-3049-NT-1178-v4.3. NOVELTIS, LMD/CNRS, CNES, 2012. Disponível em: https://4aop.noveltis.com/sites/4aop.noveltis.loc/files/NOV-3049-NT-1178v4.3.pdf.

CHEN, Y. *et al.* Algorithm Development for Land Surface Temperature Retrieval: Application to Chinese Gaofen-5 Data. **Remote Sensing**, v. 9, n. 2, p. 161, 2017. Disponível em: http://www.mdpi.com/2072-4292/9/2/161.

CHEN, G. *et al.* Evaluation of the warm-season diurnal variability over East Asia in recent reanalyses JRA-55, ERA-Interim, NCEP CFSR, and NASA MERRA. **Journal of Climate**, v. 27, n. 14, p. 5517–5537, 2014.

CHEN, B.; LIU, Z. Global water vapor variability and trend from the latest 36 year (1979 to 2014) data of ECMWF and NCEP reanalyses, radiosonde, GPS, and microwave satellite. **Journal of Geophysical Research: Atmospheres**, v. 121, n. 19, p. 11,442-11,462, 2016. Disponível em: http://www.nature.com/articles/175238c0.

COHEN, A. E. *et al.* A review of planetary boundary layer parameterization schemes and their sensitivity in simulating southeastern U.S. cold season severe weather environments. **Weather and Forecasting**, v. 30, n. 3, p. 591–612, 2015.

COLL, C. *et al.* Comparison between different sources of atmospheric profiles for land surface temperature retrieval from single channel thermal infrared data. **Remote Sensing of Environment**, v. 117, p. 199–210, 2012. Disponível em: http://dx.doi.org/10.1016/j.rse.2011.09.018.

COLL, C. *et al.* Ground measurements for the validation of land surface temperatures derived from AATSR and MODIS data. **Remote Sensing of Environment**, v. 97, n. 3, p. 288–300, 2005. Disponível em: https://linkinghub.elsevier.com/retrieve/pii/S0034425705001562.

CONIGLIO, M. C. *et al.* Verification of convection-allowing WRF model forecasts of the planetary boundary layer using sounding observations. **Weather and Forecasting**, v. 28, n. 3, p. 842–862, 2013.

CRISTÓBAL, J. *et al.* An Improved Single-Channel Method to Retrieve Land Surface Temperature from the Landsat-8 Thermal Band. **Remote Sensing**, v. 10, n. 3, p. 431, 2018. Disponível em: http://www.mdpi.com/2072-4292/10/3/431.

CUCHIARA, G. C. *et al.* Intercomparison of planetary boundary layer parameterization and its impacts on surface ozone concentration in the WRF/Chem model for a case study in houston/texas. **Atmospheric Environment**, v. 96, p. 175–185, 2014.

DASH, P. *et al.* Land surface temperature and emissivity estimation from passive sensor data: Theory and practice-current trends. **International Journal of Remote Sensing**, v. 23, n. 13, p. 2563–2594, 2002. Disponível em: https://www.tandfonline.com/doi/full/10.1080/01431160110115041.

DASH, P. *et al.* Separating surface emissivity and temperature using two-channel spectral indices and emissivity composites and comparison with a vegetation fraction method. **Remote Sensing of Environment**, v. 96, n. 1, p. 1–17, 2005. Disponível em: https://linkinghub.elsevier.com/retrieve/pii/S0034425705000234.

DE LANGE, A. *et al.* Sensitivity of meteorological variables on planetary boundary layer parameterization schemes in the WRF-ARW model. **Atmospheric Research**, v. 247, 2021.

DE ROSA, B.; DI GIROLAMO, P.; SUMMA, D. Temperature and water vapour measurements in the framework of the Network for the Detection of Atmospheric Composition Change (NDACC). **Atmospheric Measurement Techniques**, v. 13, n. 2, p. 405–427, 2020.

DEE, D. P. *et al.* The ERA-Interim reanalysis: configuration and performance of the data assimilation system. **Quarterly Journal of the Royal Meteorological Society**, v. 137, n. 656, p. 553–597, 2011. Disponível em: http://doi.wiley.com/10.1002/qj.828.

DIAO, M. *et al.* Validation of AIRS/AMSU-A water vapor and temperature data with in situ aircraft observations from the surface to UT/LS from 87°N-67°S. **Journal of Geophysical Research: Atmospheres**, v. 118, n. 12, p. 6816–6836, 2013. Disponível em: http://doi.wiley.com/10.1002/jgrd.50483.

DIAZ, L. R. *et al.* Reanalysis profile downscaling with WRF model and sensitivity to PBL parameterization schemes over a subtropical station. **Journal of Atmospheric and Solar-Terrestrial Physics**, v. 222, p. 105724, 2021. Disponível em: https://linkinghub.elsevier.com/retrieve/pii/S1364682621001784.

DU, C. *et al.* A Practical Split-Window Algorithm for Estimating Land Surface Temperature from Landsat 8 Data. **Remote Sensing**, v. 7, n. 1, p. 647–665, 2015. Disponível em: http://www.mdpi.com/2072-4292/7/1/647.

DUAN, S.-B. *et al.* Land-surface temperature retrieval from Landsat 8 single-channel thermal infrared data in combination with NCEP reanalysis data and ASTER GED product. **International Journal of Remote Sensing**, v. 40, n. 5–6, p. 1763–1778, 2018. Disponível em: https://www.tandfonline.com/doi/full/10.1080/01431161.2018.1460513.

EMDE, C. *et al.* The libRadtran software package for radiative transfer calculations (version 2.0.1). **Geoscientific Model Development**, v. 9, n. 5, p. 1647–1672, 2016. Disponível em: https://gmd.copernicus.org/articles/9/1647/2016/.

EVANS, J. P.; EKSTRÖM, M.; JI, F. Evaluating the performance of a WRF physics ensemble over South-East Australia. **Climate Dynamics**, v. 39, n. 6, p. 1241–1258, 2012.

FEKIH, A.; MOHAMED, A. Evaluation of the WRF model on simulating the vertical structure and diurnal cycle of the atmospheric boundary layer over Bordj Badji Mokhtar (southwestern Algeria). **Journal of King Saud University - Science**, v. 31, n. 4, p. 602–611, 2019. Disponível em: https://doi.org/10.1016/j.jksus.2017.12.004.

FILIOGLOU, M. *et al.* Profiling water vapor mixing ratios in Finland by means of a Raman lidar, a satellite and a model. **Atmospheric Measurement Techniques**, v. 10, n. 11, p. 4303–4316, 2017.

GALVE, J. M. *et al.* A new single-band pixel-by-pixel atmospheric correction method to improve the accuracy in remote sensing estimates of LST. Application to landsat 7-ETM+. **Remote Sensing**, v. 10, n. 6, 2018.

GARCÍA-DÍEZ, M. *et al.* Seasonal dependence of WRF model biases and sensitivity to PBL schemes over Europe. **Quarterly Journal of the Royal Meteorological Society**, v. 139, n. 671, p. 501–514, 2013.

GARCÍA-SANTOS, V. *et al.* Comparison of three methods for estimating land surface temperature from Landsat 8-TIRS Sensor data. **Remote Sensing**, v. 10, n. 9, p. 1–13, 2018.

GARRATT, J. Review: the atmospheric boundary layer. **Earth-Science Reviews**, v. 37, n. 1–2, p. 89–134, 1994. Disponível em: https://linkinghub.elsevier.com/retrieve/pii/0012825294900264.

GEMITZI, A.; DALAMPAKIS, P.; FALALAKIS, G. Detecting geothermal anomalies using Landsat 8 thermal infrared remotely sensed data. **International Journal of Applied Earth Observation and Geoinformation**, v. 96, n. December 2020, p. 102283, 2021. Disponível em: https://doi.org/10.1016/j.jag.2020.102283.

GERACE, A.; MONTANARO, M. Derivation and validation of the stray light correction algorithm for the thermal infrared sensor onboard Landsat 8. **Remote Sensing of Environment**, v. 191, p. 246–257, 2017. Disponível em: https://linkinghub.elsevier.com/retrieve/pii/S0034425717300421.

GILLESPIE, A. *et al.* A temperature and emissivity separation algorithm for Advanced Spaceborne Thermal Emission and Reflection Radiometer (ASTER) images. **IEEE Transactions on Geoscience and Remote Sensing**, v. 36, n. 4, p. 1113–1126, 1998. Disponível em: http://ieeexplore.ieee.org/document/700995/.

GONZÁLEZ-ALONSO DE LINAJE, N.; MATTAR, C.; BORVARÁN, D. Quantifying the wind energy potential differences using different WRF initial conditions on Mediterranean coast of Chile. **Energy**, v. 188, p. 116027, 2019. Disponível em: https://linkinghub.elsevier.com/retrieve/pii/S0360544219317219.

GUO, J. *et al.* Evaluation of land surface temperature retrieval from landsat 8/TIRS images before and after stray light correction using the SURFRAD dataset. **Remote Sensing**, v. 12, n. 6, 2020.

HARIPRASAD, K. B. R. R. *et al.* Numerical simulation and intercomparison of boundary layer structure with different PBL schemes in WRF using experimental

observations at a tropical site. **Atmospheric Research**, v. 145–146, p. 27–44, 2014. Disponível em: http://dx.doi.org/10.1016/j.atmosres.2014.03.023.

HASSANLI, H.; RAHIMZADEGAN, M. Investigating extracted total precipitable water vapor from Weather Research and Forecasting (WRF) model and MODIS measurements. **Journal of Atmospheric and Solar-Terrestrial Physics**, v. 193, n. May, p. 105060, 2019. Disponível em: https://doi.org/10.1016/j.jastp.2019.105060.

HERSBACH, H. *et al.* The ERA5 global reanalysis. **Quarterly Journal of the Royal Meteorological Society**, n. March, p. 1–51, 2020.

HIDALGO GARCÍA, D.; ARCO DÍAZ, J. Spatial and Multi-Temporal Analysis of Land Surface Temperature through Landsat 8 Images: Comparison of Algorithms in a Highly Polluted City (Granada). **Remote Sensing**, v. 13, n. 5, p. 1012, 2021. Disponível em: https://www.mdpi.com/2072-4292/13/5/1012.

HOLT, T.; RAMAN, S. A review and comparative evaluation of multilevel boundary layer parameterizations for first-order and turbulent kinetic energy closure schemes. **Reviews of Geophysics**, v. 26, n. 4, p. 761–780, 1988. Disponível em: http://doi.wiley.com/10.1029/RG026i004p00761.

HONG, S.-Y.; NOH, Y.; DUDHIA, J. A New Vertical Diffusion Package with an Explicit Treatment of Entrainment Processes. **Monthly Weather Review**, v. 134, n. 9, p. 2318–2341, 2006. Disponível em: http://journals.ametsoc.org/doi/abs/10.1175/MWR3199.1.

HONG, S.-Y.; PAN, H.-L. Nonlocal Boundary Layer Vertical Diffusion in a Medium-Range Forecast Model. **Monthly Weather Review**, v. 124, n. 10, p. 2322–2339, 1996. Disponível em: http://journals.ametsoc.org/doi/abs/10.1175/1520-0493%281996%29124%3C2322%3ANBLVDI%3E2.0.CO%3B2.

HU, X.-M.; NIELSEN-GAMMON, J. W.; ZHANG, F. Evaluation of Three Planetary Boundary Layer Schemes in the WRF Model. **Journal of Applied Meteorology and Climatology**, v. 49, n. 9, p. 1831–1844, 2010. Disponível em: http://journals.ametsoc.org/doi/abs/10.1175/2010JAMC2432.1.

IHLEN, V.; ZANTER, K. **Landsat 8 (L8) Data Users HandbookVersion 5.0, LSDS-1574**. Sioux Falls, South Dakota, 2019. Disponível em: https://www.usgs.gov/media/files/landsat-8-data-users-handbook. .

JANJIĆ, Z. I. The Step-Mountain Eta Coordinate Model: Further Developments of the Convection, Viscous Sublayer, and Turbulence Closure Schemes. **Monthly Weather Review**, v. 122, n. 5, p. 927–945, 1994. Disponível em: http://journals.ametsoc.org/doi/abs/10.1175/1520-0493%281994%29122%3C0927%3ATSMECM%3E2.0.CO%3B2.

JENSEN, J. R. **Sensoriamento Remoto do Ambiente: Uma Perspectiva em Recursos Terrestres**. Tradução: José Carlos Neves Epiphanio *et al.* 2. ed. São José dos Campos: Parêntese, 2009.

JIA, W.; ZHANG, X. The role of the planetary boundary layer parameterization schemes on the meteorological and aerosol pollution simulations: A review. **Atmospheric Research**, v. 239, n. October 2019, p. 104890, 2020. Disponível em: https://doi.org/10.1016/j.atmosres.2020.104890.

JIMÉNEZ-MUÑOZ, J. C. *et al.* A generalized single-channel method for retrieving land surface temperature from remote sensing data. **Journal of Geophysical Research: Atmospheres**, v. 108, n. D22, p. 2003JD003480, 2003. Disponível em: http://doi.wiley.com/10.1029/2003JD003480.

JIMÉNEZ-MUÑOZ, J. C. *et al.* Atmospheric correction of optical imagery from MODIS and Reanalysis atmospheric products. **Remote Sensing of Environment**, v. 114, n. 10, p. 2195–2210, 2010. Disponível em: http://dx.doi.org/10.1016/j.rse.2010.04.022.

JIMÉNEZ-MUÑOZ, J. C. *et al.* Land Surface Temperature Retrieval Methods From Landsat-8 Thermal Infrared Sensor Data. **IEEE Geoscience and Remote Sensing Letters**, v. 11, n. 10, p. 1840–1843, 2014. Disponível em: http://ieeexplore.ieee.org/xpl/articleDetails.jsp?arnumber=6784508.

JIMÉNEZ-MUÑOZ, J. C. *et al.* Revision of the Single-Channel Algorithm for Land Surface Temperature Retrieval From Landsat Thermal-Infrared Data. **IEEE Transactions on Geoscience and Remote Sensing**, v. 47, n. 1, p. 339–349, 2009. Disponível em: http://ieeexplore.ieee.org/document/4689350/.

KÄFER, P. S. *et al.* Assessment of single-channel algorithms for land surface temperature retrieval at two southern Brazil sites. **Journal of Applied Remote Sensing**, v. 14, n. 01, p. 1, 2020a. Disponível em: https://www.spiedigitallibrary.org/journals/journal-of-applied-remote-sensing/volume-14/issue-01/016507/Assessment-of-single-channel-algorithms-for-land-surface-temperature-retrieval/10.1117/1.JRS.14.016507.full.

KÄFER, P. S. *et al.* COMPARATIVE ANALYSIS OF SPLIT-WINDOW AND SINGLE-CHANNEL ALGORITHMS FOR LAND SURFACE TEMPERATURE RETRIEVAL OF A PSEUDO-INVARIANT TARGET. **Bulletin of Geodetic Sciences**, v. 26, n. 2, p. 1–17, 2020b. Disponível em: http://www.scielo.br/scielo.php?script=sci_arttext&pid=S1982-21702020000200204&tlng=en.

KÄFER, P. S. *et al.* Land Surface Temperature Retrieval by LANDSAT 8 Thermal Band: Applications of Laboratory and Field Measurements. **IEEE Journal of Selected Topics in Applied Earth Observations and Remote Sensing**, v. 12, n. 7, p. 2332–2341, 2019. Disponível em: https://ieeexplore.ieee.org/document/8720054/.

KALNAY, E. *et al.* The NCEP/NCAR 40-Year Reanalysis Project. **Bulletin of the American Meteorological Society**, v. 77, n. 3, p. 437–471, 1996. Disponível em: http://journals.ametsoc.org/doi/abs/10.1175/1520-0477%281996%29077%3C0437%3ATNYRP%3E2.0.CO%3B2.

KANAMITSU, M. *et al.* NCEP-DOE AMIP-II reanalysis (R-2). **Bulletin of the American Meteorological Society**, v. 83, n. 11, p. 1631-1643+1559, 2002.

KHANAL, S.; FULTON, J.; SHEARER, S. An overview of current and potential applications of thermal remote sensing in precision agriculture. **Computers and Electronics in Agriculture**, v. 139, p. 22–32, 2017. Disponível em: http://dx.doi.org/10.1016/j.compag.2017.05.001.

KIOUTSIOUKIS, I. *et al.* High resolution WRF ensemble forecasting for irrigation: Multi-variable evaluation. **Atmospheric Research**, v. 167, p. 156–174, 2016. Disponível em: http://dx.doi.org/10.1016/j.atmosres.2015.07.015.

KOBAYASHI, S. *et al.* The JRA-55 Reanalysis: General Specifications and Basic Characteristics. **Journal of the Meteorological Society of Japan. Ser. II**, v. 93, n. 1, p. 5–48, 2015. Disponível em: https://www.jstage.jst.go.jp/article/jmsj/93/1/93_2015-001/_article.

KOTCHENOVA, S. Y. *et al.* Validation of a vector version of the 6S radiative transfer code for atmospheric correction of satellite data Part I: Path radiance. **Applied Optics**, v. 45, n. 26, p. 6762, 2006. Disponível em: https://www.osapublishing.org/abstract.cfm?URI=ao-45-26-6762.

KOTCHENOVA, S. Y.; VERMOTE, E. F. Validation of a vector version of the 6S radiative transfer code for atmospheric correction of satellite data Part II Homogeneous Lambertian and anisotropic surfaces. **Applied Optics**, v. 46, n. 20, p. 4455, 2007. Disponível em: https://www.osapublishing.org/abstract.cfm?URI=ao-46-20-4455.

KUENZER, C. *et al.* **Thermal Infrared Remote Sensing**. Dordrecht: Springer Netherlands, 2013-. ISSN 1567-3200.(Remote Sensing and Digital Image Processing). v. 17 Disponível em: http://link.springer.com/10.1007/978-94-007-6639-6.

LEE, H.; WON, J. S.; PARK, W. An atmospheric correction using high resolution numericalweather prediction models for satellite-borne single-channel mid-wavelength and thermal infrared imaging sensors. **Remote Sensing**, v. 12, n. 5, 2020.

LEMUS-CANOVAS, M. *et al.* Estimating Barcelona's metropolitan daytime hot and cold poles using Landsat-8 Land Surface Temperature. **Science of the Total Environment**, v. 699, p. 134307, 2020. Disponível em: https://doi.org/10.1016/j.scitotenv.2019.134307.

LI, H. *et al.* Evaluation of the NCEP and MODIS Atmospheric Products for Single Channel Land Surface Temperature Retrieval With Ground Measurements: A Case Study of HJ-1B IRS Data. **IEEE Journal of Selected Topics in Applied Earth Observations and Remote Sensing**, v. 6, n. 3, p. 1399–1408, 2013a. Disponível em: http://ieeexplore.ieee.org/document/6496155/.

LI, Z. L. *et al.* Land surface emissivity retrieval from satellite data. **International Journal of Remote Sensing**, v. 34, n. 9–10, p. 3084–3127, 2013b.

LI, Z. L. *et al.* Satellite-derived land surface temperature: Current status and perspectives. **Remote Sensing of Environment**, v. 131, p. 14–37, 2013c. Disponível em: http://dx.doi.org/10.1016/j.rse.2012.12.008.

LI, S.; JIANG, G.-M. Land Surface Temperature Retrieval From Landsat-8 Data With the Generalized Split-Window Algorithm. **IEEE Access**, v. 6, p. 18149–18162, 2018. Disponível em: http://ieeexplore.ieee.org/document/8323370/.

LILLESAND, T. M.; KIEFER, R. W.; CHIPMAN, J. W. **Remote sensing and image interpretation**. 7. ed. Hoboken: John Wiley & Sons Ltd, 2015.

MADALA, S.; SATYANARAYANA, A. N. V.; RAO, T. N. Performance evaluation of PBL and cumulus parameterization schemes of WRF ARW model in simulating severe thunderstorm events over Gadanki MST radar facility - Case study. **Atmospheric Research**, v. 139, p. 1–17, 2014. Disponível em: http://dx.doi.org/10.1016/j.atmosres.2013.12.017.

MALAKAR, N. K. *et al.* An Operational Land Surface Temperature Product for Landsat Thermal Data: Methodology and Validation. **IEEE Transactions on Geoscience and Remote Sensing**, v. 56, n. 10, p. 5717–5735, 2018. Disponível em: https://ieeexplore.ieee.org/document/8361068/.

MAO, K. *et al.* A practical split-window algorithm for retrieving land-surface temperature from MODIS data. **International Journal of Remote Sensing**, v. 26, n. 15, p. 3181–3204, 2005. Disponível em: https://www.tandfonline.com/doi/full/10.1080/01431160500044713.

MATTAR, C. *et al.* Global Atmospheric Profiles from Reanalysis Information (GAPRI): a new database for earth surface temperature retrieval. **International Journal of Remote Sensing**, v. 36, n. 19–20, p. 5045–5060, 2015. Disponível em: http://www.tandfonline.com/doi/full/10.1080/01431161.2015.1054965.

MCMILLIN, L. M. Estimation of sea surface temperatures from two infrared window measurements with different absorption. **Journal of Geophysical Research**, v. 80, n. 36, p. 5113–5117, 1975. Disponível em: http://doi.wiley.com/10.1029/JC080i036p05113.

MENG, X. *et al.* Estimating Land Surface Temperature from Landsat-8 Data using the NOAA JPSS Enterprise Algorithm. **Remote Sensing**, v. 11, n. 2, p. 155, 2019. Disponível em: http://www.mdpi.com/2072-4292/11/2/155.

MENG, X.; CHENG, J. Evaluating Eight Global Reanalysis Products for Atmospheric Correction of Thermal Infrared Sensor—Application to Landsat 8 TIRS10 Data. **Remote Sensing**, v. 10, n. 3, p. 474, 2018. Disponível em: http://www.mdpi.com/2072-4292/10/3/474.

MIRA, M. *et al.* Quantifying uncertainties in land surface temperature due to atmospheric correction: Application to Landsat-7 data over a Mediterranean agricultural region. *In*: 2014. **2014 IEEE Geoscience and Remote Sensing Symposium**. IEEE, 2014. p. 2375–2378. Disponível em: http://ieeexplore.ieee.org/document/6946949/.

MONTANARO, M. *et al.* Performance of the Thermal Infrared Sensor on-board Landsat 8 over the first year on-orbit. *In*: 2014a. (J. J. Butler, X. (Jack) Xiong, & X. Gu, Org.) **SPIE Optical Engineering + Applications Earth Observing Systems XIX**. 2014. p. 921817. Disponível em: http://proceedings.spiedigitallibrary.org/proceeding.aspx?doi=10.1117/12.2063457.

MONTANARO, M. *et al.* Stray Light Artifacts in Imagery from the Landsat 8 Thermal Infrared Sensor. **Remote Sensing**, v. 6, n. 11, p. 10435–10456, 2014b. Disponível em: http://www.mdpi.com/2072-4292/6/11/10435.

MONTANARO, M.; GERACE, A.; ROHRBACH, S. Toward an operational stray light correction for the Landsat 8 Thermal Infrared Sensor. **Applied Optics**, v. 54, n. 13, p. 3963, 2015. Disponível em: https://www.osapublishing.org/abstract.cfm?URI=ao-54-13-3963.

MOYA-ÁLVAREZ, A. S. *et al.* Influence of PBL parameterization schemes in WRF_ARW model on short - range precipitation's forecasts in the complex orography of Peruvian Central Andes. **Atmospheric Research**, v. 233, n. October 2019, p. 104708, 2020. Disponível em: https://doi.org/10.1016/j.atmosres.2019.104708.

MYLONAS, M. P. *et al.* Analysis of a Mediterranean Tropical-Like Cyclone. Sensitivity to WRF Parameterizations and Horizontal Resolution. **Atmosphere**, v. 10, n. 8, p. 425, 2019. Disponível em: https://www.mdpi.com/2073-4433/10/8/425.

NCEP *et al.* **NCEP FNL Operational Model Global Tropospheric Analyses, continuing from July 1999. Research Data Archive at the National Center for Atmospheric Research, Computational and Information Systems Laboratory**. 2000. Disponível em: https://doi.org/10.5065/D6M043C6.

NCEP *et al.* **NCEP Global Forecast System (GFS) Analyses and Forecasts**. Boulder, Colorado: Research Data Archive at the NCAR, Computational and

Information Systems Laboratory, 2007. Disponível em: https://doi.org/10.5065/D65Q4TSG.

NEINAVAZ, E.; SKIDMORE, A. K.; DARVISHZADEH, R. Effects of prediction accuracy of the proportion of vegetation cover on land surface emissivity and temperature using the NDVI threshold method. **International Journal of Applied Earth Observation and Geoinformation**, v. 85, n. September 2019, p. 101984, 2020. Disponível em: https://doi.org/10.1016/j.jag.2019.101984.

NICLÒS, R. *et al.* Evaluation of Landsat-8 TIRS data recalibrations and land surface temperature split-window algorithms over a homogeneous crop area with different phenological land covers. **ISPRS Journal of Photogrammetry and Remote Sensing**, v. 174, n. February, p. 237–253, 2021. Disponível em: https://linkinghub.elsevier.com/retrieve/pii/S0924271621000381.

NORMAN, J. M.; BECKER, F. Terminology in thermal infrared remote sensing of natural surfaces. **Remote Sensing Reviews**, v. 12, n. 3–4, p. 159–173, 1995. Disponível em: http://www.tandfonline.com/doi/abs/10.1080/02757259509532284.

OLTRA-CARRIÓ, R. *et al.* Land surface emissivity retrieval from airborne sensor over urban areas. **Remote Sensing of Environment**, v. 123, p. 298–305, 2012. Disponível em: http://dx.doi.org/10.1016/j.rse.2012.03.007.

ONWUKWE, C.; JACKSON, P. L. Meteorological downscaling with wrf model, version 4.0, and comparative evaluation of planetary boundary layer schemes over a complex coastal airshed. **Journal of Applied Meteorology and Climatology**, v. 59, n. 8, p. 1295–1319, 2020.

OTTLÉ, C.; STOLL, M. Effect of atmospheric absorption and surface emissivity on the determination of land surface temperature from infrared satellite data. **International Journal of Remote Sensing**, v. 14, n. 10, p. 2025–2037, 1993. Disponível em: http://www.tandfonline.com/doi/abs/10.1080/01431169308954018.

PÉREZ-PLANELLS, L.; GARCÍA-SANTOS, V.; CASELLES, V. Comparing different profiles to characterize the atmosphere for three MODIS TIR bands. **Atmospheric Research**, v. 161–162, p. 108–115, 2015. Disponível em: http://dx.doi.org/10.1016/j.atmosres.2015.04.001.

PERRY, E. M.; MORAN, M. S. An evaluation of atmospheric corrections of radiometric surface temperatures for a semiarid rangeland watershed. **Water Resources Research**, v. 30, n. 5, p. 1261–1269, 1994.

PLANCK, M. On the Law of Distribution of Engergy in the Normal Spectrum. **Annalen der Physik**, v. 4, n. 9, p. 553-, 1901.

POWERS, J. G. *et al.* The Weather Research and Forecasting Model: Overview, System Efforts, and Future Directions. **Bulletin of the American Meteorological**

Society, v. 98, n. 8, p. 1717–1737, 2017. Disponível em: http://journals.ametsoc.org/doi/10.1175/BAMS-D-15-00308.1.

PRASAD, A. A.; SHERWOOD, S. C.; BROGNIEZ, H. Using Megha-Tropiques satellite data to constrain humidity in regional convective simulations: A northern Australian test case. **Quarterly Journal of the Royal Meteorological Society**, n. January, p. 1–21, 2020.

PRATA, A. J. *et al.* Thermal remote sensing of land surface temperature from satellites: Current status and future prospects. **Remote Sensing Reviews**, v. 12, n. 3–4, p. 175–224, 1995. Disponível em: http://www.tandfonline.com/doi/abs/10.1080/02757259509532285.

PRICE, J. C. Estimating surface temperatures from satellite thermal infrared data—A simple formulation for the atmospheric effect. **Remote Sensing of Environment**, v. 13, n. 4, p. 353–361, 1983. Disponível em: http://linkinghub.elsevier.com/retrieve/pii/0034425783900366.

QIN, Z.; KARNIELI, A.; BERLINER, P. A mono-window algorithm for retrieving land surface temperature from Landsat TM data and its application to the Israel-Egypt border region. **International Journal of Remote Sensing**, v. 22, n. 18, p. 3719–3746, 2001.

RAJA, M. K. R. V. *et al.* The validation of AIRS retrievals of integrated precipitable water vapor using measurements from a network of ground-based GPS receivers over contiguous United States. **Journal of Atmospheric and Oceanic Technology**, v. 25, n. 3, p. 416–428, 2008.

REUTER, D. *et al.* The Thermal Infrared Sensor (TIRS) on Landsat 8: Design Overview and Pre-Launch Characterization. **Remote Sensing**, v. 7, n. 1, p. 1135–1153, 2015. Disponível em: http://www.mdpi.com/2072-4292/7/1/1135.

RIENECKER, M. M. *et al.* MERRA: NASA's modern-era retrospective analysis for research and applications. **Journal of Climate**, v. 24, n. 14, p. 3624–3648, 2011.

ROCHA, N. S. da *et al.* The Influence of Land Surface Temperature in Evapotranspiration Estimated by the S-SEBI Model. **Atmosphere**, v. 11, n. 10, p. 1059, 2020. Disponível em: https://www.mdpi.com/2073-4433/11/10/1059.

ROSAS, J.; HOUBORG, R.; MCCABE, M. F. Sensitivity of Landsat 8 Surface Temperature Estimates to Atmospheric Profile Data: A Study Using MODTRAN in Dryland Irrigated Systems. **Remote Sensing**, v. 9, n. 10, p. 988, 2017. Disponível em: http://www.mdpi.com/2072-4292/9/10/988.

ROY, D. P. *et al.* Landsat-8: Science and product vision for terrestrial global change research. **Remote Sensing of Environment**, v. 145, p. 154–172, 2014. Disponível em: https://linkinghub.elsevier.com/retrieve/pii/S003442571400042X.

SABINS, F. F. **Remote Sensing: Principles and Interpretation**. 2. ed. San Francisco: W.H. Freeman, 1986.

SAHA, S. *et al.* The NCEP Climate Forecast System Reanalysis. **Bulletin of the American Meteorological Society**, v. 91, n. 8, p. 1015–1058, 2010. Disponível em: http://journals.ametsoc.org/doi/10.1175/2010BAMS3001.1.

SAHA, S. *et al.* The NCEP Climate Forecast System Version 2. **Journal of Climate**, v. 27, n. 6, p. 2185–2208, 2014. Disponível em: http://journals.ametsoc.org/doi/abs/10.1175/JCLI-D-12-00823.1.

SAJIB, M. Q. U.; WANG, T. Estimation of land surface temperature in an agricultural region of Bangladesh from landsat 8: Intercomparison of four algorithms. **Sensors**, v. 20, n. 6, 2020.

SCHMUGGE, T. *et al.* Temperature and emissivity separation from multispectral thermal infrared observations. **Remote Sensing of Environment**, v. 79, n. 2–3, p. 189–198, 2002.

SEKERTEKIN, A. Validation of Physical Radiative Transfer Equation-Based Land Surface Temperature Using Landsat 8 Satellite Imagery and SURFRAD in-situ Measurements. **Journal of Atmospheric and Solar-Terrestrial Physics**, v. 196, n. July, p. 105161, 2019. Disponível em: https://doi.org/10.1016/j.jastp.2019.105161.

SEKERTEKIN, A.; BONAFONI, S. Land surface temperature retrieval from Landsat 5, 7, and 8 over rural areas: Assessment of different retrieval algorithms and emissivity models and toolbox implementation. **Remote Sensing**, v. 12, n. 2, 2020a.

SEKERTEKIN, A.; BONAFONI, S. Sensitivity analysis and validation of daytime and nighttime land surface temperature retrievals from landsat 8 using different algorithms and emissivity models. **Remote Sensing**, v. 12, n. 17, 2020b.

SHIN, H. H.; HONG, S. Y. Intercomparison of Planetary Boundary-Layer Parametrizations in the WRF Model for a Single Day from CASES-99. **Boundary-Layer Meteorology**, v. 139, n. 2, p. 261–281, 2011.

SIUTA, D.; WEST, G.; STULL, R. WRF hub-height wind forecast sensitivity to PBL scheme, grid length, and initial condition choice in complex terrain. **Weather and Forecasting**, v. 32, n. 2, p. 493–509, 2017.

SKAMAROCK, W. C. *et al.* **A Description of the Advanced Research WRF Model Version 4NCAR Technical Note NCAR/TN-475+STR**. Boulder, Colorado, 2019. Disponível em: http://library.ucar.edu/research/publish-technote.

SKOKOVIC, D.; SOBRINO, J. A.; JIMENEZ-MUNOZ, J. C. Vicarious Calibration of the Landsat 7 Thermal Infrared Band and LST Algorithm Validation of the ETM+ Instrument Using Three Global Atmospheric Profiles. **IEEE Transactions on Geoscience and Remote Sensing**, v. 55, n. 3, p. 1804–1811, 2017.

SOBRINO, J. A. *et al.* Land Surface Emissivity Retrieval From Different VNIR and TIR Sensors. **IEEE Transactions on Geoscience and Remote Sensing**, v. 46, n. 2, p. 316–327, 2008. Disponível em: http://ieeexplore.ieee.org/document/4358831/.

SOBRINO, J. A. *et al.* Review of thermal infrared applications and requirements for future high-resolution sensors. **IEEE Transactions on Geoscience and Remote Sensing**, v. 54, n. 5, p. 2963–2972, 2016.

SOBRINO, J. A.; CASELLES, V.; BECKER, F. Significance of the remotely sensed thermal infrared measurements obtained over a citrus orchard. **ISPRS Journal of Photogrammetry and Remote Sensing**, v. 44, n. 6, p. 343–354, 1990. Disponível em: https://linkinghub.elsevier.com/retrieve/pii/092427169090077O.

SOBRINO, J.; COLL, C.; CASELLES, V. Atmospheric correction for land surface temperature using NOAA-11 AVHRR channels 4 and 5. **Remote Sensing of Environment**, v. 38, n. 1, p. 19–34, 1991. Disponível em: https://linkinghub.elsevier.com/retrieve/pii/003442579190069I.

SOBRINO, J. A.; JIMÉNEZ-MUÑOZ, J. C.; PAOLINI, L. Land surface temperature retrieval from LANDSAT TM 5. **Remote Sensing of Environment**, v. 90, n. 4, p. 434–440, 2004. Disponível em: https://linkinghub.elsevier.com/retrieve/pii/S0034425704000574.

SOBRINO, J. A.; RAISSOUNI, N. Toward remote sensing methods for land cover dynamic monitoring: Application to Morocco. **International Journal of Remote Sensing**, v. 21, n. 2, p. 353–366, 2000. Disponível em: https://www.tandfonline.com/doi/full/10.1080/014311600210876.

SOBRINO, J.; RAISSOUNI, N.; LI, Z.-L. A Comparative Study of Land Surface Emissivity Retrieval from NOAA Data. **Remote Sensing of Environment**, v. 75, n. 2, p. 256–266, 2001. Disponível em: https://linkinghub.elsevier.com/retrieve/pii/S0034425700001711.

STENSRUD, D. J. **Parameterization Schemes**. Cambridge: Cambridge University Press, 2007-. ISSN 17577780.v. 9780521865 Disponível em: http://ebooks.cambridge.org/ref/id/CBO9780511812590.

STULL, R. **Practical Meteorology: An Algebra-based Survey of Atmospheric Science**. 1.02bed. Vancouver: University of British Columbia, 2017.

SUSSKIND, J.; ROSENFIELD, J.; REUTER, D. An accurate radiative transfer model for use in the direct physical inversion of HIRS2 and MSU Temperature Sounding Data. **Journal of Geophysical Research**, v. 88, n. C13, p. 8550, 1983. Disponível em: http://doi.wiley.com/10.1029/JC088iC13p08550.

TANG, H.; LI, Z. L. **Quantitative Remote Sensing in Thermal Infrared**. Berlin, Heidelberg: Springer Berlin Heidelberg, 2014. (Springer Remote

Sensing/Photogrammetry). *E-book*. Disponível em: http://link.springer.com/10.1007/978-3-642-42027-6.

TARDY, B. *et al.* A Software Tool for Atmospheric Correction and Surface Temperature Estimation of Landsat Infrared Thermal Data. **Remote Sensing**, v. 8, n. 9, p. 696, 2016. Disponível em: http://www.mdpi.com/2072-4292/8/9/696.

TAVARES, M. H. *et al.* Derivation of consistent, continuous daily river temperature data series by combining remote sensing and water temperature models. **Remote Sensing of Environment**, v. 241, n. June 2019, p. 111721, 2020. Disponível em: https://doi.org/10.1016/j.rse.2020.111721.

TONOOKA, H. An atmospheric correction algorithm for thermal infrared multispectral data over land-a water-vapor scaling method. **IEEE Transactions on Geoscience and Remote Sensing**, v. 39, n. 3, p. 682–692, 2001. Disponível em: http://ieeexplore.ieee.org/lpdocs/epic03/wrapper.htm?arnumber=911125.

TYAGI, B. *et al.* Performance analysis of planetary boundary layer parameterization schemes in WRF modeling set up over Southern Italy. **Atmosphere**, v. 9, n. 7, p. 1–22, 2018.

VALOR, E.; CASELLES, V. Mapping land surface emissivity from NDVI: Application to European, African, and South American areas. **Remote Sensing of Environment**, v. 57, n. 3, p. 167–184, 1996. Disponível em: https://linkinghub.elsevier.com/retrieve/pii/0034425796000399.

VAN DE GRIEND, A. A.; OWE, M. On the relationship between thermal emissivity and the normalized difference vegetation index for natural surfaces. **International Journal of Remote Sensing**, v. 14, n. 6, p. 1119–1131, 1993. Disponível em: https://www.tandfonline.com/doi/full/10.1080/01431169308904400.

VANHELLEMONT, Q. Automated water surface temperature retrieval from Landsat 8/TIRS. **Remote Sensing of Environment**, v. 237, p. 111518, 2020a. Disponível em: https://doi.org/10.1016/j.rse.2019.111518.

VANHELLEMONT, Q. Combined land surface emissivity and temperature estimation from Landsat 8 OLI and TIRS. **ISPRS Journal of Photogrammetry and Remote Sensing**, v. 166, p. 390–402, 2020b. Disponível em: https://doi.org/10.1016/j.isprsjprs.2020.06.007.

WANG, W. *et al.* **Advanced Research WRF (ARW) Version 4 Modeling System User´s Guide**. National Center for Atmospheric Research, 2019. Disponível em: https://www2.mmm.ucar.edu/wrf/users/docs/user_guide_V4/WRFUsersGuide.pdf.

WANG, F. *et al.* An Improved Mono-Window Algorithm for Land Surface Temperature Retrieval from Landsat 8 Thermal Infrared Sensor Data. **Remote Sensing**, v. 7, n. 4, p. 4268–4289, 2015. Disponível em: http://www.mdpi.com/2072-4292/7/4/4268.

WANG, L.; LU, Y.; YAO, Y. Comparison of three algorithms for the retrieval of land surface temperature from landsat 8 images. **Sensors**, v. 19, n. 22, 2019.

WEE, T. K. *et al.* Two overlooked biases of the advanced research wrf (arw) model in geopotential height and temperature. **Monthly Weather Review**, v. 140, n. 12, p. 3907–3918, 2012.

WENG, Q. Thermal infrared remote sensing for urban climate and environmental studies: Methods, applications, and trends. **ISPRS Journal of Photogrammetry and Remote Sensing**, v. 64, n. 4, p. 335–344, 2009. Disponível em: http://dx.doi.org/10.1016/j.isprsjprs.2009.03.007.

WINDAHL, E.; BEURS, K. de. An intercomparison of Landsat land surface temperature retrieval methods under variable atmospheric conditions using in situ skin temperature. **International Journal of Applied Earth Observation and Geoinformation**, v. 51, p. 11–27, 2016. Disponível em: http://dx.doi.org/10.1016/j.jag.2016.04.003.

WU, P. *et al.* Spatially Continuous and High-Resolution Land Surface Temperature Product Generation: A Review of Reconstruction and Spatiotemporal Fusion Techniques. **IEEE Geoscience and Remote Sensing Magazine**, v. 2, 2021. Disponível em: https://ieeexplore.ieee.org/document/9353399/.

XIE, B. *et al.* Evaluation of nonlocal and local planetary boundary layer schemes in the WRF model. **Journal of Geophysical Research Atmospheres**, v. 117, n. 12, p. 1–26, 2012.

XIE, B. *et al.* Structure of the planetary boundary layer over Southeast England: Modeling and measurements. **Journal of Geophysical Research Atmospheres**, v. 118, n. 14, p. 7799–7818, 2013.

YANG, J. *et al.* Evaluation of seven atmospheric profiles from reanalysis and satellite-derived products: Implication for single-channel land surface temperature retrieval. **Remote Sensing**, v. 12, n. 5, 2020.

YU, X.; GUO, X.; WU, Z. Land Surface Temperature Retrieval from Landsat 8 TIRS—Comparison between Radiative Transfer Equation-Based Method, Split Window Algorithm and Single Channel Method. **Remote Sensing**, v. 6, n. 10, p. 9829–9852, 2014. Disponível em: http://www.mdpi.com/2072-4292/6/10/9829.